Computational Study of Hypersonic Boundary Layer Stability on Cones

A DISSERTATION

SUBMITTED TO THE FACULTY OF THE GRADUATE SCHOOL

OF THE UNIVERSITY OF MINNESOTA

BY

Joel Edwin Gronvall

IN PARTIAL FULFILLMENT OF THE REQUIREMENTS

FOR THE DEGREE OF

Doctor of Philosophy

Dr. Graham Candler

December, 2012

© Joel Edwin Gronvall 2012
ALL RIGHTS RESERVED

Acknowledgements

This work was sponsored by Sandia National Laboratories, the Air Force Office of Scientific Research, the NASA Constellation University Institutes Project, and by the National Security Science and Engineering Faculty Fellowship. A portion of the computational results presented in this work were performed on the Itasca HPC machine at the Minnesota Supercomputing Institute. The views and conclusions contained herein are those of the authors and should not be interpreted as necessarily representing the official policies or endorsements, either expressed or implied, of the AFOSR or the U.S. Government.

During my time at the University of Minnesota, there have been a great number of people who have generously provided support and encouragement as I pursued my studies. I'd like to acknowledge just a few of them.

First, I'd like to start by thanking my advisor, Dr. Graham Candler who granted me the priviledge of working with him and his group. His contributions toward my work, my education, and my professional development are far too numerous to list. His patient mentoring, his immense knowledge in the field of CFD, and his guidance in my work in hypersonic boundary layer stability provided me with the best possible learning experience.

I'd also like to thank Dr. Heath Johnson for all the help and instruction he provided, especially early on in my graduate studies. He was an invaluable resource to have for learning about hypersonic boundary layer transition and provided me with comments and criticisms that helped improve the clarity in my work. I am grateful that I had the opportunity to work with him. Dr. Pramod Subbareddy was also an invaluable resource to have. He was always willing to share his fundamental insights in fluid dynamics and numerical methodologies and generously provided help when challenges arose. Dr. Ioannis Nompelis was greatly helpful in many matters, whether they were about coursework, research, or future career guidance. His advice was always welcomed and appreciated.

Next, I'd like to extend my gratitude to the Candler group and fellow aerospace graduate students. I'd like to thank Dr. Ross Wagnild for sharing his valuable insights concerning boundary layer stability. I'd also like to thank Erik Tylczak, Kyle McConaughey, Vincent Jusuf, Pietro Ferrero, and Loretta Trevino for their helpful discussions in our coursework. I'd also like to thank Dr. Matthew Bartkowicz and Dr. Travis Drayna for their guidance in making high-quality grids for high-fidelity simulations.

Lastly, I am greatly indebted to my wife and my family for their constant support, encouragement, patience, and prayers during my graduate studies. Most importantly, I'm thankful for the grace and mercy given to me daily by my Lord and Savior, Jesus Christ.

"The heart of man plans his way, but the Lord establishes his steps." Proverbs 16:9

Dedication

To my wife, Christine, and to my family.

Abstract

Due to the complex nature of boundary layer laminar-turbulent transition in hypersonic flows and the resultant effect on the design of re-entry vehicles, there remains considerable interest in developing a deeper understanding of the underlying physics. To that end, the use of experimental observations and computational analysis in a complementary manner will provide the greatest insights. It is the intent of this work to provide such an analysis for two ongoing experimental investigations.

The first focuses on the hypersonic boundary layer transition experiments for a slender cone that are being conducted at JAXA's free-piston shock tunnel HIEST facility. Of particular interest are the measurements of disturbance frequencies associated with transition at high enthalpies. The computational analysis provided for these cases included two-dimensional CFD mean flow solutions for use in boundary layer stability analyses. The disturbances in the boundary layer were calculated using the linear parabolized stability equations. Estimates for transition locations, comparisons of measured disturbance frequencies and computed frequencies, and a determination of the type of disturbances present were made. It was found that for the cases where the disturbances were measured at locations where the flow was still laminar but nearly transitional, that the highly amplified disturbances showed reasonable agreement with the computations. Additionally, an investigation of the effects of finite-rate chemistry and vibrational excitation on flows over cones was conducted for a set of theoretical operational conditions at the HIEST facility.

The second study focuses on transition in three-dimensional hypersonic boundary layers, and for this the cone at angle of attack experiments being conducted at the Boeing/AFOSR Mach-6 quiet tunnel at Purdue University were examined. Specifically, the effect of surface roughness on the development of the stationary crossflow instability are investigated in this work. One standard mean flow solution and two direct numerical simulations of a slender cone at an angle of attack were computed. The direct numerical simulations included a digitally-filtered, randomly distributed surface roughness and were performed using a high-order, low-dissipation numerical scheme on appropriately resolved grids. Comparisons with experimental observations showed excellent qualitative agreement. Comparisons with similar previous computational work were also made and showed agreement in the wavenumber range of the most unstable crossflow modes.

Contents

List of Tables

List of Figures

Chapter 1

Introduction

1.1 Background

Transition from laminar to turbulent flow in engineering applications remains a critical field of study. The effects of transition in high-speed boundary layers can have significant impact on design decisions for re-entry vehicles. For example, a turbulent boundary layer can result in a five-fold increase in surface heating compared with a laminar boundary layer. The integrated heating effect from this is substantial and results in greater demands from the thermal protection system. In addition, there is a significant increase in skin friction in a turbulent boundary layer over a laminar boundary layer. In the presence of an asymmetrical transition pattern, the unbalanced drag forces can considerably alter the trajectory and in rare cases can become excessive to the point of catastrophic loss of control. Therefore, there has been significant effort put forth by the research field to elucidate the physical mechanisms involved in the transition process, though a complete understanding remains elusive[8].

In addition to the numerous factors which affect boundary layer transition, the process itself can follow multiple paths toward transition from laminar to turbulent flow. A useful diagram is shown in Figure 1.1 which illustrates the known paths to turbulence. For this work, only Path A will be considered, which begins with the presence of environmental disturbances. In free-flight, this can consist of particulates, atmospheric turbulence, entropy-temperature spottiness, among others. It has been estimated that a typical free-flight acoustic disturbance can have an intensity of something less than 0.05%[9, 10] as measured by the root-mean-square pressure fluctuation to the mean pitot pressure. In hypersonic wind tunnels, disturbances mainly[11] arise due to

the turbulent break-down of the tunnel wall boundary layer resulting in noise being radiated into the flow[12]. In conventional tunnels the intensity of these disturbances can range anywhere from 1% to 5%[13], while quiet tunnels are beginning to approach intensity levels seen in free-flight[14]. The next step involves the interaction between the particular flowfield and the free-field disturbances, a process which Morkovin in 1969[15] described as the 'receptivity' process which can be influenced by surface roughness, nose bluntness, and Mach number, curvature, among others. Disturbances which are introduced into the boundary layer through this receptivity process may then be amplified in the linear growth regime under the appropriate conditions. In hypersonic flows, instabilities such as the first mode, Mack's second and higher modes, Görtler vortices, and crossflow instabilities are commonly observed. With sufficient amplification, these disturbances may then lead to the nonlinear breakdown at the onset of transition. The complexity and critical nature of this process is the basis for continued interest, especially as it applies to the design of hypersonic vehicles. Understanding these mechanisms and having the ability to predict and even influence them will be of great value.

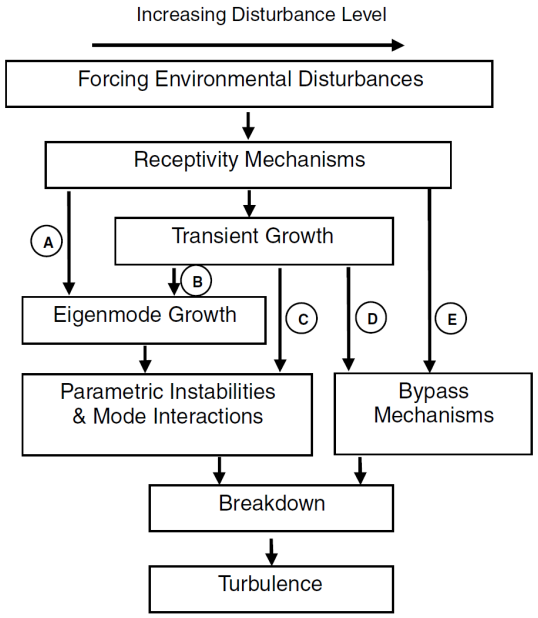

Figure 1.1: Boundary layer transition to turbulence map[2]. Adapted from Morkovin *et al.*[3]

1.2 Outline

It is the intent of this work to investigate some of the specific mechanisms which influence boundary layer transition on slender cones. As such, two cases have been examined here.

First, the linear growth, character, and evolution of streamwise disturbances at high enthalpies have been investigated for an axisymmetric case. Relevant to this end, recent experiments conducted at the free-piston shock tunnel HIEST (High Enthalpy Shock Tunnel) have examined boundary layer transition over a sharp cone and have therefore provided the basis for the two-dimensional computational analysis. In addition to providing heat flux measurements, high-speed pressure transducers were employed in order to directly measure boundary layer disturbance frequencies at four locations along the cone model. Utilizing the mean flow solutions, the boundary layer profiles were analyzed using the parabolized stability equations as implemented in STABL[16] which has been developed at the University of Minnesota.

Second, the stability characteristics of a hypersonic three-dimensional boundary layer were investigated for flow over a sharp cone at angle of attack. Current investigations of a cone at angle of attack are being conducted in the Boeing/AFOSR Mach-6 quiet tunnel at Purdue University. A representative set of conditions from these experiments have been used for the computational work. The specific purpose for these cases has been to investigate the role that surface roughness plays in the development of the crossflow instability. Pursuant to this, direct numerical simulations (DNS) of a cone with distributed surface roughness placed at angle of attack provided the high quality boundary layer transition data to be analyzed. These solutions were generated using a low-dissipation flux scheme in the three-dimensional unstructured Navier-Stokes solver, US3D[17], which has also been developed at the University of Minnesota.

- Chapter 2 briefly presents the governing equations for the compressible fluid flow, to be solved numerically.

- Chapter 3 provides the fundamental numerical approach upon which this work was completed.

- Chapter 4 presents boundary layer stability calculations which were based on the recent transition experiments conducted at the HIEST shock tunnel in Japan.

- Chapter 5 presents the direct numerical simulations of a cone with surface roughness at angle of attack. The conditions used were based on the set of experiments conducted at

Purdue's quiet tunnel.

- Chapter 6 6 provides a summary of the work presented and some conclusions based on this work.

Chapter 2

Governing Equations

The relevant equations of motion for the work presented here are the compressible Navier-Stokes equations. This set of coupled partial differential equations along with appropriate equations of state, provide a well-established means of describing aerodynamic flowfields. In this chapter, these equations, which are solved numerically are presented.

2.1 Conservation Equations

The three-dimensional compressible Navier-Stokes equations for a thermally and calorically perfect gas, expressed in partial differential equation form are as follows:

$$\frac{\partial \rho}{\partial t} + \frac{\partial \left(\rho u_i\right)}{\partial x_i} = 0 \tag{2.1a}$$

$$\frac{\partial \left(\rho u_i\right)}{\partial t} + \frac{\partial \left(\rho u_i u_j\right)}{\partial x_j} + \frac{\partial p}{\partial x_i} - \frac{\partial \tau_{ij}}{\partial x_j} = 0 \tag{2.1b}$$

$$\frac{\partial E}{\partial t} + \frac{\partial \left(\left(E+p\right) u_j\right)}{\partial x_j} + \frac{\partial q_j}{\partial x_j} - \frac{\partial \left(u_i \tau_{ij}\right)}{\partial x_j} = 0 \tag{2.1c}$$

where u_i is the velocity vector in the x_i direction (for $i = 1, 2, 3$), ρ is the fluid density, p is the pressure, E is the total energy, q_j is the heat conduction vector, and τ_{ij} are the shear stresses.

2.2 Constitutive Relations and Equations of State

Since the fluid is assumed to be a thermally and calorically perfect gas, the specific heats, c_v and c_p, are approximated as constant ($c_p = c_v + R$), the specific internal energy can be represented by the linear relation, $e = c_v T$, and the pressure can be determined using the ideal gas law, $p = \rho RT$. The total energy is represented by the following:

$$E = \frac{\rho u_i u_i}{2} + c_v T \tag{2.2}$$

The heat conduction vector, q_j, is assumed to be governed by Fourier's law for heat conduction:

$$q_j = -\kappa \frac{\partial T}{\partial x_j} \tag{2.3}$$

where κ is related to the viscosity through the Prandtl number ($Pr = c_p \mu / \kappa$), which is assumed to be constant at 0.72. The form of the viscous stress, τ_{ij}, is given by the following relation:

$$\tau_{ij} = \mu \left(\frac{\partial u_i}{\partial x_j} + \frac{\partial u_j}{\partial x_i} \right) + \lambda \frac{\partial u_k}{\partial x_k} \delta_{ij} \tag{2.4}$$

where μ is the kinematic viscosity and λ is the bulk viscosity. The bulk viscosity is related to the kinematic viscosity by invoking Stokes hypothesis resulting in $\lambda = -\frac{2}{3}\mu$. The viscosity was assumed to take the form given by Sutherland's law:

$$\mu = \mu_0 \frac{T^{\frac{2}{3}}}{T + T_0} \tag{2.5}$$

For air, the constant μ_0 was set at $1.458 \times 10^{-6} {}^{kg}/_{m-s}$ and the constant T_0 was set at 110.3 K. The set of equations laid out herein provide an adequate description of supersonic and even hypersonic aerodynamic flows on the condition that the temperature is sufficiently low that the effects of vibrational modes and chemical non-equilibrium are negligible.

Chapter 3

Numerical Method

Since no general analytical solution for the coupled set of partial differential equations described above has yet been discovered, a numerical approach must be used. As such, the results presented in this work, specifically the high-fidelity simulations, were computed using the US3D flow solver[17]. US3D is a fully three-dimensional, parallel, unstructured finite volume solver developed at the University of Minnesota for solving the compressible Navier-Stokes equation. This solver is capable of computing thermally and calorically perfect gases as well as gases in thermal and chemical non-equilibrium.

In this section, the fundamental construct of the finite volume formulation will be discussed. This will include the basics of the flux-vector splitting methodology, time advancement, as well as a discussion of the higher order formulations relevant to this work. More detailed discussions of the numerical methodology can be found in works by Nompelis[18, 17], Wright[19, 20], Candler[21], and Subbareddy[22].

3.1 Discretization

As a starting point in the formulation of the finite volume method, it is convenient to write the conserved variables in vector form:

$$U = (\rho, \rho u_1, \rho u_2, \rho u_3, E)^T \tag{3.1}$$

where u_1, u_2, and u_3 are commonly referred to as velocities u, v, and w. Using this, the governing equations can be written compactly as:

$$\frac{\partial U}{\partial t} + \frac{\partial F_j}{\partial x_j} = 0 \tag{3.2}$$

where,

$$F_j = \begin{pmatrix} \rho u_j \\ \rho u_1 u_j + p\delta_{1j} - \tau_{1j} \\ \rho u_2 u_j + p\delta_{2j} - \tau_{2j} \\ \rho u_3 u_j + p\delta_{3j} - \tau_{3j} \\ (E+p)\, u_j + \tau_{kj} u_k + q_j \end{pmatrix} \tag{3.3}$$

Equation 3.2 can then be restated in the weak form by integrating over an arbitrary control volume V yielding

$$\int_V \frac{\partial U}{\partial t} dV + \int_V \frac{\partial F_j}{\partial x_j} dV = 0 \tag{3.4}$$

Applying the divergence theorem to the spatial derivative in equation 3.4 gives the following result

$$V\frac{\partial U}{\partial t} + \oint_{\partial V} \left(\vec{F} \cdot \hat{n}\right) dS = 0 \tag{3.5a}$$

where $\hat{n}$ is the unit normal vector for the differential surface element dS on the surface ∂V of the control volume. This form of the equation naturally lends itself to the discretization process required for computations. A discretized domain will typically consist of an interconnected set of polyhedra with planar faces. Thus we can rewrite equation 3.5a in a semi-discrete form to take advantage of this.

$$\frac{\partial U_i}{\partial t} + \frac{1}{V_i}\sum_{j=1}^{N} \vec{F}_j \cdot \vec{S}_j = 0 \tag{3.5b}$$

where V_i represents the volume of an arbitrary cell i, U_i represents the vector of conserved variables averaged over the volume, N is the total number of faces on the cell, $\vec{F}_j$ is the total flux for each face of cell i, and $\vec{S}_j$ is the product of the area of the face with the unit normal vector $\hat{n}$. As implemented in US3D, the conserved variables are stored at the cell centers and fluxes are evaluated at each face centroid by reconstructing the variables using neighboring cells. Taking

a step back, one can recognize the elegant simplicity of the formulation shown in equation 3.5b where the change in the conserved variables of a particular cell can be determined by the sum of the fluxes across each of the faces.

3.2 Evaluation of the Fluxes

Noting the finite volume framework above, the focus of this section will be toward formulating a method to describe the fluxes. For this purpose, it is convenient to decompose the fluxes into two components:

$$F' = F'_I + F'_V \tag{3.6}$$

where F' is the scalar product of the flux vector and surface normal vector ($F' = \vec{F} \cdot \hat{n}$), F'_I is referred to as the inviscid flux, and F'_V as the viscous flux. The advantage of this decomposition is straight-forward when it is recognized that in the absence of the viscous terms and heat conduction in equation 2.1 the system reduces to the Euler equations, which are purely hyperbolic in nature. That is, information propagates in a "wave-like" fashion as it travels along the characteristics of the equation. In contrast, the viscous terms and heat conduction behave in an elliptic manner, where information travels in all directions simultaneously. It is this fundamental difference in behavior that requires separate treatment of the respective fluxes. In the following sections, a derivation of the underlying numerics in US3D are presented for both types fluxes.

3.2.1 Gradient Calculation

Before examining the mathematical construction for evaluating the fluxes, it is helpful to lay out the process for calculating the cell gradients, as they are fundamental to the formulations of both viscous and higher order inviscid fluxes in the current implementation of US3D. Practically speaking, there are two common methods for determining cell centered gradients on unstructured grids. The first applies the Green-Gauss theorem on a cell-by-cell basis to reconstruct the cell-centered gradients and the second employs a weighted least squares analysis over a defined stencil to reconstruct the gradients.

Green-Gauss Method

As the name implies, this method is a direct application of the Green-Gauss theorem, which simply states:

$$\int_V \nabla\phi dV = \int_{\partial V} \phi\hat{n} dS \tag{3.7}$$

where ϕ is the scalar quantity of which the gradient is desired, V is the volume, ∂V is the surface of the volume, and $\hat{n}$ is the outward point unit normal vector of differential surface element dS. Recognizing the similarities between this equation (3.7) and the application of the divergence theorem to the spatial derivatives in equation 3.5a, a similar discretization process can be employed yielding:

$$\nabla\phi = -\frac{1}{V}\sum_{faces} \phi_f \vec{S}_f \tag{3.8}$$

where $\nabla\phi$ is the desired gradient, ϕ_f is the scalar quantity at the face (typically constructed using an average of left and right quantities), and $\vec{S}_f$ is the product of the area of the face with the unit normal vector $\hat{n}$. While this method is easy to implement, it suffers from a drawback that prevents it from being useful to the work presented here. Specifically, this method loses accuracy in cells with high aspect ratios which is a common feature found in grids designed to simulate hypersonic boundary layer phenomena.

Weighted Least Squares Method

A common alternative to the Green-Gauss gradient reconstruction, is the weighted least squares technique which has been used for this work. The standard analysis performs a minimization of the function defined by

$$f = \sum_{k=1}^{N} w_{ik}^2 E_{ik}^2 \tag{3.9}$$

In order to make an estimate for the gradient of scalar ϕ at some point i, the error term E_{ik} in equation 3.9 must be appropriately constructed. Performing a Taylor series expansion to each

point in the stencil can accomplish this and is given by

$$\phi_k = \phi_i + \left(\frac{\partial \phi}{\partial x}\right)_i \triangle x_{ik} + \left(\frac{\partial \phi}{\partial y}\right)_i \triangle y_{ik} + \left(\frac{\partial \phi}{\partial z}\right)_i \triangle z_{ik} + h.o.t. \tag{3.10a}$$

where,

$$\triangle x_{ik} = x_k - x_i,\ \triangle y_{ik} = y_k - y_i,\ \triangle z_{ik} = z_k - z_i \tag{3.10b}$$

For convenience, in subsequent equations the partial derivatives $\frac{\partial \phi}{\partial x}$, $\frac{\partial \phi}{\partial y}$, and $\frac{\partial \phi}{\partial z}$ will be expressed as ϕ_x, ϕ_y, and ϕ_z, respectively. By simply rearranging equation 3.10a and substituting the relation $\triangle \phi_{ik} = \phi_k - \phi_i$ gives the weighted least squares problem to be minimized

$$f\left(\nabla \phi_i\right) = \sum_{k=1}^{N} w_{ik}^2 \left(\triangle \phi_{ik} - \left(\phi_x\right)_i \triangle x_{ik} - \left(\phi_y\right)_i \triangle y_{ik} - \left(\phi_z\right)_i \triangle z_{ik}\right)^2 \tag{3.11}$$

where k is summed over the list of N neighbors in the stencil and w_{ik} are the weights given to each neighbor. Finding the minimum of this function can be accomplished by differentiating equation 3.11 with respect to each gradient and setting them to zero

$$\begin{aligned}
\frac{\partial}{\partial \phi_x}\left(\sum_{k=1}^{N} w_{ik}^2 E_{ik}^2\right) &= \sum_{k=1}^{N} w_{ik}^2 \left(\triangle x_{ik}^2 \phi_x + \triangle x_{ik} \triangle y_{ik} \phi_y + \triangle x_{ik} \triangle z_{ik} \phi_z - \triangle \phi_{ik} \triangle x_{ik}\right) = 0 \\
\frac{\partial}{\partial \phi_y}\left(\sum_{k=1}^{N} w_{ik}^2 E_{ik}^2\right) &= \sum_{k=1}^{N} w_{ik}^2 \left(\triangle x_{ik} \triangle y_{ik} \phi_x + \triangle y_{ik}^2 \phi_y + \triangle y_{ik} \triangle z_{ik} \phi_z - \triangle \phi_{ik} \triangle y_{ik}\right) = 0 \\
\frac{\partial}{\partial \phi_z}\left(\sum_{k=1}^{N} w_{ik}^2 E_{ik}^2\right) &= \sum_{k=1}^{N} w_{ik}^2 \left(\triangle x_{ik} \triangle z_{ik} \phi_x + \triangle y_{ik} \triangle z_{ik} \phi_y + \triangle z_{ik}^2 \phi_z - \triangle \phi_{ik} \triangle z_{ik}\right) = 0
\end{aligned} \tag{3.12a}$$

Dropping the i index for clarity, rearranging terms, and rewriting in full matrix form gives

$$\underbrace{\begin{bmatrix} \sum w_k^2 \triangle x_k^2 & \sum w_k^2 \triangle x_k \triangle y_k & \sum w_k^2 \triangle x_k \triangle z_k \\ \sum w_k^2 \triangle x_k \triangle y_k & \sum w_k^2 \triangle y_k^2 & \sum w_k^2 \triangle y_k \triangle z_k \\ \sum w_k^2 \triangle x_k \triangle z_k & \sum w_k^2 \triangle y_k \triangle z_k & \sum w_k^2 \triangle z_k^2 \end{bmatrix}}_{[A]} \underbrace{\begin{bmatrix} \phi_x \\ \phi_y \\ \phi_z \end{bmatrix}}_{\nabla \phi} = \underbrace{\begin{bmatrix} \sum w_k^2 \triangle \phi_k \triangle x_k \\ \sum w_k^2 \triangle \phi_k \triangle y_k \\ \sum w_k^2 \triangle \phi_k \triangle z_k \end{bmatrix}}_{[b]} \tag{3.12b}$$

Neglecting the weights for the moment, it can be observed that the coefficients of matrix A are grid dependent only. This means that for static grids this matrix can be pre-computed once, inverted, and stored while only vector b needs to be recomputed each time the gradients are calculated. Turning back to the weights, if $w_{ik} = 1$ (unweighted) is chosen, the system may become ill-conditioned. Commonly, the weights are set based on an inverse distance, for instance $w_{ik} = \frac{1}{\sqrt{\triangle x_{ik}^2 + \triangle y_{ik}^2 + \triangle z_{ik}^2}}$, which provides a much better conditioned system. There is yet another choice for the weights that can also provide improved numerical stability over the unweighted case while yielding higher order accuracy compared with the simple inverse distance. It can be demonstrated that if the weights are proportional to $\triangle x^{-3/2}$ the gradients are second order accurate and the effect on stability compared with inverse distance is, in practice, negligible.

3.2.2 Inviscid Fluxes

Steger-Warming Flux

Taking a look at the inviscid fluxes, it is again useful to consider the Euler equations. Due to the specific nature of the propagation of information in these equations, a sophisticated treatment of flux evaluation is required to maintain numerical stability. In US3D, the Steger-Warming flux vector splitting scheme[23] is implemented to achieve this goal. This method is commonly employed as a shock capturing scheme and is often referred to as an upwind biasing method for its foundation in characteristic theory.

First, this scheme takes advantage of the inviscid flux property in which it is homogeneous in the vector of conserved variables.

$$F'(\lambda U) = \lambda F'(U) \tag{3.13}$$

where U is the vector of conserved variables and λ is an arbitrary scalar. This property permits the application of Euler's homogeneous function theorem and thus the fluxes can be written as an exact linearization:

$$F'(U) = \frac{\partial F'}{\partial U} \cdot U = A_{SW} \cdot U \tag{3.14}$$

where A_{SW} (subscript denotes Steger-Warming) is the Jacobian matrix for the inviscid flux. Recognizing again that the Euler equations are hyperbolic means that the Jacobian matrix can

be diagonalized. Initially, one might try to diagonalize $A_{SW} = \frac{\partial F'}{\partial U}$ directly, however in practice this would be difficult. Utilizing a different set of variables, simplifies this process greatly. The process is as follows:

$$A_{SW} = S^{-1}\frac{\partial V}{\partial U}\frac{\partial F'}{\partial V}S \tag{3.15a}$$

where,

$$V = (\rho, u_1, u_2, u_3, p)^T \tag{3.15b}$$

and,

$$S = \frac{\partial V}{\partial U},\ S^{-1} = \frac{\partial U}{\partial V} \tag{3.15c}$$

are defined as transformation matrices. Taking the center matrix and defining it as:

$$M = \frac{\partial V}{\partial U}\frac{\partial F'}{\partial V} \tag{3.16a}$$

and diagonalizing it,

$$M = C^{-1}\Lambda C \tag{3.16b}$$

which yields,

$$\Lambda = \begin{bmatrix} \lambda_1 & & 0 \\ & \ddots & \\ 0 & & \lambda_m \end{bmatrix} \tag{3.16c}$$

Matrices C^{-1} and C are referred to as the left and right eigenvector matrices, respectively and Λ represents the eigenvalue matrix. For a more explicit derivation of these matrices, the reader should refer to Nompelis[18] or Subbareddy[22]. With this information, the eigenvalue matrix can now be split into positively and negatively moving components, i.e. flux vector splitting:

$$\Lambda^{\pm} = \frac{\Lambda \pm |\Lambda|}{2} \tag{3.17}$$

This is an important feature, as this provides a mathematical test for determining the direction and speed that information is traveling in a manner that reflects the underlying physics.

Applying this knowledge, the inviscid fluxes are split into a positively moving flux and a negatively moving flux corresponding to the values calculated using equation 3.17:

$$\begin{aligned} F' &= F'^{+} + F'^{-} \\ F'^{+} &= A^{+}_{SW} \cdot U = \left(S^{-1}C^{-1}\Lambda^{+}CS\right) \cdot U \\ F'^{-} &= A^{-}_{SW} \cdot U = \left(S^{-1}C^{-1}\Lambda^{-}CS\right) \cdot U \end{aligned} \tag{3.18}$$

Now, the Steger-Warming flux vector splitting can be formally stated as follows:

$$F'_I = A^{+}_{SW} \cdot U_i + A^{-}_{SW} \cdot U_{i+1} \tag{3.19}$$

where i represents the cell adjacent to the face on the left, $i+1$ represents the cell adjacent to the right, A^{+}_{SW} is the positive flux Jacobian evaluated using U_i, and A^{-}_{SW} is the negative flux Jacobian evaluated using U_{i+1}. This formulation is straight-forward, however it is highly dissipative due to the fact that the Jacobians are evaluated using the upwind cell data. However, a simple modification to this method was proposed by MacCormack and Candler[21]. By simply evaluating the Jacobians at the face using averaged flow quantities from the two adjacent cells reduces dissipation. Thus both A^{+}_{MSW} and A^{-}_{MSW} (subscript denotes modified Steger-Warming) are evaluated using U_f which can be calculated using any reasonable average of U_i and U_{i+1}. This gives:

$$F'_I = A^{+}_{MSW} \cdot U_i + A^{-}_{MSW} \cdot U_{i+1} \tag{3.20}$$

While this modification reduces numerical dissipation, it can also result in numerical instability in regions of high gradients, such as shocks. Therefore, in practice the two schemes are blended using a pressure weighted average that smoothly switches between the two. The blending function is constructed as follows:

$$U_f = w_f U_i + (1 - w_f) U_{i+1} \tag{3.21a}$$

where,

$$w_f = 1 - \frac{1}{2}\left(\frac{1}{(\beta \triangle p)^2 + 1}\right) \tag{3.21b}$$

and

$$\triangle p = \frac{p_L - p_R}{min\,(p_L, p_R)} \tag{3.21c}$$

where p_L and p_R are the values of pressure on the left and right sides of the face, respectively. The coefficient β governs the sensitivity of the blending function. The effect of w_f is that in smooth regions its value limits to 0.5 while in regions of large gradients it will limit to either 0 or 1 depending on which direction is upwind.

One correction regarding this method is still required. When the eigenvalues of the system go to zero along sonic lines, there is an issue commonly referred to as a "sonic glitch" where numerical error is generated. Additionally, in stagnation regions where convection speeds are minimal compared to sound speeds, numerical error may become trapped. For example, in blunt body geometries if there is even slight grid misalignment with the bow shock, error can be generated and can accumulate in the stagnation region resulting in an aphysical deformation known as a carbuncle. A simple modification, known as an eigenvalue limiter, alleviates both problems by defining the following:

$$\begin{aligned} \lambda^+ &= \tfrac{1}{2}\left(\lambda^+ + \sqrt{\lambda^{+2} + \epsilon^2}\right) \\ \lambda^- &= \tfrac{1}{2}\left(\lambda^- + \sqrt{\lambda^{-2} + \epsilon^2}\right) \end{aligned} \tag{3.22}$$

where ε is some small fraction of the speed of sound.

Lastly, it should be noted that this formulation is locally first-order accurate. However, for the work presented here, higher order methods were employed and will be discussed in the following section.

Higher Order Spatial Accuracy

Keeping the form expressed in equations 3.19 and 3.20, attention can now be given to the vectors of conserved variables to the left (U_i) and right (U_{i+1}) of the face being evaluated. For the higher order methods to be discussed in this section, it is convenient to replace U_i and U_{i+1} with more generic values U_L and U_R to be defined later (subscripts indicate either left or right). The flux vector splitting formulation is now

$$F'_I = A^+_{MSW} \cdot U_L + A^-_{MSW} \cdot U_R \tag{3.23}$$

It is useful to take a step back and consider the motivation for pursuing higher order schemes. The simple answer is primarily to improve the ability to capture small scale flow features. With this in view, any minimization of dissipation that is associated with the numerics while still maintaining stability will provide such improvement. Therefore, it is helpful to decompose and rearrange the inviscid fluxes into a so-called skew-symmetric form through a straightforward procedure. This can be shown for the modified Steger-Warming flux vector splitting in the following steps:

$$\begin{aligned} F'_I &= \left(S^{-1}C^{-1}\Lambda^+ CS\right)\cdot U_L + \left(S^{-1}C^{-1}\Lambda^- CS\right)\cdot U_R \\ &= \left(S^{-1}C^{-1}\tfrac{\Lambda+|\Lambda|}{2}CS\right)\cdot U_L + \left(S^{-1}C^{-1}\tfrac{\Lambda-|\Lambda|}{2}CS\right)\cdot U_R \\ &= \left(S^{-1}C^{-1}\Lambda CS\right)\cdot \tfrac{U_L+U_R}{2} - \tfrac{1}{2}\left(S^{-1}C^{-1}\left|\Lambda\right|CS\right)\cdot(U_R-U_L) \\ &= \underbrace{A\cdot\left(\frac{U_L+U_R}{2}\right)}_{symmetric/central} + \underbrace{\frac{1}{2}\left|A\right|\cdot(U_R-U_L)}_{upwinded/dissipative} \end{aligned} \tag{3.24}$$

Examining this result, it can be seen that this formulation contains two essential components, a symmetric non-dissipative contribution and an upwinded dissipative contribution. It is now possible, with this formulation, to take advantage of computing each of these components separately, adding the upwinded component in regions where numerical stability is required, such as shocks, and using a form of the symmetric component alone wherever possible.

Digging into the details of the dissipative component first, the form that this component takes bears a resemblance to that of a first derivative taken across the face. It is on this basis that the dissipative character of this term is recognized. Turning toward formulating higher order accuracies, one can construct the left and right values used in the differencing with various stencils. Shown below, in increasing order of accuracy, are some formulations which can be used:

$$\begin{array}{llll} 1^{\text{st}}\ \text{Order:} & U_L = U_i & \text{and} & U_R = U_{i+1} \\ 2^{\text{nd}}\ \text{Order:} & U_L = \frac{3U_i - U_{i-1}}{2} & \text{and} & U_R = \frac{3U_{i+1} - U_{i+2}}{2} \\ 3^{\text{rd}}\ \text{Order:} & U_L = \frac{3U_{i+1} + 6U_i - U_{i-1}}{8} & \text{and} & U_R = \frac{3U_i + 6U_{i+1} - U_{i+2}}{8} \end{array} \tag{3.25}$$

Now that a higher order upwinding has been developed separately from the symmetric portion, it may be advantageous to remove the dissipative portion of the flux entirely in smooth regions where

the dangers of numerical instability are negligible while adding it only in regions that require it. A switch that premultiplies this component would modify equation 3.24 to look like:

$$F_I' = F_{sym} + \alpha F_{diss} \tag{3.26}$$

A switch that is tuned to certain features of the flow to provide a value of 0 in smooth regions and vary smoothly to a value of 1 in regions of large gradients would be optimal. As such, a switch proposed by Ducros[24] attempts to provide such operation and is given by

$$\alpha = \frac{\left(\vec{\nabla} \cdot \vec{u}\right)^2}{\left(\vec{\nabla} \cdot \vec{u}\right)^2 + \|\vec{\omega}\|^2} \tag{3.27}$$

For this work, this Ducros switch provided adequate operation.

Moving to the symmetric/central component of the fluxes, it is this portion of the fluxes that is critical to achieving higher order, low dissipation solutions. As such, the standard technique of using the flux Jacobians must be abandoned due to their inherent second order accurate nature. Instead this component is computed directly using reconstructed variables at the cell faces. These values are reconstructed using the gradients as previously described in section 3.2.1. For this work a sixth order accurate reconstruction is used and is formulated as follows

$$\phi_f = \frac{(\phi_i + \phi_{i+1})}{2} + \frac{8\left(\nabla\phi_i \cdot \triangle x_i + \nabla\phi_{i+1} \cdot \triangle x_{i+1}\right)}{15} - \frac{\left(\nabla\phi_{i-1} \cdot \triangle x_{i-1} + \nabla\phi_{i+2} \cdot \triangle x_{i+2}\right)}{45} \tag{3.28}$$

It should be noted that while this symmetric flux was formulated using a one-dimensional stencil with uniform grid spacing and the factors multiplying each quantity were selected such that sixth order characteristics were achieved in the modified wavenumber, this was used on more complex grid constructions that contained anisotropies. For this reason, this method is considered *nominally* sixth order accurate but does in practice provide greater accuracy over lower order methods.

3.2.3 Viscous Fluxes

For the viscous fluxes, a straightforward procedure is used to directly calculate the fluxes. In this work, the cell-centered gradients calculated using the weighted least squares method (section 3.2.1)

are used to calculate the gradients at the face using a procedure called deferred correction. Initially, one may be tempted to use a simple average of the cell-centered gradients from the cells adjacent to the face, however in practice this method proves inaccurate and can cause numerical stability issues. Instead a blending of methods is used. To start, the gradients at the face are decomposed into two components, one aligned normal to the face and one aligned parallel to the face giving rise to the following relation

$$\nabla\phi_f = \underbrace{\left(\nabla\phi_f \cdot \hat{n}\right)\hat{n}}_{normal\,component} + \underbrace{\left(\nabla\phi_f - \left(\nabla\phi_f \cdot \hat{n}\right)\hat{n}\right)}_{tangential\,component} \tag{3.29}$$

or simply,

$$\nabla\phi_f = \left(\nabla\phi_f\right)_N + \left(\nabla\phi_f\right)_T \tag{3.30}$$

where $\hat{n}$ is the face unit normal vector. For the tangential component $\left(\nabla\phi_f\right)_T$, a distance weighted average is sufficient and thus only requires some simple rearranging of equation 3.30 to be obtained

$$\begin{aligned} \left(\nabla\phi_f\right)_T &= \nabla\phi_f - \left(\nabla\phi_f\right)_N \\ \left(\nabla\phi_f\right)_T &= \left(\tfrac{\nabla\phi_i + \nabla\phi_{i+1}}{2}\right) - \left(\tfrac{\nabla\phi_i + \nabla\phi_{i+1}}{2} \cdot \hat{n}\right)\hat{n} \end{aligned} \tag{3.31}$$

For the normal component, a more reasonable estimate is used and is given by

$$\left(\nabla\phi_f\right)_N \approx \left(\frac{\phi_{i+1} - \phi_i}{\triangle l}\hat{e} \cdot \hat{n}\right)\hat{n} \tag{3.32}$$

where $\triangle l$ is the distance between centroids of the adjacent cells and $\hat{e}$ is the unit vector defining the direction between the two centroids. Combining equations 3.31 and 3.32 gives the so-called deferred correction gradient at the face

$$\widetilde{\nabla\phi_f} = \frac{\nabla\phi_i + \nabla\phi_{i+1}}{2} + \left(\frac{\phi_{i+1} - \phi_i}{\triangle l}\hat{e} \cdot \hat{n} - \frac{\nabla\phi_i + \nabla\phi_{i+1}}{2} \cdot \hat{n}\right)\hat{n} \tag{3.33}$$

Once the gradients are known at the face it is a simple matter to calculate the viscous fluxes.

3.3 Time Advancement

Now that a spatially discrete system of equations has been developed, a method for advancing in time is required. For this work, implicit time advancement was used, however it is instructive to begin by looking at explicit schemes. For this, a common approach to explicit time advancement is the first order Euler backward differencing given by

$$\frac{\partial U_i}{\partial t} \approx \frac{U_i^{n+1} - U_i^n}{\triangle t} \tag{3.34}$$

applying this technique to equation 3.5b gives

$$\frac{U_i^{n+1} - U_i^n}{\triangle t} + \frac{1}{V_i}\sum_{j=1}^{N} \vec{F}_j^n \cdot \vec{S}_j = 0 \tag{3.35}$$

It can be shown that for explicit schemes there exists a maximum allowable time step that ensures numerical stability which is based on the spatial grid spacing and wave speed and is given by the following relation

$$\triangle t < \frac{\triangle x}{|u'| + c} \tag{3.36}$$

where c is a local speed of sound. Unfortunately, for the type of problems considered in this work this time step is too restrictive. This is due to the very fine nose radii of the cones considered herein along with clustering in the boundary layer, all of which creates a large range of length scales that makes it difficult to get sufficient flow times for the flow phenomena of interest. Therefore, an implicit time advancement scheme is used for this work. In order to implement such a method, a linearization of the fluxes is required to obtain the fluxes at time $n+1$. This process is shown for the inviscid fluxes

$$\begin{aligned} F_f^{n+1} &\approx F_f^n + \left(\frac{\partial F_f}{\partial U}\right)^n \left(U^{n+1} - U^n\right) \\ &\approx F_f^n + A_f^n \delta U^n \end{aligned} \tag{3.37}$$

where the subscript f indicates values evaluated at the face in question and δU. In order to cast this linearization in a form suitable to the cell-centered formulation of US3D, the component $A_f^n \delta U^n$ is split using the same flux vector splitting methodology described in section 3.2.2

$$F_f^{n+1} \approx F_f^n + A_f^{+n}\delta U_i^n + A_f^{-n}\delta U_{i+1}^n \tag{3.38}$$

where A^+ and A^- represent the Jacobians of the split flux vectors. For treatment of the implicit viscous fluxes see Nompelis[18]. Now the entire system can be assembled

$$\delta U_i^n = -\frac{\triangle t}{V_i}\sum_f \left(F_f^n + A_f^{+n}\delta U_i^n + A_f^{-n}\delta U_{i+1}^n\right) S_f \tag{3.39}$$

This system can be rewritten to illustrate how this system can be solved

$$\underbrace{\left(I + \frac{\triangle t}{V_i}\sum_f A_f^{+n} S_f\right)}_{Diagonal\,terms}\delta U_i^n + \underbrace{\left(\frac{\triangle t}{V_i}\sum_f A_f^{-n} S_f\right)}_{Off-diagonal\,terms}\delta U_{i+1}^n = \underbrace{\left(-\frac{\triangle t}{V_i}\sum_f F_f^n S_f\right)}_{RHS} \tag{3.40}$$

where I is the identity matrix. Now, if the off-diagonal terms are moved to the right hand side (RHS), relaxation methods such as full matrix point relaxation (FMPR) or data parallel line relaxation (DPLR) can be used to solve the system. The reader is referred to Wright[20] for a full derivation of these methods.

For this work, a second order implicit scheme was used. These scheme replaces equation 3.34 with the following second order formulation

$$\frac{\partial U_i}{\partial t} \approx \frac{3U_i^{n+1} - 4U_i^n + U_i^{n-1}}{2\triangle t} \tag{3.41}$$

and following the same procedure for the first order derivation results in the following system

$$\left(\frac{3}{2}I + \frac{\triangle t}{V_i}\sum_f A_f^{+n} S_f\right)\delta U_i^n + \left(\frac{\triangle t}{V_i}\sum_f A_f^{-n} S_f\right)\delta U_{i+1}^n = \left(\frac{1}{2}\delta U_i^{n-1} - \frac{\triangle t}{V_i}\sum_f F_f^n S_f\right) \tag{3.42}$$

From here, relaxation methods are used.

3.4 Boundary Conditions

In US3D, the explicit boundary conditions are enforced using ghost cells which are an extra layer of cells placed along every boundary of the grid. The variables stored in these ghost cells

are selected such that the appropriate boundary conditions are imposed. This treatment of the boundary conditions is simple to implement, for example an inviscid wall condition only requires that a tangency condition on the velocity is imposed: $\vec{u} \cdot \vec{n} = 0$. This involves simply reflecting the normal component of the velocity found in the boundary cell and using that value in the adjacent ghost cell. A similar process can be used for the no-slip condition, however in addition to the normal component, the tangential component is reflected as well resulting in a zero velocity condition at the boundary.

Due to the characteristic nature of hypersonic flow, the inflow conditions are fully specified by specifying the freestream conditions. Outflow conditions are straightforward for fully supersonic values. In cases with subsonic flow, the outflow boundary condition requires more sophisticated treatment. For this work, care was taken such that the outflow plane saw entirely supersonic flow.It is assumed that pressure is constant within the boundary layer, therefore $p_{ghost} = p_{interior}$. For isothermal wall condition, the desired temperature of the wall, T_w, is set using the following relation $T_{ghost} = 2T_w - T_{interior}$.

The process for setting boundary conditions in implicit schemes is more complex. In this case, instead of setting certain values in the ghost cells, the effect that the boundaries have on the implicit operator are enforced. Take, for example, the following term

$$A_f^{-n} \delta U_{i+1}^n S_f \tag{3.43}$$

In this case there is the potential that $i + 1$ lies outside of a boundary. In such a case, the ghost cell values are enforced by "folding" them into the implicit operator. To accomplish this, the following form is assumed

$$\delta U_{ghost} = E \, \delta U_{interior} \tag{3.44}$$

where E is some matrix. The task that remains is to figure out the form of E. To this end, it is useful to switch to primitive variables $V = (\rho \, u \, v \, w \, p)$, since these are the quantities upon which boundary conditions may be enforced. Now consider

$$\delta V_{ghost} = R \, \delta V_{interior} \tag{3.45}$$

Recalling that $\delta U = \frac{\partial U}{\partial V} \delta V = S^{-1} \delta V$ gives the following result

$$\delta U_{ghost} = \underbrace{\left(S_{ghost}^{-1} R\, S\right)}_{E} \delta U_{interior} \tag{3.46}$$

Now that the form of E has been illuminated, the implicit operator may now be modified at the boundary to include

$$A_f^{-n} \delta U_{ghost}^n = \left(A_f^{-n} E \delta\right) U_{interior}^n \tag{3.47}$$

Chapter 4

Slender Cone: Axisymmetric

4.1 Introduction

Laminar-turbulent boundary layer transition in high-speed flows continues to be a topic of great interest. In particular, boundary layer stability of two-dimensional and axisymmetric flows has received significant attention with slender cones being one of the geometries of choice. In such flows, absent surface roughness, streamwise disturbances have been identified as Mack's first, second, and higher modes[25]. The second and higher modes belong to a family of trapped acoustic waves that arise due to the presence of a region of supersonic mean flow relative to the disturbance phase velocity. Observations from theory[25], experiments, and computations have confirmed that the second mode instability is most often the dominant mechanism for inducing transition in two-dimensional high-speed flows[26]. For insulated surfaces, this trend occurs for flows greater than Mach 4 and can occur at even lower Mach numbers for cooled surfaces. Efforts to study these phenomena have provided increasingly greater understanding of the underlying physics, however these mechanisms remain poorly understood[8] resulting in uncertainties in transition prediction.

Following Mack's[25] pioneering work applying linear stability theory to high speed boundary layers and his identification of the now well-known second mode, there have been continuing efforts toward the verification of stability theory in high speed flows through experimental observations. Early on, stability experiments utilizing hot-wire anemometry conducted by Kendall[27, 28] and Demetriades[29, 30] confirmed the existence of Mack's second mode instability. This led to an extensive experimental program headed by Stetson[31, 32, 33, 34, 35] to further investigate these instabilities over a range of parameters culminating in an excellent review of their observations

in a 1992 publication[36]. Later, experiments[37] conducted at Purdue's Boeing/AFOSR Mach 6 Quiet Tunnel (BAM6QT) using hot-wire anemometry examined instabilities on cones under both conventional free-stream noise levels and quiet flow conditions with comparisons to stability theory. More recently, however, advances in sensing technologies have provided high-speed heat flux sensors and pressure transducers which are capable of resolving the high frequency fluctuations associated with hypersonic boundary layer instabilities. This permits instability measurements at high speed, high stagnation enthalpy conditions which were previously inaccessible to hot-wire measurements due to insufficient overheat ratios and wire breakage at such conditions. The first application[38] of high speed pressure transducers showed that it is indeed possible to measure second mode instabilities at high enthalpy conditions. Subsequent experiments[39, 40, 41, 42, 43] successfully employed these new classes of sensors for similar investigations and are continuing to gain wider use.

In concert with these experiments, boundary layer analysis techniques such as linear stability theory[44, 45, 46, 47] (LST) and the parabolized stability equations[48, 49, 16, 50] (PSE) have provided valuable insights into the linear growth regime of disturbances. These tools have been gaining widespread use in the analysis of hypersonic boundary layer stability and are well suited to axisymmetric flows. The recent focus on the direct measurement of second mode disturbances on slender cones in high speed flows provides increased opportunities to validate stability theory in addition to gaining greater physical insights. One such set of experiments which will be examined for this work is the transition experiments conducted at the free-piston shock tunnel HIEST[40] which used pressure transducers to measure pressure fluctuations on a cone surface. In addition, heat flux measurements were taken to aid in detecting any transition front present. As such, computational analysis, which includes high enthalpy effects, of the experiments using PSE have been completed using the STABL[16] software suite. The tools provided with this software include grid generation tools, a two-dimensional/axisymmetric CFD solver based on the implicit data-parallel line relaxation (DPLR)[20], and the stability analysis code, PSE-Chem.

4.2 Experimental Setup

The **Hi**gh **E**nthalpy **S**hock **T**unnel (HIEST) facility located at JAXA's (Japan Aerospace Exploration Agency) Kakuda Space Research Center is a large free-piston shock tunnel capable of producing stagnation pressures up to 150 MPa at a stagnation enthalpy of 25 MJ/kg. The facility

consists of a high pressure air reservoir, compression tube, shock tube, nozzle, and test section. A schematic of the facility is shown in Figure 4.1 and a list of relevant specifications can be found in Table 4.1. The reader is referred to Itoh *et al.*[51] for more details regarding the HIEST facility.

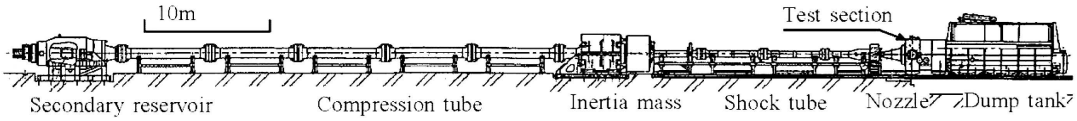

Figure 4.1: Free-piston shock tunnel HIEST.

Compression Tube	Length:	42 m
	Bore:	600 mm
Shock Tube	Length:	17 m
	Bore:	180 mm
Piston Mass		220 kg to 780 kg
Conical Nozzle	Exit Diameter:	1.2 m
Contoured Nozzle	Exit Diameter:	0.8 m
Stagnation Pressure		12 MPa to 150 MPa
Stagnation Enthalpy		3 MJ/kg to 25 MJ/kg
Test Time		2 ms or longer

Table 4.1: HIEST specifications.

The primary focus of this chapter centers around the first campaign of transition experiments performed at the JAXA free-piston shock tunnel HIEST[40]. Two additional similar campaigns[52, 53] have subsequently been conducted but will not be considered here. The experimental model used for these cases consisted of a 7° half angle cone with a 2.5 mm blunted nose tip and an axial length of 1100 mm and is shown in the photograph and schematic in Figure 4.2. Installed onto the surface of the cone model were a total of 86 miniature co-axial thermocouples. However, due to certain limitations, data from only 72 of the 86 thermocouples were recorded. In addition to the thermocouples, four piezoelectric pressure transducers of the type PCB132A37 were installed flush with the surface of the model in order to measure pressure fluctuations in the boundary layer. These transducers had a response time of greater than 1 MHz, providing adequate ability to capture the 100 kHz magnitude frequencies that would be expected from second mode disturbances

at the experimental conditions. The transducers were mounted at the following axial locations: 656 mm, 782 mm, 908 mm, and 1034 mm.

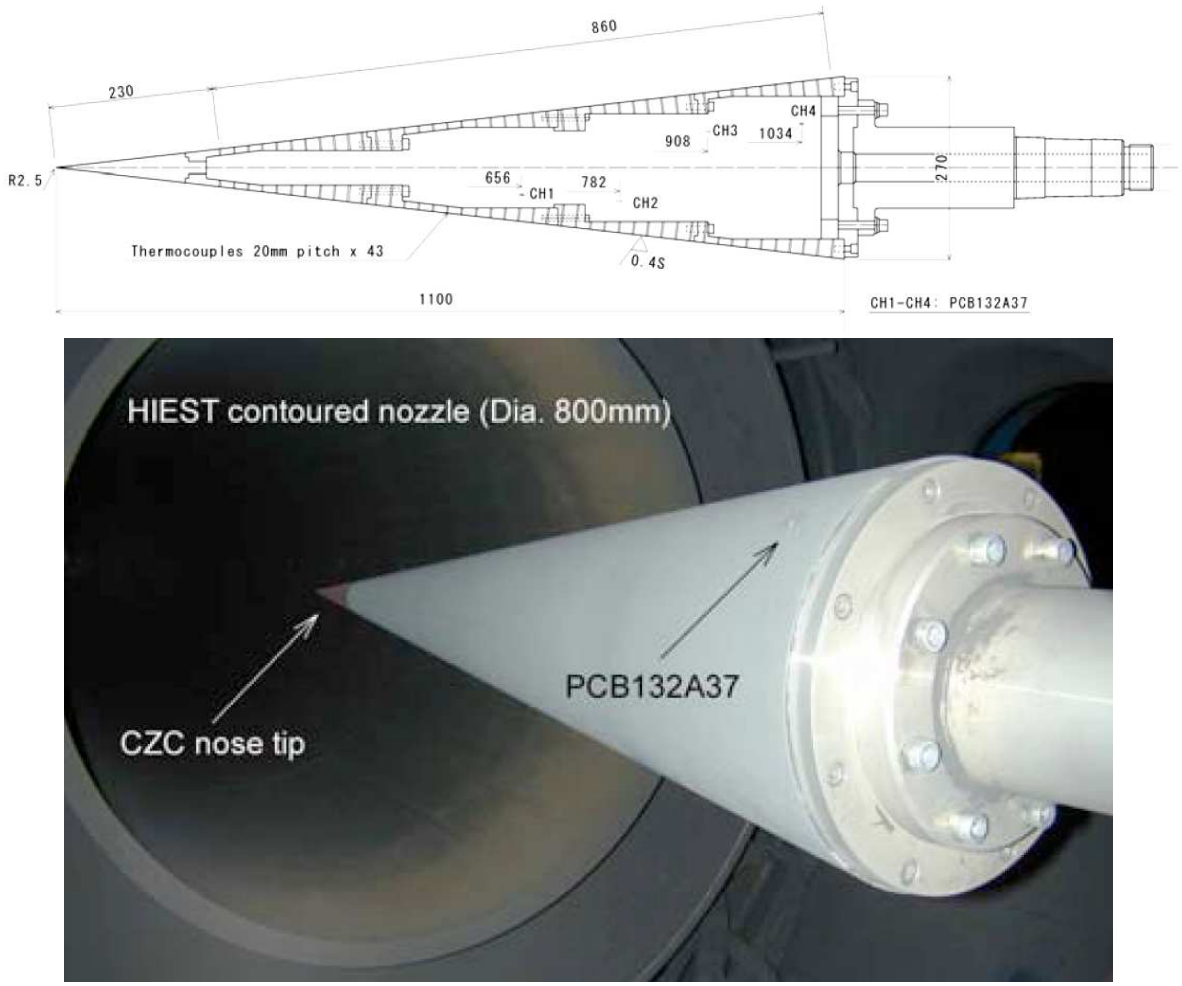

Figure 4.2: HIEST 7° half angle cone model schematic (top) and photograph (bottom).

Several runs were made during the first campaign of transition experiments. The stagnation pressure was held approximately constant at 30 MPa throughout the runs while the stagnation enthalpy was varied from 3.3 MJ/kg to 8.7 MJ/kg. Four runs were selected to be used for comparison to computational analysis and were chosen for two reasons. First, the conditions of these four cases spanned a range that was representative of this first campaign. Second, they were identical to the four cases presented in Tanno *et al*[40]. These runs included: shot 1717, 1719, 1721, and 1732. The freestream conditions and chemical compositions which were provided[1]

are shown in Table 4.2 and Table 4.3. See Tanno *et al.*[40] for more details about the transition experiments investigated here.

Shot #:	1717	1719	1721	1732	
M	7.709	7.281	6.5	7.684	–
P_0	31.553	27.429	31.036	30.793	MPa
H_0	3.255	4.747	8.169	3.347	MJ/kg
T_∞	243.7	394.6	843.7	251.7	K
$T_{v\infty}$	372.4	463.5	848.3	375.4	K
ρ_∞	0.0382	0.0236	0.0163	0.0365	kg/m^3
R_∞	5.88×10^6	3.01×10^6	1.62×10^6	5.55×10^6	$1/m$
u_∞	2413.8	2895.4	3720.9	2445.2	m/s
T_{wall}	300	300	300	300	K

Table 4.2: HIEST freestream conditions.

Species	Shot 1717	Shot 1719	Shot 1721	Shot 1732
N_2	0.740189	0.732028	0.726089	0.739077
O_2	0.214367	0.204934	0.192307	0.213140
NO	0.032566	0.049863	0.061542	0.034899
N	0.000000	0.000000	0.000000	0.000000
O	0.000021	0.000314	0.007175	0.000026
Ar	0.012857	0.012861	0.012887	0.012858

Table 4.3: HIEST freestream composition.

Additional operational conditions were created in order to identify an operational range for the HIEST shock tunnel where high enthalpy effects are predicted to have the greatest influence on boundary layer stability. These conditions were determined by using the unit Reynolds numbers and Mach numbers from the four selected shots in the original experiment and varying the freestream static temperature. The test conditions used for these cases are shown in Table 4.4. The freestream chemical composition was assumed to consist only of 76.7% diatomic nitrogen

[1] H. Tanno, private correspondence, 2009.

by mass and 23.3% diatomic oxygen by mass. A plot summarizing the range of conditions that the HIEST facility can provide is shown in Figure 4.3 and includes the conditions for the cases considered herein.

	$R_\infty = 5.7 \times 10^6$			$R_\infty = 5.4 \times 10^6$			$R_\infty = 3.0 \times 10^6$			$R_\infty = 1.6 \times 10^6$			
M	7.70	7.70	7.70	7.70	7.70	7.70	7.30	7.30	7.30	6.50	6.50	6.50	–
T_0	2717	6108	7715	2780	6429	8063	3651	6995	8744	5214	11340	13703	K
H_0	3.26	6.16	7.78	3.35	6.48	8.11	4.75	7.06	8.82	8.17	11.44	13.82	MJ/kg
T_∞	244	475	600	252	500	625	395	600	750	844	1200	1450	K
ρ_∞	0.0382	0.0451	0.0470	0.0365	0.0432	0.0448	0.0236	0.0261	0.0269	0.0163	0.0169	0.0172	kg/m^3
u_∞	2417	3371	3789	2449	3458	3867	2905	3592	4016	3792	4523	4972	m/s
T_{wall}	300	300	300	300	300	300	300	300	300	300	300	300	K

Table 4.4: HIEST additional freestream conditions.

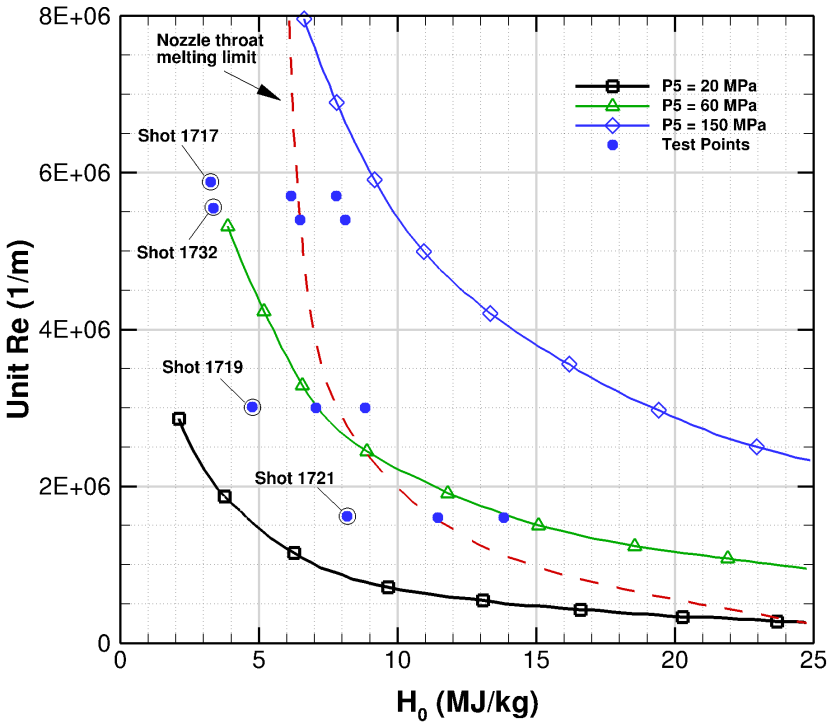

Figure 4.3: HIEST operational map. The four shots from the experiment are highlighted. The red dashed line indicates the tunnel's CZC (chrome-zirconia-copper) throat melting limit.

4.3 Numerical Setup

4.3.1 Mean Flow Solutions

ll of the cases selected for computational analysis were simulated using structured two-dimensional grids. The grids were constructed using the grid tailoring routines provided with STABL which are based on the methods used in the NASA OUTBOUND code[54]. This provides grids where the outer boundary closely follows the bow shock shape. Clustering was used in the grid to ensure that regions of strong gradients were appropriately resolved. A value of y^+ less than unity at the first solution point away from the wall was used as the criterion for adequate grid resolution of the boundary layer and each grid conformed to standard grid cell stretching metrics. A mean flow grid of size 660×300 was used for all the HIEST calculations. A zoomed-in look at the nose region of a typical grid is shown in Figure 4.4.

The laminar mean flow solutions were generated using a two-dimensional/axisymmetric, second order accurate mean flow solver based on the implicit data-parallel line relaxation (DPLR) method[20]. The governing equations are the Navier-Stokes equations with extensions for multiple species gas mixtures. A two-temperature model is used, where the combination of translational and rotational energies are characterized by the single translational temperature T, and the energy in the vibrational modes is characterized by the temperature T_v. The species diffusion velocity is governed by Fick's law of diffusion and the mass diffusion constant D is determined by assuming a constant Schmidt number for all species. The species viscosity is formulated in a way such that multiple viscosity models may be used over the range of temperatures and a smooth blending function handles the transitions. Due to the temperature ranges observed in the work, two models, Sutherland's viscosity law and Blottner's viscosity model[55] were used. Extensive studies have been conducted to validate the DPLR CFD solver and the stability analysis code for linear stability theory (LST) and PSE calculations.[16, 56, 57]

For all of the cases evaluated in this work, certain assumptions were made in the absence of experimental data. As such, an isothermal wall temperature of 300 K was assumed and used for all of the simulations. Two CFD simulations were run for each case, since the run times were very brief, where one simulation was run with translation-vibrational energy exchanges and finite rate reactions allowed to occur and the other with both translation-vibrational energy exchanges and finite rate reactions frozen. An example plot of the flowfield for shot 1719 shown in Figure 4.5 shows temperature contours and is typical of the computations made.

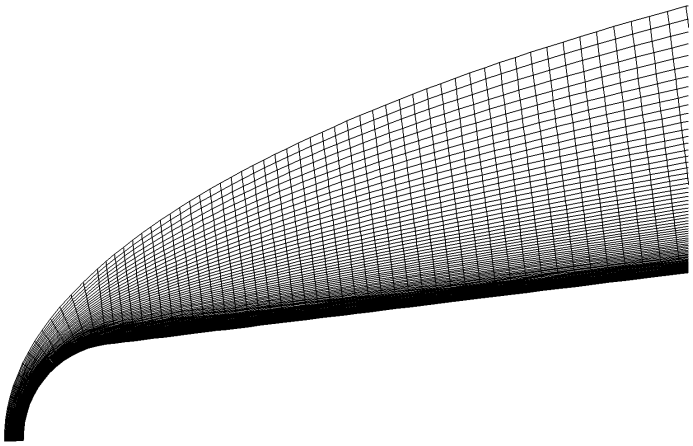

Figure 4.4: Typical grid in nose region (de-refined for clarity).

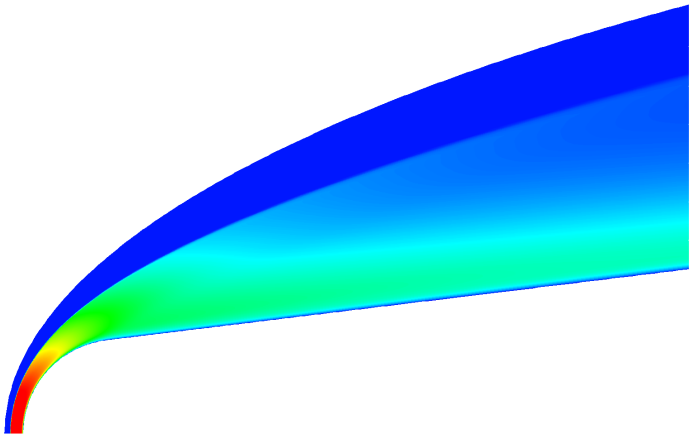

Figure 4.5: Temperature contours in nose region for Shot 1719.

4.3.2 Stability Analysis

Boundary layer stability analyses were conducted using the PSE-Chem module in the STABL suite of software. The PSE-Chem code solves the parabolized stability equations for high speed flows and includes the effects of finite-rate chemistry and translation-vibrational energy exchanges. This allows one to track the growth and evolution of disturbances in supersonic and hypersonic boundary layers. A summary of the derivation of linear stability theory, the parabolized stability

equations, and their implementation in STABL can be found in Appendix A. For a more detailed description the reader is referred to Johnson[58] and Johnson and Candler[16]. One particularly useful quantity is the N factor from the e^N method. Briefly, this method provides a means to measure the integrated amplitude growth of constant frequency disturbances in the boundary layer as they propagate downstream. Following Jaffe *et al.*[59] this quantity can then be compared to experimental transition data to determine a particular value of the N factor which correlates to transition. The N factor is defined as follows:

$$N(\omega, s) = \int_{s_0}^{s} \sigma ds$$

where s is the distance along the surface, s_0 is the the location of the first critical point, ω is the disturbance frequency, and σ is the disturbance growth rate as defined by:

$$\sigma = -Im(\alpha) + \frac{1}{2E}\frac{dE}{ds}$$

In this equation, α is the complex stream-wise wavenumber and E is the disturbance kinetic energy which is defined as follows:

$$E = \int_{n} \bar{\rho}\left(|u'|^2 + |v'|^2 + |w'|^2\right) dn$$

where $\bar{\rho}$ is the mean flow density, (u', v', w') are the complex fluctuating velocity components, and n is the direction normal to the body surface. Using either LST or PSE to compute the N factors, comparisons with experiments where transition data is available have shown that for smooth-surfaced geometries in low disturbance environments the N factor correlating to transition occurs in the range of 8-11[59, 60, 61]. When applied to transition studies conducted in higher disturbance environments, such as conventional wind tunnels and shock tunnels, the corresponding N factor of transition is reduced to approximately 5.5[62, 63, 64, 65].

For practical application, a graphical user interface is included with STABL along with an object oriented scripting interface which allows for basic automation of operations. These features streamline the process of conducting stability analyses, which in the absence of such features might result in tedious repetition. STABL has also been designed to utilize the message passing interface (MPI) library to efficiently distribute the required calculations on parallel computing resources. The automatic test matrix feature provided in PSE-Chem was used to set up an initial stability

analysis for each case. This feature uses estimates of frequencies for first mode and second mode disturbances and places test points to cover both. An example of the test matrices used from the automatic matrix generator is plotted in Figure 4.6. When necessary, these results were appended manually by adding additional test points in regions where the initial results were incomplete.

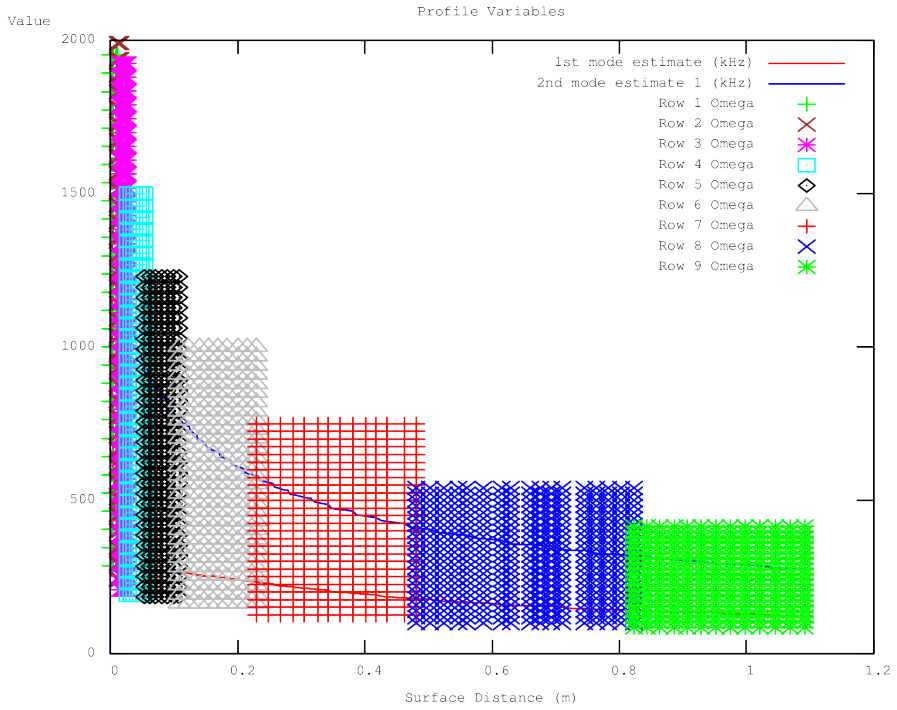

Figure 4.6: Example PSE-Chem automatic test matrices for stability analysis of shot #1719.

4.4 Results

Stability analyses were conducted for each of the four shots from the experiment as well as for the additional operational conditions. The normalized heat flux data which were provided from the experiment were compared to the computed normalized laminar heat transfer rate in order to determine the approximate location of transition. The heat flux data were normalized using the heat flux value at the axial location, $x = 210$ mm.

For shot #1717, Figure 4.7a shows the N factor envelope and a comparison between normalized surface heat flux from the experiment and from the calculations. Figures 4.7b, 4.7c, and 4.7d provide similar results from shots #1719, #1721, and #1732, respectively. Dotted lines indicating the estimated location of transition and corresponding N factors are also provided in these figures.

These estimated transitions location and N factor values are tabulated in Table 4.5. Qualitatively, transition of the boundary layer appears to occur at some location along the length of the cone for three of the four shots, but for shot #1721 the flow remains entirely laminar.

Recalling previous observations in both conventional wind tunnels and shock tunnels, it has been documented that a value of $N = 5.5$ typically corresponds to the onset of transition. In contrast, for these four cases, a value of $N = 8$ appears to correlate the onset of boundary layer transition. This difference might be attributed to the fact that the $N = 5.5$ value has been more commonly applied to cold flow hypersonic facilities[66] whereas an N factor of transition for flows where high-enthalpy effects are influential on boundary layer transition has not be quantified.

This difference may be attributed to the fact that high enthalpy effects on boundary layer transition have not been quantified, since the $N = 5.5$ value has been more commonly applied to cold flow hypersonic facilities[66].

One last observation regarding Figures 4.7a, 4.7b, 4.7c, and 4.7d: if these plots were rearranged in order of increasing unit Reynolds number as follows, shot #1721, #1719, #1732, and lastly #1717, there would be the observable trend that as the freestream unit Reynolds increases, the location of the transition front moves upstream. This is the effect that one would expect the Reynolds number would have on transition.

	Shot #1717	Shot #1719	Shot #1721	Shot #1732
Axial Location	660 mm	926 mm	$>$ 1100 mm	672 mm
N Factor	8.0	7.7	> 6.7	8.0

Table 4.5: Approximate Transition Locations.

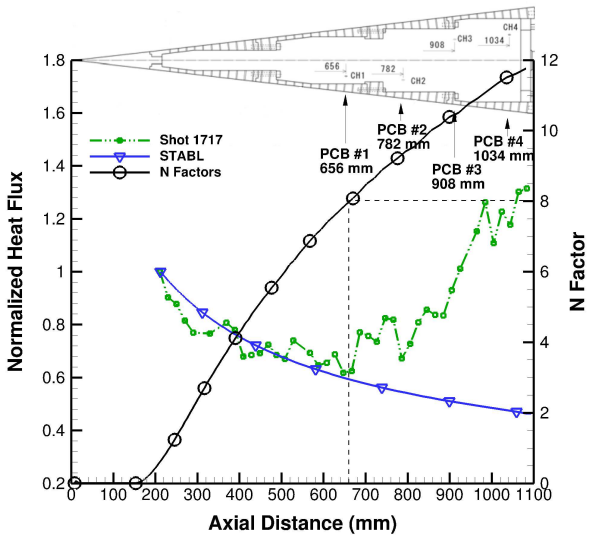

(a) Shot #1717.

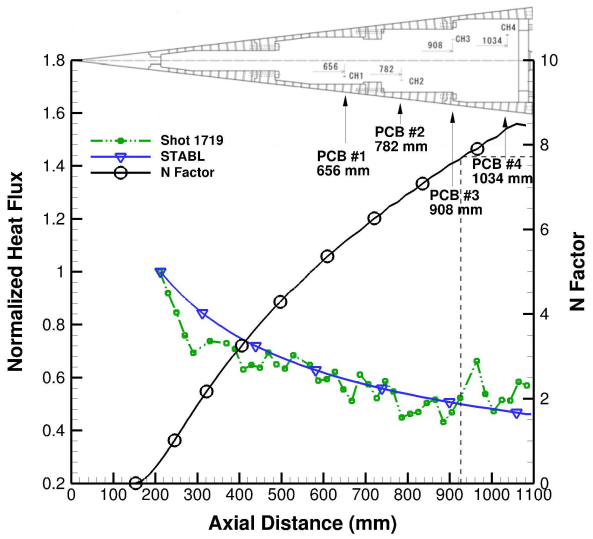

(b) Shot #1719.

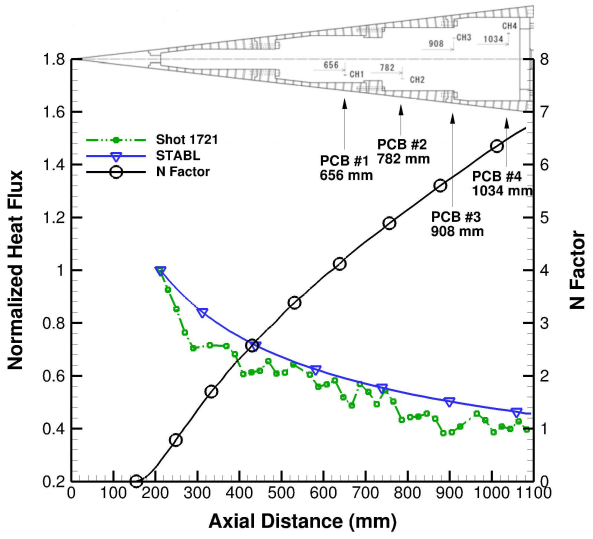

(c) Shot #1721.

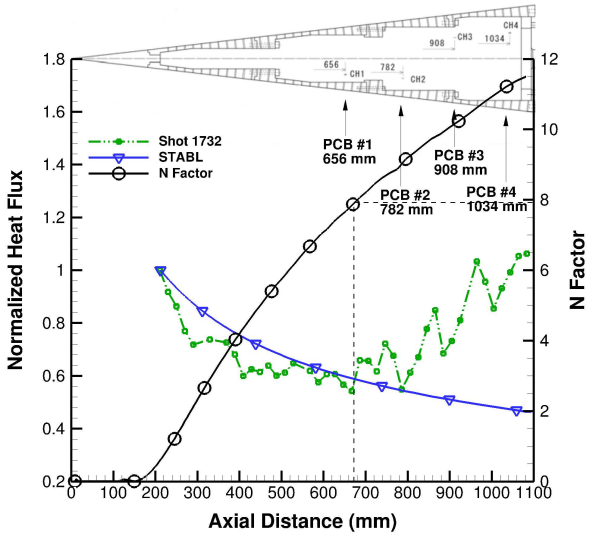

(d) Shot #1732.

Figure 4.7: HIEST heat flux and N factors. Transition locations were estimated to be at the location where the experimental heat transfer first diverges from the laminar calculation. A schematic of the cone model with indicators showing the installation locations of the pressure transducers is included on the plots.

With transition locations and transition N factors having been considered for these cases, attention can now be turned toward determining which type of disturbances are present and are most amplified in the computations. Stability diagrams can provide quick insights toward the identification of disturbances. The stability diagrams shown in Figure 4.8 were generated using LST and are plotted along with lines showing first and second mode frequency estimates. Also plotted are lines for the maximum amplified frequencies which correspond to the N factor curves from above. Examining these stability diagrams, it can be immediately observed that there is only one region of instability. The curve showing the frequencies corresponding to the maximum N factors passes through this region and more closely resembles the expected frequency range from the second mode estimate. Therefore, based on preliminary indicators, the second mode instability is the dominant mode observed in the computational analysis.

To confirm that the disturbances are indeed second mode in nature, pressure disturbance eigenfunctions were extracted from the PSE analysis at an axial location of 656 mm for three different frequencies. The frequencies and location were specifically chosen to aid in the analysis of the experimental pressure fluctuation observations in Figure 4.12a, to be discussed below. The normalized pressure disturbance amplitude is shown in Figure 4.9 for the three frequencies 450 kHz, 500 kHz, and 550 kHz. These curves were normalized using the value of the disturbance pressure amplitude at the wall. In Figure 4.10, the pressure disturbance amplitude phase is plotted for the 500 kHz frequency. For convenience, only one frequency was shown but is characteristic of all three frequencies. What can be observed is that the shapes in both plots are indicative of a second mode disturbance, similar to observations by Johnson[58]. As Mack[25] observed, the pressure amplitude plots show two peaks which are characteristic of second mode disturbances. It should be noted that Mack plotted the real component of the eigenfunction, whose values cross zero amplitude, whereas in this work they do not. The single change in the pressure disturbance phase is also considered characteristic of second mode disturbances.

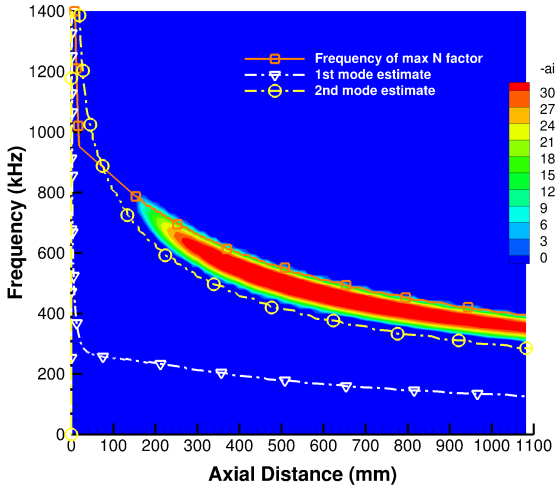

(a) Shot #1717.

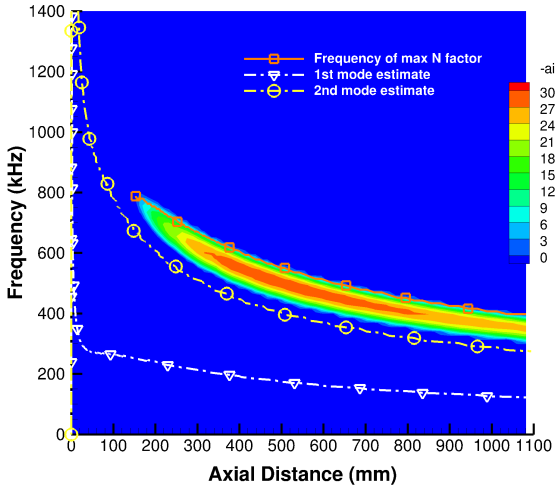

(b) Shot #1719.

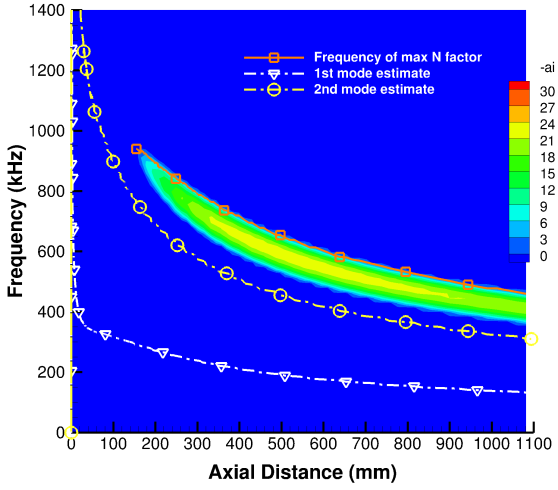

(c) Shot #1721.

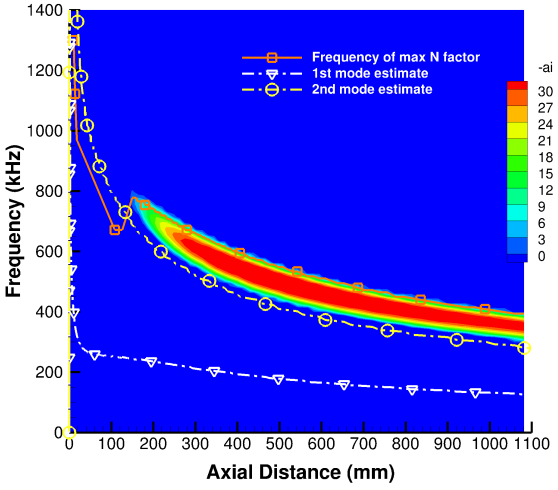

(d) Shot #1732.

Figure 4.8: Stability diagrams for the HIEST transition experiments. Note the presence of only a single region of instability. Frequencies from the maximum N factor pass through this region which are both similar in frequency range to the second mode estimate.

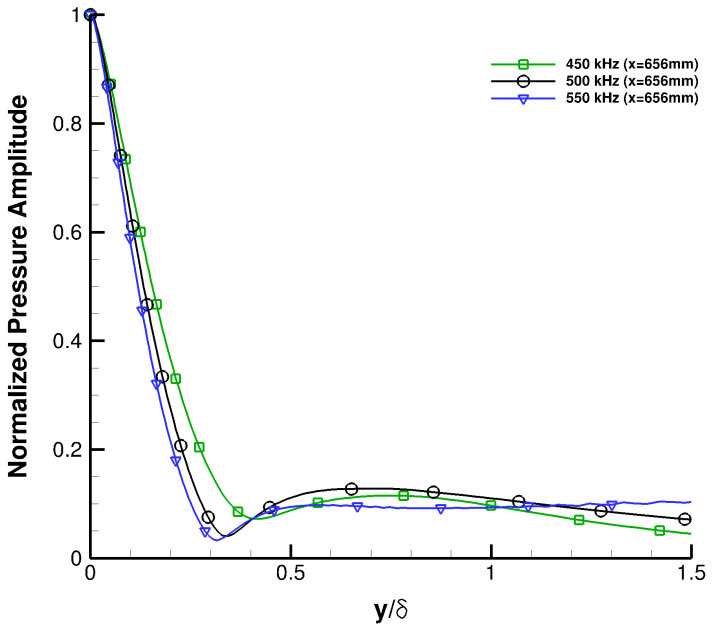

Figure 4.9: Normalized amplitude of the pressure disturbance eigenfunction at the axial location $x = 656$ mm.

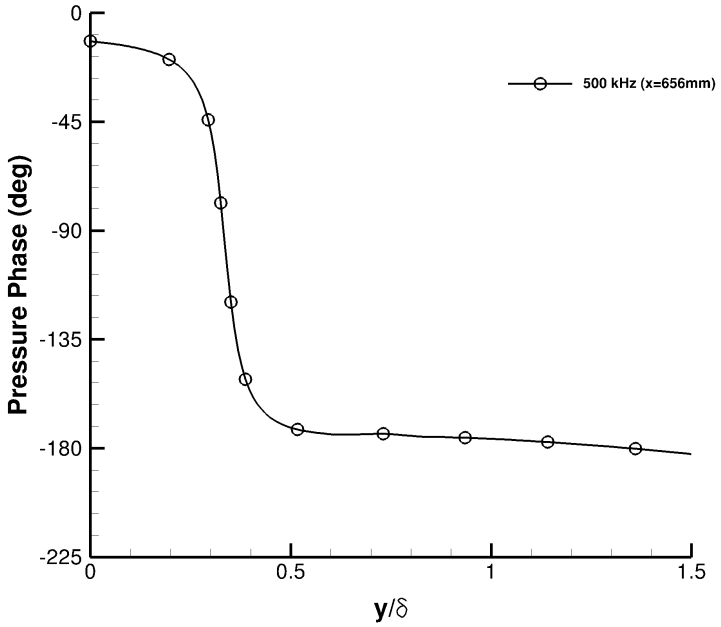

Figure 4.10: Phase of the pressure disturbance eigenfunction at the axial location $x = 656$ mm.

One of the main goals of the HIEST transition experiment was to directly measure the disturbance frequencies within boundary layer. As such, four pressure transducers were installed into the cone model. The locations of these transducers are indicated on the N factor and heat flux plots in Figure 4.7. From the measured surface pressure fluctuations, the power spectra at each transducer were determined using standard Fourier analysis[40]. The power spectra for each shot at each pressure transducer location are qualitatively compared to N factors versus frequency and are shown in Figures 4.11-4.14.

For shots #1717 and #1732, the boundary layer is experimentally shown to have already begun the transition process upstream of all the pressure transducer locations, resulting in a broadening of the power spectra. Therefore, the comparisons between the experimental power spectra and the N factors versus frequency are expected not to show any conclusive relationship, which is readily apparent when examining these two cases. However, for shots #1719 and #1721, the boundary layer either remains entirely laminar or only begins to transition to turbulence at a location somewhere within the range of the pressure transducer locations. While there is significant noise in the experimental data, the plots for the transducer locations where the flow is still laminar show a general agreement of the frequency range between the computations and experiment. This is especially true for the cases where the disturbances have been significantly amplified, typically just upstream of the transition front, that they overwhelm the noise in the experimental data and are more readily identifiable. For example, see Figures 4.12a, 4.12b, 4.13c, and 4.13d. This result shows that, for high enthalpy flows similar to these, PSE with appropriate thermochemical and vibrational modeling can provide consistent results with measured pressure fluctuations. It should be noted that the two frequencies, 190 kHz and 340 kHz, indicated in each of the power spectra plots represent the resonant frequencies of the cone model as determined experimentally by a hammer test.

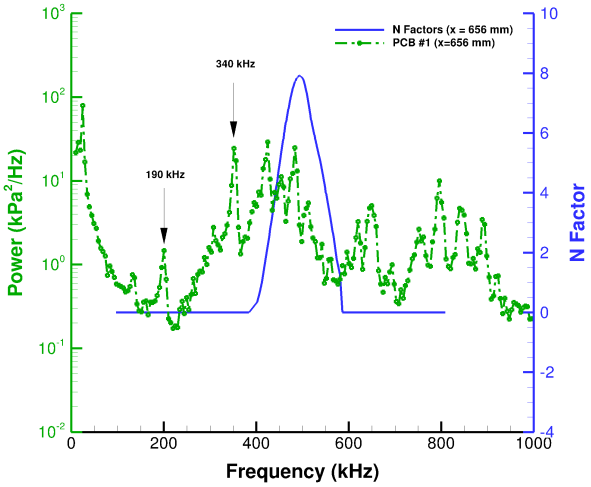

(a) Pressure transducer at x=656 mm (CH1).

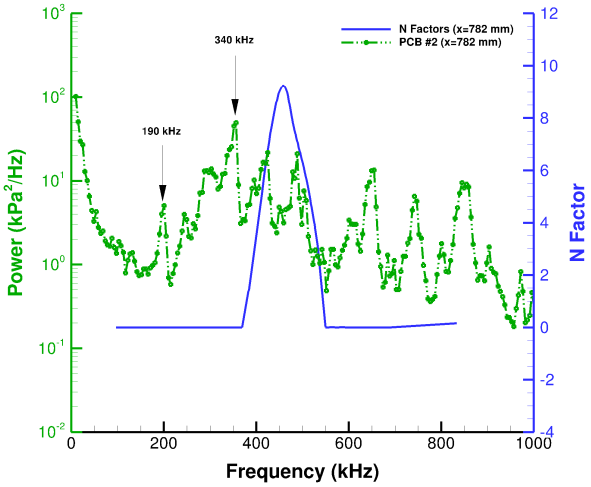

(b) Pressure transducer at x=782 mm (CH2).

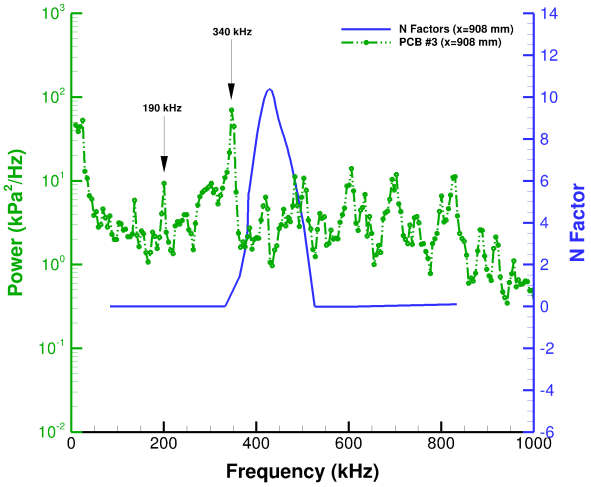

(c) Pressure transducer at x=908 mm (CH3).

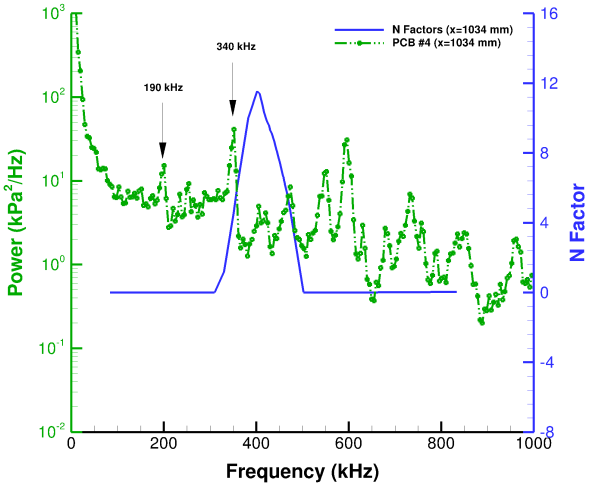

(d) Pressure transducer at x=1034 mm (CH4).

Figure 4.11: Shot #1717. As indicated in Figure 4.7a, it is estimated that all four transducer locations are downstream of the transition front. Therefore, as expected, the computations do not match the experimental observations.

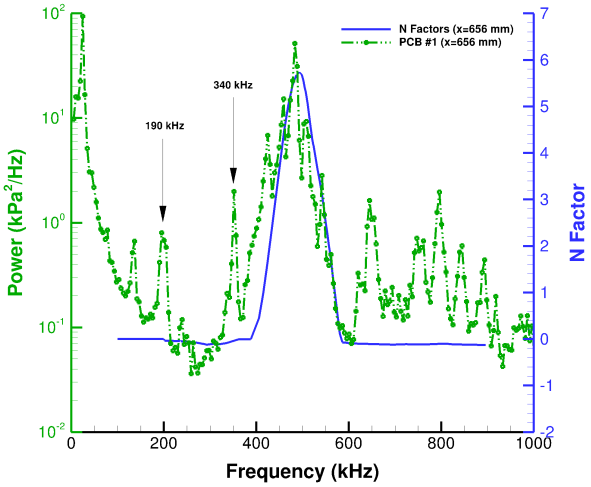

(a) Pressure transducer at x=656 mm (CH1).

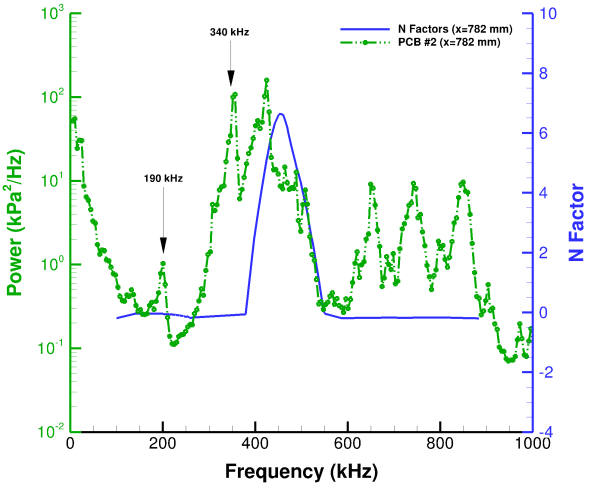

(b) Pressure transducer at x=782 mm (CH2).

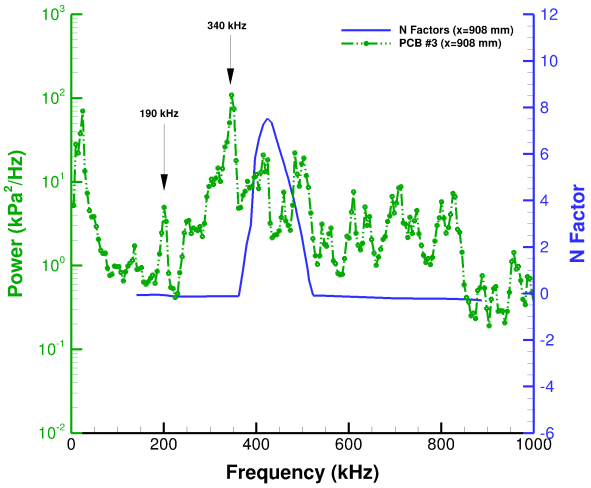

(c) Pressure transducer at x=908 mm (CH3).

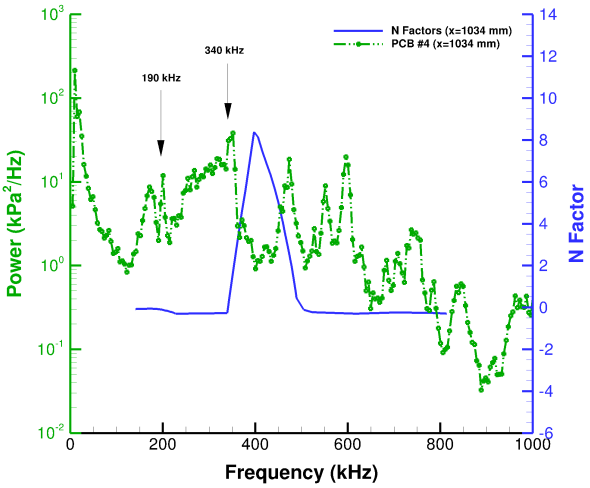

(d) Pressure transducer at x=1034 mm (CH4).

Figure 4.12: Shot #1719. Note the good frequency range agreement between experiment and computations in (a) and (b). In figures (c) and (d) there is a noticeable broadening of the measured spectrum indicating transition.

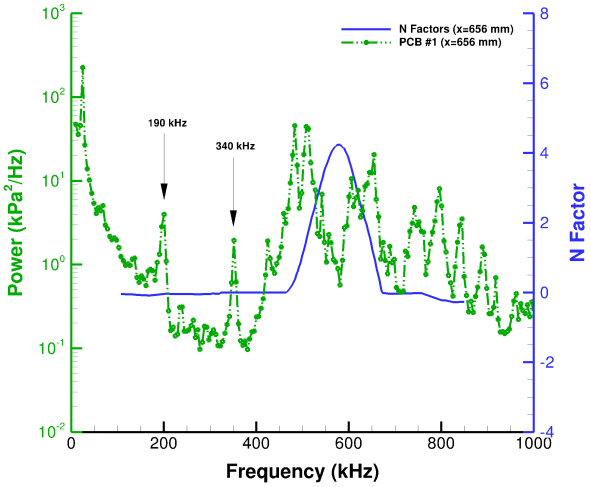

(a) Pressure transducer at x=656 mm (CH1).

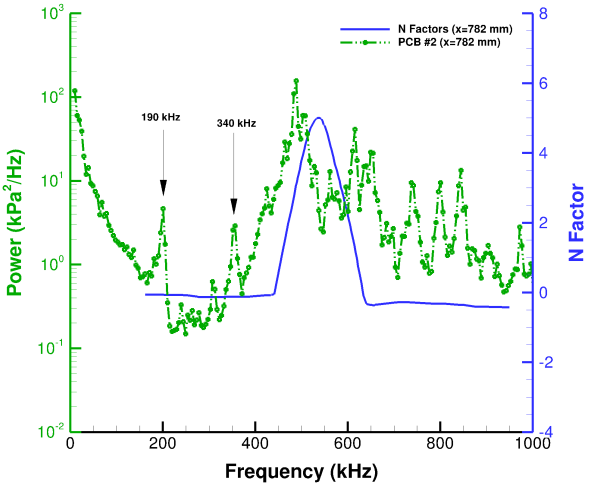

(b) Pressure transducer at x=782 mm (CH2).

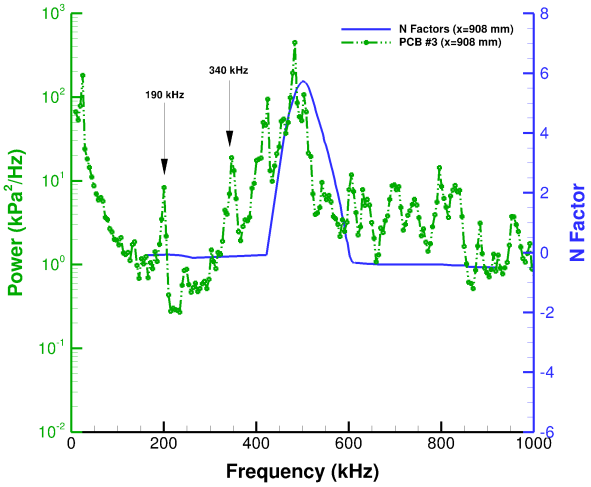

(c) Pressure transducer at x=908 mm (CH3).

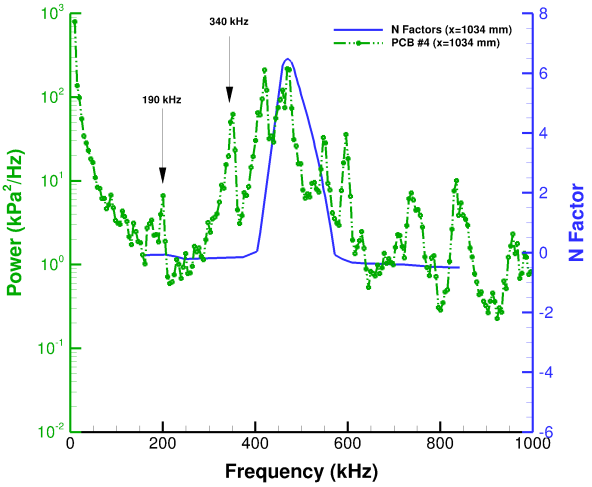

(d) Pressure transducer at x=1034 mm (CH4).

Figure 4.13: Shot #1721. In figure (a) and to a lesser extent (b) it is difficult to ascertain any dominant range of disturbances in this fully laminar case. However, nearing the end of the cone there appears to be greater agreement between computations and experiment.

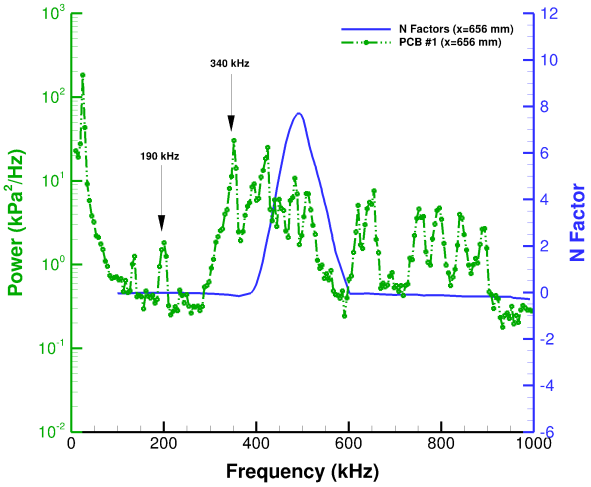

(a) Pressure transducer at x=656 mm (CH1).

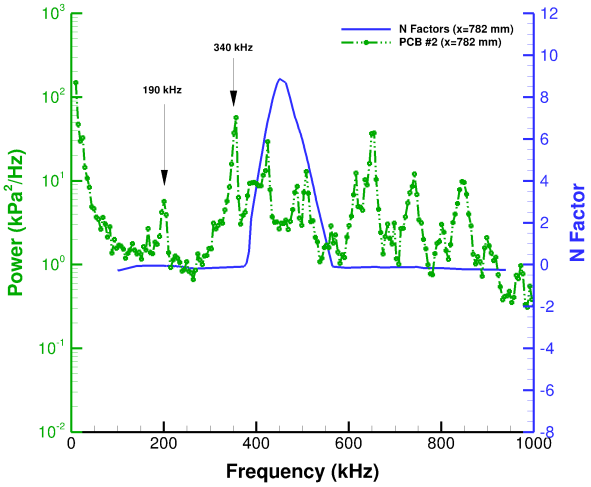

(b) Pressure transducer at x=782 mm (CH2).

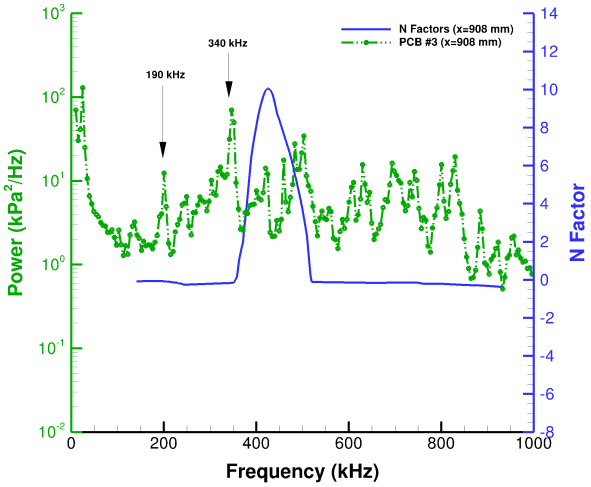

(c) Pressure transducer at x=908 mm (CH3).

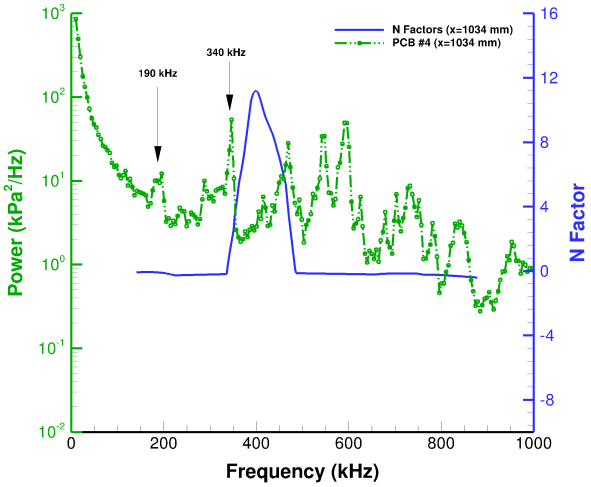

(d) Pressure transducer at x=1034 mm (CH4).

Figure 4.14: Shot #1732. As was the case with shot #1717, this case was arguably transitional prior to the transducer locations. Therefore, broadening of the spectrum was expected.

Additional cases have been examined at selected freestream conditions in order to identify an operational range for the shock tunnel where high enthalpy effects are predicted to have the greatest effect on boundary layer stability. These test points, which include the four shots from the experimental campaign, are indicated with blue dots in Figure 4.3. Using N factors, a comparison of enthalpy effects on boundary layer stability is shown for each freestream unit Reynolds number

in Figure 4.15. Taking a detailed look at the highest freestream unit Reynolds case in Figure 4.15a, it can be observed that as the freestream stagnation enthalpy is increased from 3.3 MJ/kg to 6.2 MJ/kg to 7.8 MJ/kg there is a corresponding destabilization of the boundary layer as indicated by the increasing N factors. Examining the lowest freestream unit Reynolds case in Figure 4.15d, an identical trend is observed as the stagnation enthalpy is increased over the baseline 8.2 MJ/kg. However, counteracting this trend is the stabilizing effect of the decrease in the unit Reynolds number, which can be observed by noting the general decrease in N factors as one moves from the highest unit Reynolds number plot toward the lowest unit Reynolds plot. Due to operational constraints, such as the nozzle throat melting limit, this reduction in unit Reynolds number is required to achieve higher stagnation enthalpies.

Next, the effects of chemical dissociation and vibrational relaxation on boundary layer stability were examined for the eight additional operational conditions. For this study, two mean flow solutions were generated, one where finite-rate chemistry and vibrational relaxation effects were disallowed and the other with both effects allowed. For the non-reacting mean flow, a stability analysis was conducted, also without chemistry and vibrational effects. For the reacting mean flow, two stability analyses were conducted, one reacting and one non-reacting. Again, plots of N factors provide the basis of comparison and are shown in Figures 4.16-4.19. When examining the highest unit Reynolds number case in Figures 4.16a and 4.16b it can be noted that the increase in stagnation enthalpy results in an increase in the difference between the stability of the boundary layer for the reacting and non-reacting calculations. This difference is primarily driven by the change in the mean flow solution from the CFD solver, depending on whether chemical dissociation and vibrational relaxation modeling were used or not. At these conditions, it can also be noted that adding thermochemical modeling to the stability analysis had a negligible effect. Similar to the highest unit Reynolds case, the lowest unit Reynolds case also demonstrates that increasing stagnation enthalpy produces an increased effect on boundary layer stability. However, at the highest stagnation enthalpy, 13.8 MJ/kg, there is a small but noticeable difference between the stability analyses run with and without thermochemical modeling. Again, as previously noted, the effect of increasing stagnation enthalpy is more than offset by the required decrease in freestream unit Reynolds number.

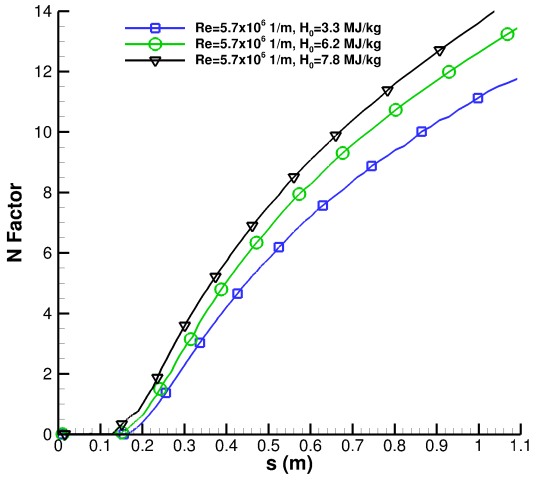

(a) Comparison of N factors for $R_\infty = 5.7 \times 10^6$ 1/m.

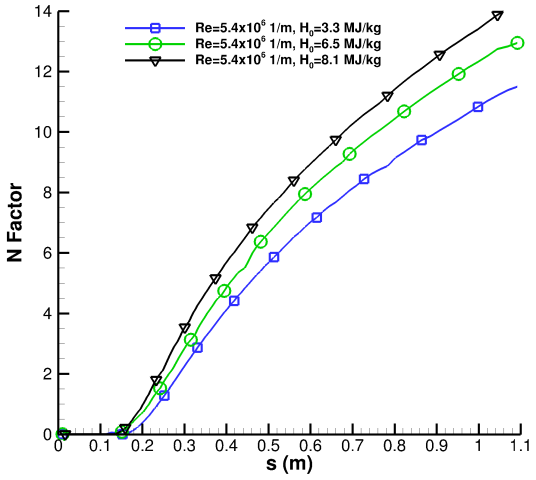

(b) Comparison of N factors for $R_\infty = 5.4 \times 10^6$ 1/m.

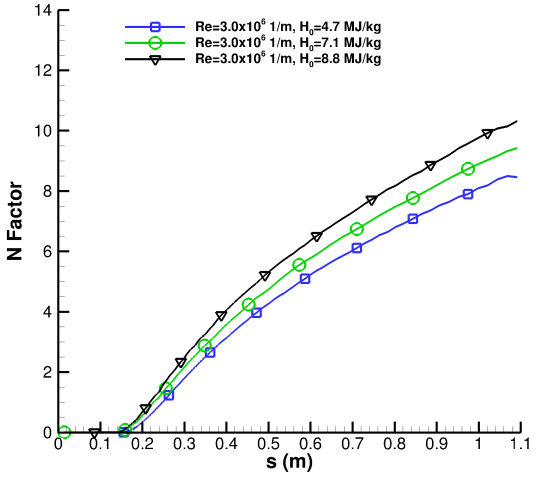

(c) Comparison of N factors for $R_\infty = 3.0 \times 10^6$ 1/m.

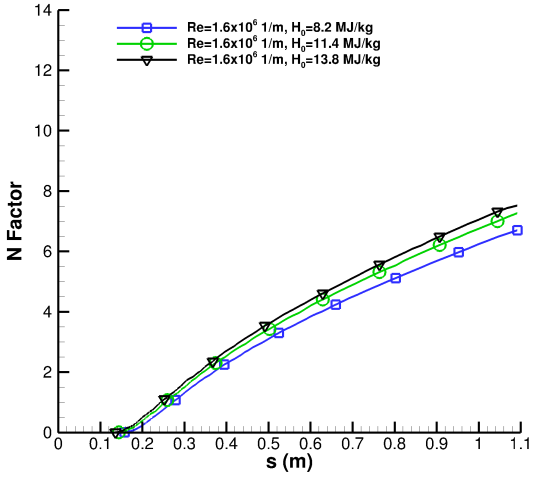

(d) Comparison of N factors for $R_\infty = 1.6 \times 10^6$ 1/m.

Figure 4.15: HIEST freestream stagnation enthalpy effects.

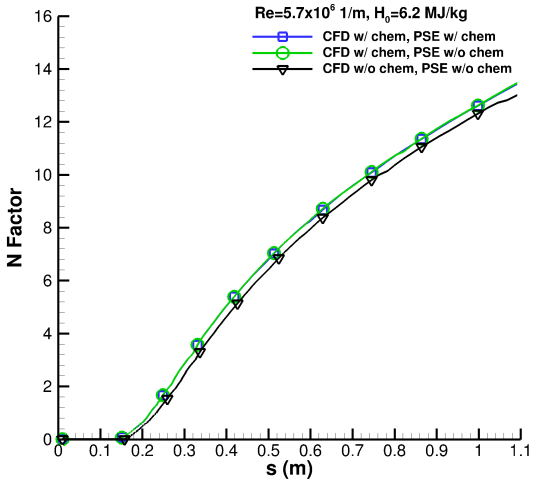

(a) $H_0 = 6.2\ MJ/kg$

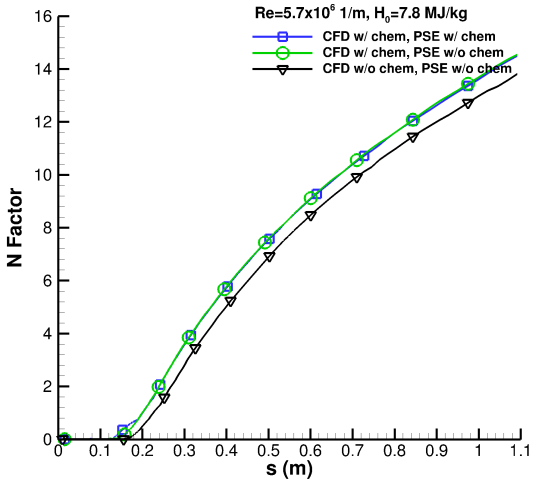

(b) $H_0 = 7.8\ MJ/kg$

Figure 4.16: Comparison of chemistry and vibration effects on N Factors for $R_\infty = 5.7 \times 10^6$.

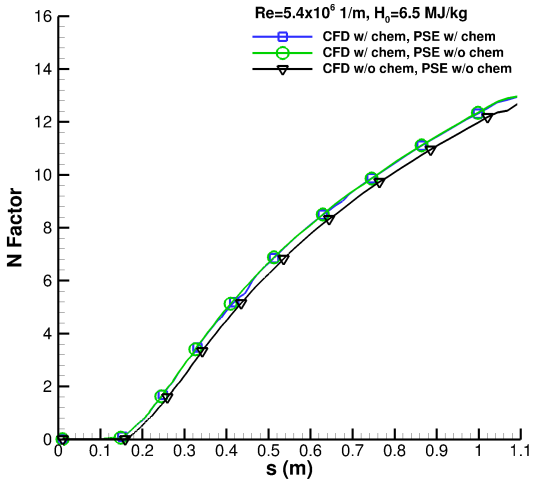

(a) $H_0 = 6.5\ MJ/kg$

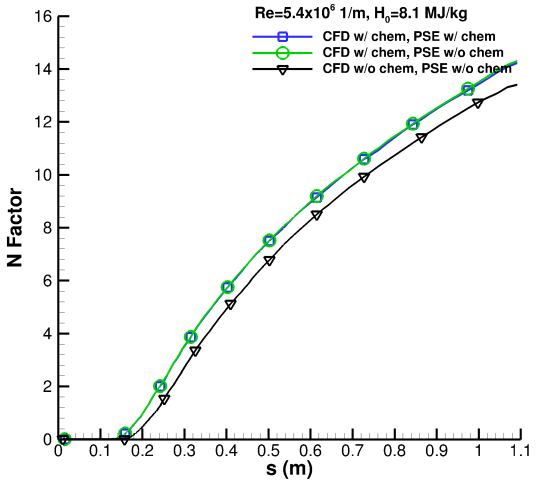

(b) $H_0 = 8.1\ MJ/kg$

Figure 4.17: Comparison of chemistry and vibration effects on N Factors for $R_\infty = 5.4 \times 10^6$.

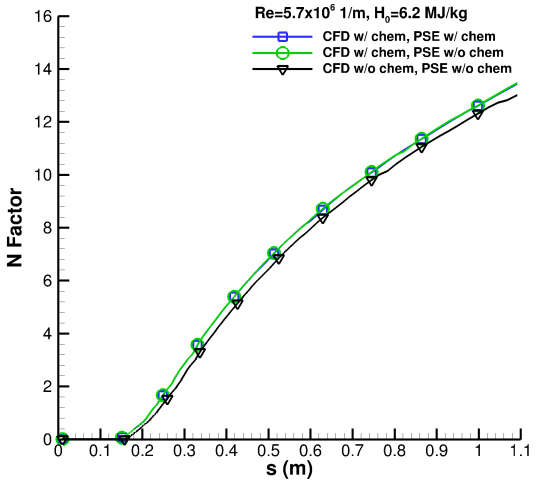

(a) $H_0 = 7.0\ MJ/kg$

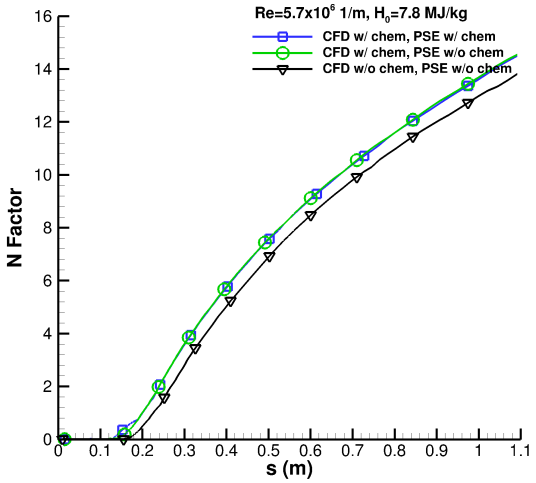

(b) $H_0 = 8.8\ MJ/kg$

Figure 4.18: Comparison of chemistry and vibration effects on N Factors for $R_\infty = 3.0 \times 10^6$.

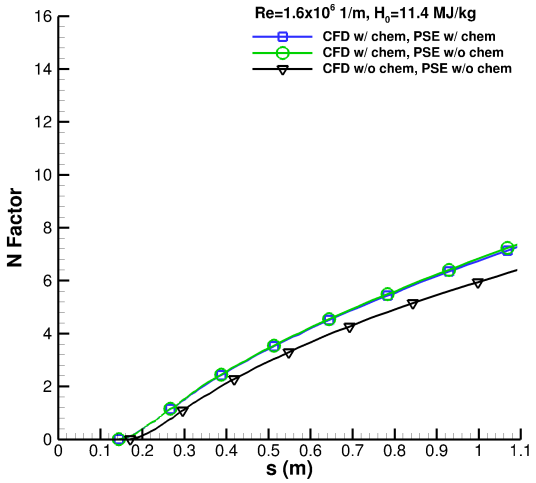

(a) $H_0 = 11.4\ MJ/kg$

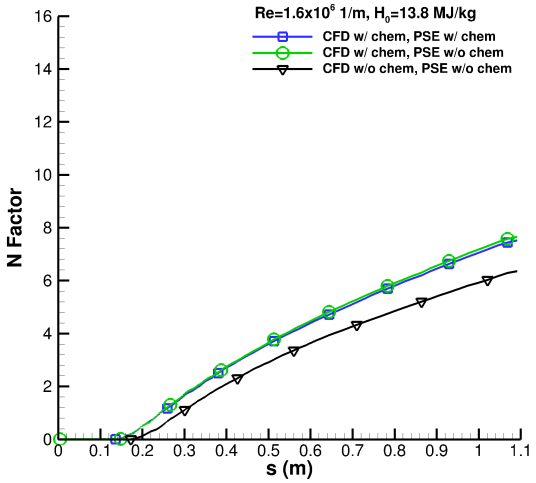

(b) $H_0 = 13.8\ MJ/kg$

Figure 4.19: Comparison of chemistry and vibration effects on N Factors for $R_\infty = 1.6 \times 10^6$.

To gain a better understanding of what is shown in Figures 4.16-4.19, it is useful to examine the amplification rates of some representative frequencies. The case with a unit Reynolds number of 1.6×10^6 1/m and stagnation enthalpy of 13.8 MJ/kg will be investigated since it showed

the greatest influence of finite-rate chemical kinetics and internal energy relaxation on boundary layer stability. To provide clarity in the following discussion, the non-reacting mean flow with the non-reacting stability analysis will be referred to as the baseline case. The analysis which utilized the reacting mean flow in combination with a non-reacting stability analysis will be referred to as case A and the analysis which used the reacting mean flow in combination with a reacting stability analysis will be referred to as case B.

Four frequencies were selected for this examination and were chosen by taking the most amplified disturbance frequency at each pressure transducer location from case B. The disturbances selected were: 800 kHz at 656 mm, 742 kHz at 782 mm, 695 kHz at 908 mm, and 652 kHz at 1034 mm. In Figure 4.20 the amplification rate, α_i, is plotted versus the axial distance for the four frequencies. Due to the spatial stability formulation of the PSE method used for this work, disturbances are considered to be unstable when $\alpha_i < 0$. Therefore, the ordinate axis in this figure is formatted to reflect the negative values of α_i. Boundary layer temperature profiles have also been provided and are shown in Figure 4.21 for the furthest downstream pressure transducer location ($x = 1034$ mm) to aid this analysis.

It is again evident that the difference between the baseline case and case A is more significant than the difference between case A and case B. In addition, there is a noticeable downstream shift in the location of the amplification rate peaks going from the baseline case to cases A and B. To help illustrate this, two vertical lines denoting the peaks in amplification rates for the 652 kHz disturbance are shown. This downstream shift indicates that, in the absence of chemical kinetics modeling in the mean flow, the disturbance frequencies are generally lower. This is also reflected in the fact that the non-reacting boundary layer is thicker due to higher temperatures (see Figure 4.21), which results from the lack of endothermic reactions associated with the chemical kinetics and internal energy relaxation. Another observation may be made regarding Figure 4.21. As has been noted, there is a decrease in the boundary layer thickness (δ_{99}) going from non-reacting to reacting mean flow. The region of relative supersonic flow, that is, below the relative sonic line, also decreases in thickness. However, this decrease is much less than that of the boundary layer thickness which indicates that this region makes up a larger portion of the boundary layer in the reacting case. It has been noted that the thickness of this relative supersonic flow region can greatly influence the character of second mode disturbances[67].

Lastly, a general observation may be made concerning the baseline case versus cases A and B. That is, besides achieving larger amplification rates in cases A and B, the distance over which

a particular frequency is amplified is also broader. One possible explanation for this behavior is that the inclusion of chemical dissociation and vibrational effects have resulted in a boundary layer whose characteristics change more gradually with distance. To put it another way, for a boundary layer whose characteristics are changing slowly with distance, one might expect the region of amplification for an individual frequency to be greater than for a boundary layer whose characteristics change more rapidly with distance.

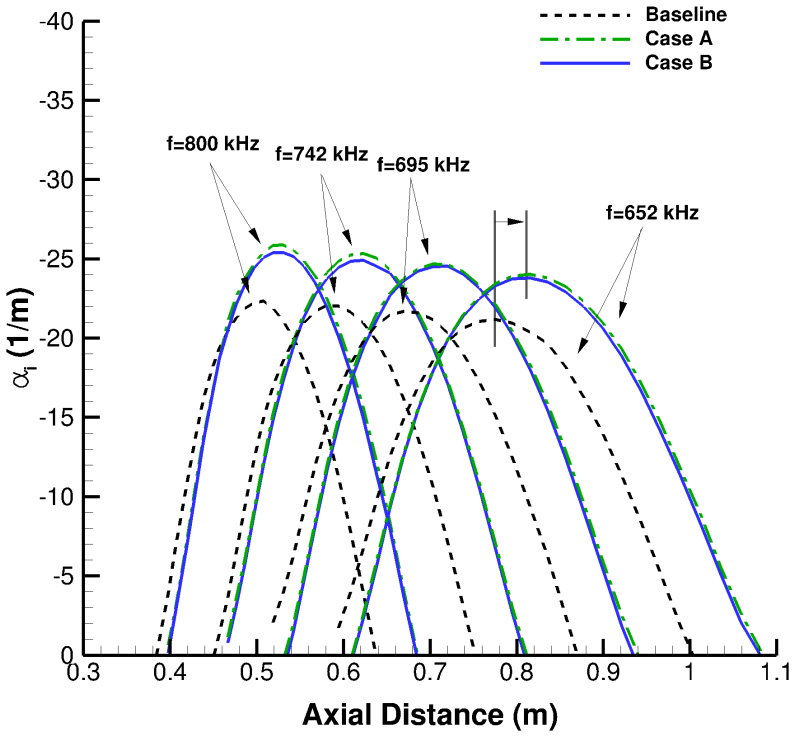

Figure 4.20: Comparison of chemistry and vibration effects on amplification rates for $R_\infty = 1.6 \times 10^6$ 1/m.

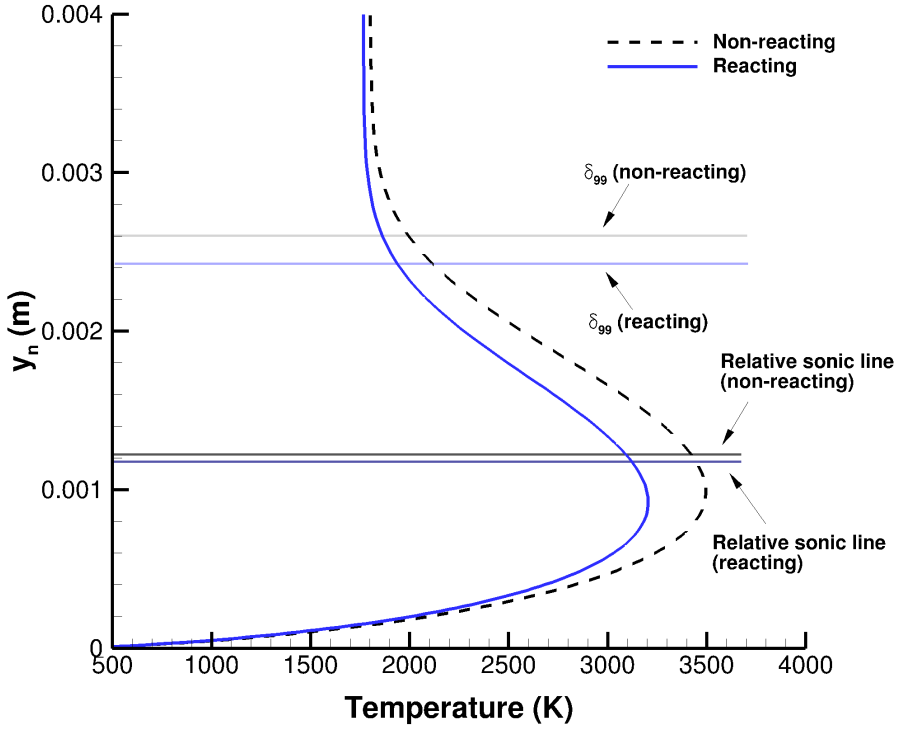

Figure 4.21: Comparison of chemistry and vibration effects on Temperature in the boundary layer for $R_\infty = 1.6 \times 10^6$ 1/m at $x = 1.034$ m.

Chapter 5

Slender Cone: Angle of Attack

5.1 Introduction

As previously mentioned, hypersonic boundary layer transition continues to be critical field of study with respect to re-entry vehicles. This is due to the need for an improved understanding of the complex nature of the transition process. Neglecting the transient growth and bypass paths to turbulence, boundary layer transition essentially starts with receptivity, moves to the linear growth of disturbances, and finally to nonlinear breakdown to turbulence. Making matters more complicated, re-entry vehicles often maneuver during their flight paths, resulting in three-dimensional flow fields on even the most simple of geometries. Therefore, while studies such as those discussed in the previous chapter are useful for investigating two-dimensional disturbances, they are obviously insufficient for studying disturbances that arise due to three-dimensionality of flows. In this chapter, the stability characteristics of a hypersonic three-dimensional boundary layer are investigated, with a specific focus on the so-called crossflow instability.

Historically, there have been three categories of flow fields that have been used to study the crossflow instability: rotating geometries, swept surfaces, and geometries at angle of attack. The first type, rotating geometries and specifically the rotating disk, initially found favor due to the availability of a similarity solution for the steady-state flow and the characteristic that this flow maintains both the profile shape and thickness of the boundary layer independent of the radius[68]. In addition to rotating disks, rotating axisymmetric cones have also been considered. It was observed that in quiescent flow conditions, centrifugal instabilities dominated on cones with half angles less than 30° while crossflow instabilities dominated on cones with half angles greater

than 30° with the additional observation that the presence of an axial flow lowered the threshold angle between the two regimes[69, 70]. However, it was discovered that an absolute instability existed at a Reynolds number of 510 for rotating disks[71] making the application of these types of problems limited. The second type, swept surfaces, has received considerable attention, especially at low-speeds. It has been considered that the crossflow instability was first discovered by Gray in 1952[72, 73] while observing transition on a swept wing. Consequently, Owen & Randall in 1952[74] examined this instability on a yawed infinite cylinder and introduced the crossflow Reynolds number, $w_{max}\delta/\nu$ as a criteria to correlate the onset of transition. Excellent reviews of work relating to swept surfaces can be found in Reed & Saric[75], Bippes[76], and Saric et al[77]. Of particular note, was the development of a swept wing laminar flow control developed by Saric & Reed[78] using appropriately placed discrete roughness elements. Additionally, the crossflow stability has been investigated on swept surfaces for high-speed flows as well, typically using elliptic cones[79, 80, 81, 82]. However, for this work the third type will be used, specifically a cone at angle of attack following extensive previous work[83, 84, 28, 85, 32, 86, 5, 87, 88, 89, 90, 7, 91, 92, 93], which will be discussed in more detail. Lastly, it has been observed that the crossflow instability has an additional complexity over the more studied streamwise instabilities in that the disturbances can either be traveling or stationary[94, 95].

In this chapter, the stability characteristics of a hypersonic three-dimensional boundary layer are investigated for flow over a sharp cone at angle of attack. As has been discussed, Mack's second mode disturbance can often dominate in purely two-dimensional/axisymmetric hypersonic flows. However, for a cone at angle of attack, first mode, second mode, and crossflow instabilities all become relevant mechanisms in the transition process[96, 83, 97]. The crossflow instability arises due to the fact that windward shock is stronger than the leeward shock, which produces a circumferential pressure gradient. This pressure gradient pushes fluid from the windward side to the leeward side, inducing a velocity component within the boundary layer that is perpendicular to the edge streamlines, called crossflow. Since the velocity must drop to zero at the surface and since by definition the crossflow component is zero at the edge, implies that there is a maximum crossflow value within the boundary in addition to an inflection point. This can more easily be seen by examining Figure 5.1.

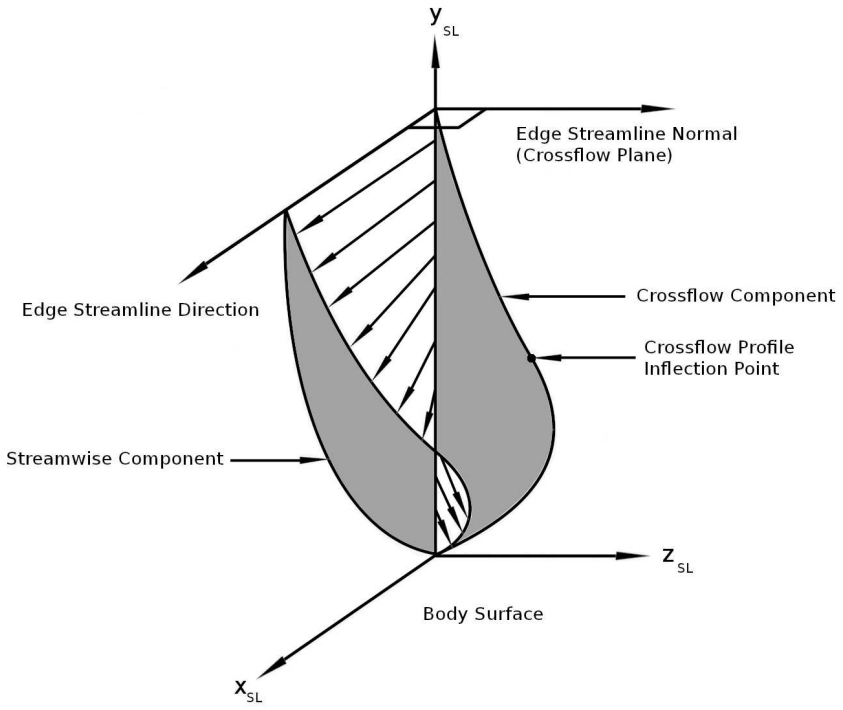

Figure 5.1: Three-dimensional boundary layer profile showing streamwise and crossflow components. Adapted from Figure 2 of Adams & Martindale[4]

Two direct numerical simulations (DNS) of a cone at angle of attack provided the high quality boundary layer transition data presented in this paper. The solutions were generated using a low-dissipation flux scheme in the three-dimensional unstructured Navier-Stokes solver, US3D[17], which was developed at the University of Minnesota. In order to observe the transition process in a DNS, a perturbation of the flow is often required. Common methods used to accomplish this include introducing freestream disturbances, adding small fluctuations of suction and blowing through the surface such that there is zero net mass flux, or adding surface roughness elements to the model. It has been widely observed that freestream acoustic disturbances have considerable influence on first and second mode instabilities. However, for the crossflow instability, surface roughness appears to hold greater influence while freestream disturbances affect whether the primary crossflow instability is either stationary or traveling.[96, 98, 5] The specific influence of surface roughness on the crossflow instability is still largely unknown for high-speed flows. Therefore, in order to study the interaction of surface roughness with the crossflow instability, a digitally filtered, randomly distributed surface roughness was introduced into the simulation.

5.2 Experimental Setup

The Boeing/AFOSR Mach-6 Quiet Tunnel (BAM6QT) facility located at Purdue University is a Ludweig tube type tunnel capable of quiet flow operation up to a stagnation pressure of 1 MPa (150 psia) and is considered the largest operational hypersonic quiet tunnel in the world. Under conventional operation, the tunnel is capable of operating at a stagnation pressure of 2 MPa (300 psia). The facility consists of a long driver tube, nozzle, test section, diffuser, burst diaphragms, and a vacuum tank. A schematic of the facility is shown in Figure 5.2 and a list of relevant specifications can be found in Table 5.1. Operationally, the portion of the tunnel upstream of the burst diaphragm is pressurized to the desired stagnation pressure while the vacuum chamber is evacuated. To start the flow, the diaphragms are burst resulting in a shock wave traveling downstream to the vacuum tank while simultaneously an expansion wave travels upstream. During the test run, the expansion wave reflects between the most upstream end of the driver tube and the contraction. Most notably, under quiet flow operation the tunnel boundary layer is removed by bleed slots at the contraction resulting in noise levels of 0.05% and less[99]. The reader is referred to Schneider[12] for more details regarding the BAM6QT facility.

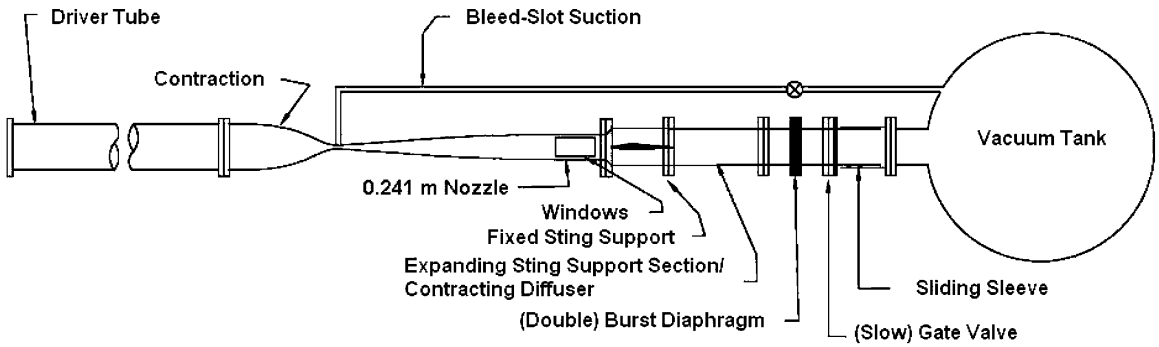

Figure 5.2: Boeing/AFOSR Mach-6 quiet tunnel schematic.

Driver Tube	Length:	37.34 m
	Bore:	0.445 m
Nozzle	Length:	2.590 m
	Exit Diameter:	0.242 m
Stagnation Temperature		433 K
Maximum Stagnation Pressure	Quiet:	1 MPa
	Conventional:	2 MPa
Noise Level	Quiet:	$\leq$0.05%
	Conventional:	$\sim$3%
Test Time		3-4 s (quiet operation)

Table 5.1: Boeing/AFOSR Mach-6 tunnel specifications.

The primary basis for the work presented in this chapter are the recent series of cone at angle of attack experiments performed at the Purdue Boeing/AFOSR Mach 6 quiet tunnel. The experimental model was nominally a 7.0° half angle cone with a 51 μm (0.002 in) nose radius and a total length of 41.37 cm (16.29 in). The model was mounted in the wind tunnel at a 6.0° angle of attack to the flow. Several different configurations have been used throughout the ongoing cone at angle of attack experiments. Initial runs began sometime in the early 2000's[6] and the first cone model was constructed using a two-piece construction. The sharp nose tips (51 μm nose radius) were machined using 6061-T6 aluminum and had a total length of 15.70 cm. It should be noted that additional nosetips of various nose radii were constructed and used in this first campaign of angle of attack experiments, but are not considered for this work. Two types of frusta were used. The first type was machined out of 6061-T6 aluminum which was used in both temperature sensitive paint (TSP) and oil flow visualizations. A second type was machined using a Nylon 6,6 material. The material for the second type was chosen for it's superior insulative properties for use in surface temperature and heat flux measurements from TSP. Both types of frusta had a total length of 25.67 m. Therefore there were two configurations, one with an aluminum nosetip and an aluminum frustum and the other with an aluminum nosetip and a nylon frustum. A photograph of this cone setup is shown in Figure 5.3. For convenience, this first cone will be referred to as Cone A.

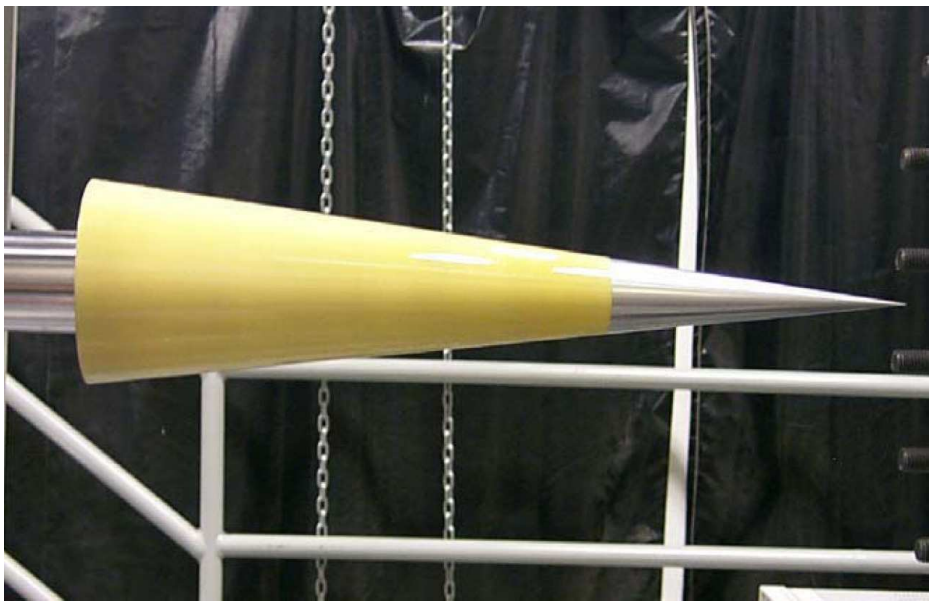

Figure 5.3: Photograph of the original Purdue 7° half angle cone[5].

Also of note from this first campaign of experiments, was the investigation of the effect of surface roughness on the nosetip. Five discrete surface roughness elements were placed azimuthally at the axial location x=5.08 cm. This axial location is within the range of the first neutral point for the most unstable crossflow disturbances as calculated by Li *et al.*[88] The first element was located on the 37° ray, azimuthally (where 0° is defined as the windward ray). The following elements were separated by 9° spacing azimuthally which corresponds to a wavenumber of 40, which is in the range of predicted unstable crossflow disturbances. The roughness elements were built up by stacking five rub-on dots on top of each other at each location and are shown in Figure 5.4.

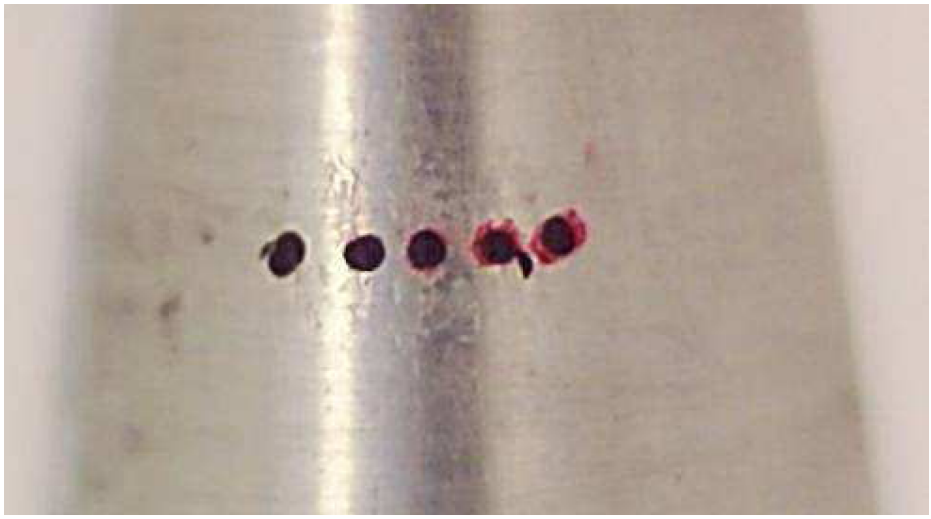

Figure 5.4: Discrete roughness elements (rub-on dots) at the axial location x=5.08 cm.[6]

Later, it was discovered that the cone model described above had a measurable forward-facing step in the junction between the nosetip and frustum[86]. It was determined that this was a consequence of the painting procedure, where only paint was applied to the frustum and not the nosetip. Subsequently, a second cone model was constructed in a similar fashion to the first cone, however the frustum radius was reduced by 200 μm in order to account for the thickness of the paint. This second cone model was constructed with slightly different dimensions and materials. The nosetip length was shortened slightly, to 15.24 cm, and the frustum to 25.40 cm resulting in a total length of 40.64 cm[7]. Two stainless steel nosetips with the same nose radius as before, were fabricated. One which was polished and the other kept the unpolished, machine finish. This was done in order to study the effect of distributed roughness and will be discussed further below. A photograph of the second cone model is shown in Figure 5.5. In following discussion, this cone will be referred to as Cone B.

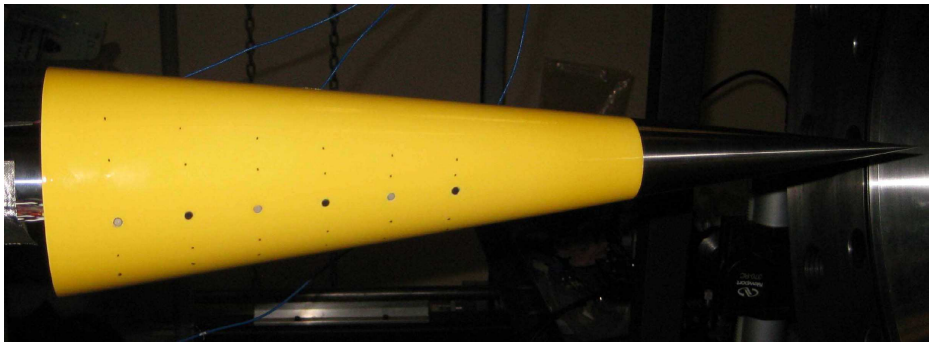

Figure 5.5: Photograph of the new Purdue7° half angle cone.[7]

There is much to learn regarding the role that surface roughness plays in the crossflow instability. Throughout the cone at angle of attack investigations at Purdue, there have been efforts to study surface roughness effects. The preliminary roughness experiments focused on discrete surface roughness elements while subsequent investigations have considered distributed roughness on both the frustum and nosetip. For the frustum, two surface types were achieved through the use of different base coats and painting techniques. One method used a careful process of application of paint to achieve a smooth finish. A second method applied a different type of base coat to achieve an orange peel finish[1]. Sample images of both smooth and rough paint finishes are shown in Figure 5.6. Surface characteristics of all types of surface finishes were quantified using a Mitutoyo Surftest SJ-301 profilometer and a summary of nominal roughness heights[6, 86, 90, 7, 100] for both cones is provided in Tables 5.2a and 5.2b. An important note concerning the step located at the nosetip-frustum junction. From the most recently published cases (Table 5.2b, last row), it was noted[7] that despite greatly reducing the magnitude of the forward-facing step there were azimuthal variations along the junction. It was proposed that these variations between forward-facing and backward-facing steps held greater influence than the difference in surface characteristics between the machined and polished nosetips. There are current efforts to further mitigate discontinuities from the nosetip-frustum junction using a new painting technique, referred to as feathering[100].

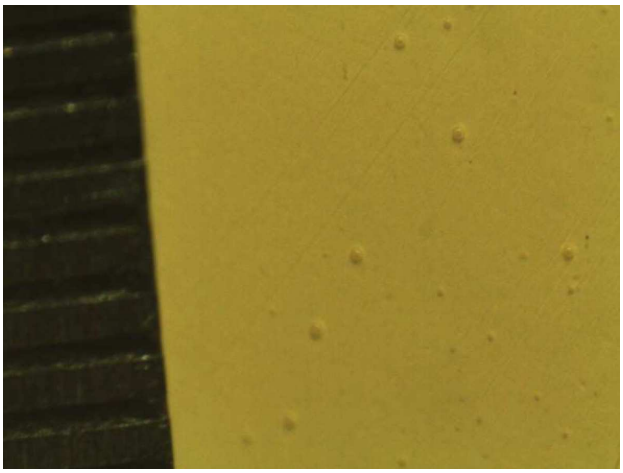

(a) Sample smooth paint finish.

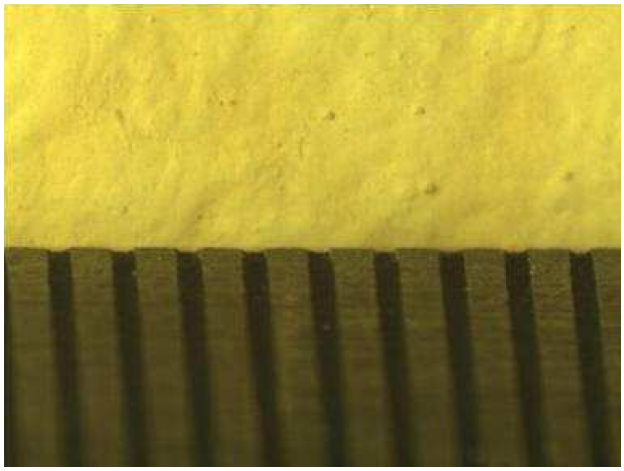

(b) Sample rough "orange peel" paint finish.

Figure 5.6: Microscopic images of paint finishes. Ruler graduations are 1/64 inches apart.[1]

Component	Surface Type	Roughness Magnitude (μm)	Step (μm)
Nosetip	Machined	0.3 [RMS]	–
	Discrete Elements	12 to 18	–
Frustum	Smooth Paint	0.2 to 0.3 [RMS]	80 to 85
	Rough Paint	3 to 10 [RMS]	70 to 160

(a) Cone A nominal roughness characteristics.

Component	Surface Type	Roughness Magnitude (μm)	Step (μm)
Nosetip	Machined	0.3 [RMS]	–
	Polished	0.01 [RMS]	–
Frustum	Smooth Paint 1	0.4 [RMS]	40 to 80
	Smooth Paint 2	0.4 [RMS]	-5 to 5

(b) Cone B nominal roughness characteristics.

Table 5.2: Summary of roughness magnitudes for various surfaces[1].

Two methods were used in the experiments to aid in the visualization of the primary flow features. One was the oil flow visualization technique where the cone model was spray painted black and a silicone oil with either a white or fluorescent pigment was brushed onto the surface of

the model. Any stationary crossflow vortices present in the flow would be seen as a series of peaks (lighter) and valleys (darker). The second method used was temperature sensitive paint (TSP). In addition to providing qualitative observations of flow features, such as the surface temperature effects of crossflow vortices, a methodology was implemented to use the TSP for providing more quantitative results such as surface temperature and heat flux. See Swanson and Schneider[5] and Swanson[6] for details about the TSP measurement techniques.

The series of experiments completed to date have examined various cone surface roughness types, tunnel operation modes (quiet vs. noisy), and freestream unit Reynolds numbers[5, 6, 86, 90, 7, 93]. The freestream unit Reynolds number has ranged from 8.1×10^6/m to 14.4×10^6/m corresponding to a range of stagnation pressures from 610 kPa to 1200 kPa. However, a representative case was chosen for the work presented here which corresponds to conditions that are near the tunnels maximum operating conditions under quiet flow and where several interesting flow features were observed. These conditions correspond to an approximate stagnation pressure of 930 kPa (135 psia) and a freestream unit Reynolds number of 9.5×10^6/m.

5.3 Numerical Setup

5.3.1 Flow Solutions

As described in Chapter 3, the three-dimensional, unstructured, cell-centered finite volume flow solver, US3D[17] was used to simulate the flow over a cone at angle of attack in this study. For the DNS calculations, the inviscid fluxes were evaluated using the high-order low-dissipation scheme developed by Subbareddy and Candler[22]. To broadly summarize, this scheme decomposes the inviscid fluxes into a non-dissipative symmetric component and a dissipative component which is pre-multiplied by a shock detecting switch given by Ducros[24]. This flux evaluation has the following form:

$$F_{flux} = F_{sym} + \alpha_{sw} F_{diss}$$

The switch, α_{sw}, ensures that the dissipative portion of the flux evaluation is only used in regions near discontinuities while in smooth regions only the non-dissipative portion is used. A sixth-order reconstruction of the inviscid fluxes and second-order point implicit time integration was used for the DNS results presented in this paper. As an aid to the analysis of the DNS computations, a

steady mean flow solution was also generated. For this solution, a second-order-accurate modified Steger-Warming (MSW)[21] flux vector splitting scheme was used to compute the inviscid fluxes and a first order implicit parallel Full-Matrix Point Relaxation method[19] of time integration. In both cases, the viscous fluxes were computed using a weighted least-squares gradient approximation scheme.

For all of the simulations, a representative set of freestream conditions were used, as previously mentioned. These conditions are shown in Table 5.3 and include an isothermal wall temperature condition of 300 K. Due to the range of operational conditions that the BAM6QT operates at, the test gas, which is air, is considered nonreacting. Therefore, in the simulations a perfect gas air assumption was used. The 6.0° angle of attack was achieved by inclining the freestream velocity vector.

M	$R_\infty[1/m]$	T_0 $[K]$	$P_0[MPa]$	$\rho_\infty\left[kg/m^3\right]$	$T_\infty[K]$	$u_\infty[m/s]$	$T_{wall}[K]$
6.00	9.50×10^6	433	0.927	0.0387	52.85	874.5	300

Table 5.3: Simulation freestream conditions.

Again, the steady mean flow solution was generated using standard modified Steger-Warming fluxes and first order implicit time integration. This methodology permits the use of large time steps, though with limitations, to converge the calculation to steady state using fewer iterations. For the unsteady calculations, however, high-order low-dissipation numerics were required. Additional restrictions placed on maximum allowable time step due to the sharp nose grid resolution requirements significantly increase computational demands. Therefore a balanced approach to computational resources and accuracy in the nose region results in a time step of 2.5×10^{-9} seconds which corresponds to a CFL of 20 in a small region at the nose and less than one everywhere else. This ensures that the numerical dissipation due to the time integration is negligible in all of the regions of interest.

5.3.2 Grid Construction

To reproduce the experiments, the computational model consisted of a 7.0° half angle sharp cone with a 51 μm (0.002 in) blunted nose and a total axial length of 413.7 mm. For the present work, one half of the full cone was modeled, and a symmetry condition was utilized. The symmetry plane was defined such that the cone was split in the plane of the pitch angle along the windward

ray, defined as 0°, and the leeward ray, defined as 180°.

By carefully constructing a grid of very high quality, the sources of grid-related errors in the computed solution can be minimized. This is especially important considering the small amplitudes of some of the quantities that are of interest to this investigation. As such, the three-dimensional unstructured grid, consisting entirely of hexahedral cells, was generated using the commercially available software package GridPro. The grid was constructed by first generating a solution on a coarse grid where the outer domain was conservatively placed such that it would capture the shock shape. The shock position was extracted from the initial solution and imported into Pro/ENGINEER, where the desired outer domain surface was constructed by closely following the shock shape with minimal buffer zone. This ensured the efficient use of grid points within the domain by minimizing the number of points in the freestream and helped to accurately capture the shock in the refined grid. Using the outer domain surface and the cone model surface, the grid topology was created with careful attention to the cone surface grid densities. It should be noted that using this topological paradigm one can avoid creating a grid singularity in the nose region as would be encountered in structured grid generated by revolution. This singularity, due to its location near the stagnation region, can be troublesome for finite volume solvers.

The grid described above is shown in Figure 5.7a and utilizes a nested refinement technique, shown in Figure 5.7b, in the streamwise direction. While nested refinement does introduce five-cell singularities, the effect of these points on the flow are minimized by strategically placing them away from the regions of interest, in this case near the leeward plane. The primary benefit of this refinement technique is that it provides the user the ability to tailor the shape and spacing of the cells where desired, which for this investigation is in the windward region where surface roughness is to be applied and in the region split by the 90° ray, sometimes referred to as yaw-side, where observations of the crossflow phenomena are expected. By carefully constructing the grid topology in this manner, one is able to ensure that the finite volume cells are smooth and regular with a minimum of skewness. Based on experience generating grids for similar flows, grid clustering normal to the surface and a required value of y^+ less than one at the first solution point away from the wall ensures that the boundary layer is appropriately resolved in the body-normal direction.

An additional requirement was adequate spatial resolution of observed crossflow disturbances, typically desired to be a minimum of ten to twenty grid points per wavelength. After meeting all these requirements, the resulting high-quality grid consisted of 140 million cells with 200 points

normal to the surface.

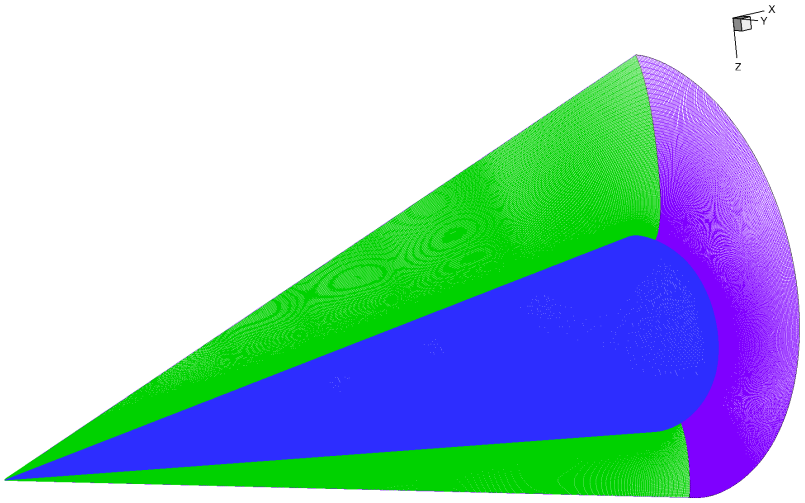

(a) Computational grid.

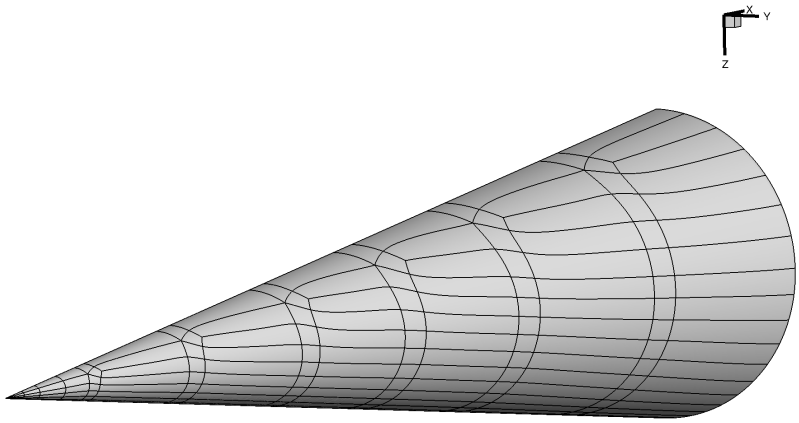

(b) Surface grid topology.

Figure 5.7: Simulation geometry.

5.3.3 Surface Roughness Model

A digitally-filtered, randomly-distributed surface roughness model was used in the DNS calculations. The approach used to generate this surface roughness was adapted from a digital filtering technique applied in the prescription of perturbations as an inflow condition in shock-boundary layer interaction studies[101]. The primary benefit of this approach is the ability to specify a desired length scale for the roughness. This allows one to target and effectively perturb certain boundary layer instabilities, in this case stationary crossflow disturbances, while providing a roughness pattern that reasonably reflects observed surface imperfections in real experimental models.

A description of the derivation of this digital filter can be found in Appendix B. For more details on this approach see Touber[102]. In summary, a set of filter coefficients are constructed such that the application of the filter operator attempts to enforce a particular shape on the correlation function based on some selected form. In this case, it is desired that the correlation function (left hand side) fit an exponential function (right hand side) defined by an integral length scale which is given by

$$R_c\left(x_k + r_{lag}\right) = \exp\left(-\frac{\pi r_{lag}}{2I_r}\right)$$

where R_c is the correlation function, x_k is the particular grid location, r_{lag} is some distance from x_k, and I_r is the specified length scale. The process for creating the digitally-filtered roughness basically consisted of the following steps. First, a desired integral length scale, I_r, was selected for use in the filter operator. Next a maximum radius, which defines the filtering neighborhood, was selected to be $r_{max} = 3I_r$. Then a set of random roughness heights of uniform distribution were created for the surface using a generic pseudo-random number generator. It was desired to have a set of normally distributed random heights with unit variance. Therefore, the range of the original random heights was modified to fit in (0,1] and the Box-Muller transform was performed on the set. Lastly, the filter operator was applied to the roughness heights using the appropriate filter coefficients. A sample flat plate case with unfiltered and filtered surface roughness is shown in Figures 5.8b and 5.8c, respectively. Also plotted is a correlation function comparison between the theoretical exponential function and the filtered values which is shown in Figure 5.8a. The length scale and roughness height selected for this sample is identical to that used in the cone calculations which are $I_r = 0.5$ mm and $h = 10\,\mu$m RMS. The scale of the plots below are roughly

the same as those shown in Figure 5.6. Qualitatively, there is decent resemblance between the orange peel paint finish shown in Figure 5.6b and the digitally-filtered surface roughness shown in Figure 5.8c.

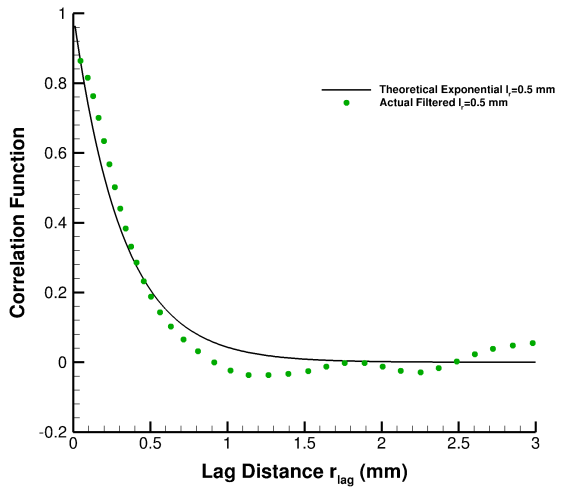

(a) Correlation function comparison: theoretical vs. actual.

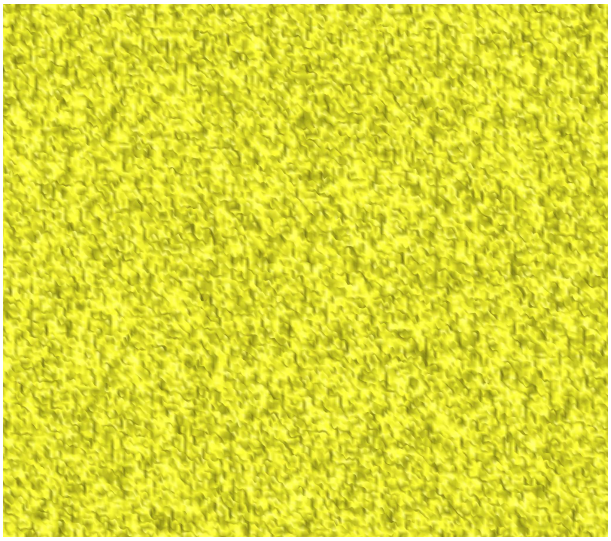

(b) Pre-filtered surface roughness.

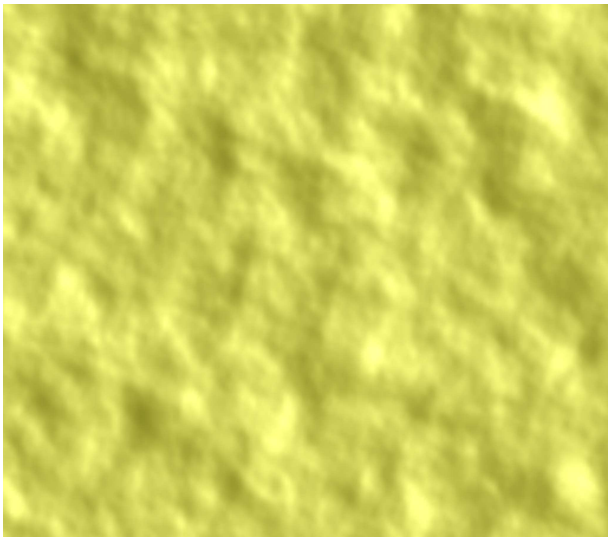

(c) Digitally-filtered surface roughness. Specified length scale $I_r = 0.5$ mm and roughness height 10 μm RMS.

Figure 5.8: Example using the digitally filter method for generating surface roughness on a flat plate. Figures (a) and (b) are plotted using similar scales to those shown in Figure 5.6.

For the work presented in this chapter, the region of roughness was limited to a strip centered

along the 20° ray beginning at an axial location of 5.1 cm (1000 nose radii) and ending at the axial location 200 cm. The circumferential width of the region of roughness remained a constant $\triangle 15°$ width along the length of the strip. Figures 5.9a and 5.9b show the roughness strip for this case. Since the magnitudes of the roughness heights are on the order of micrometers, the surface displacement has been enhanced in these plots by shading in order to aid in visualization. The integral length scale was chosen to reflect a wavelength of approximately 0.5 mm corresponding to the azimuthal wavenumber of 80 at the 5.1 cm axial location. Two roughness heights were considered for this work and were set such that the root-mean-square (RMS) value was 10 μm and 20 μm, both of which have been achieved experimentally through painting techniques[1] and sand-blasting[100] on similar models. It was the intent of this work to build on Balakumar's previous DNS computations[89] of this configuration to include more complex surface roughness models.

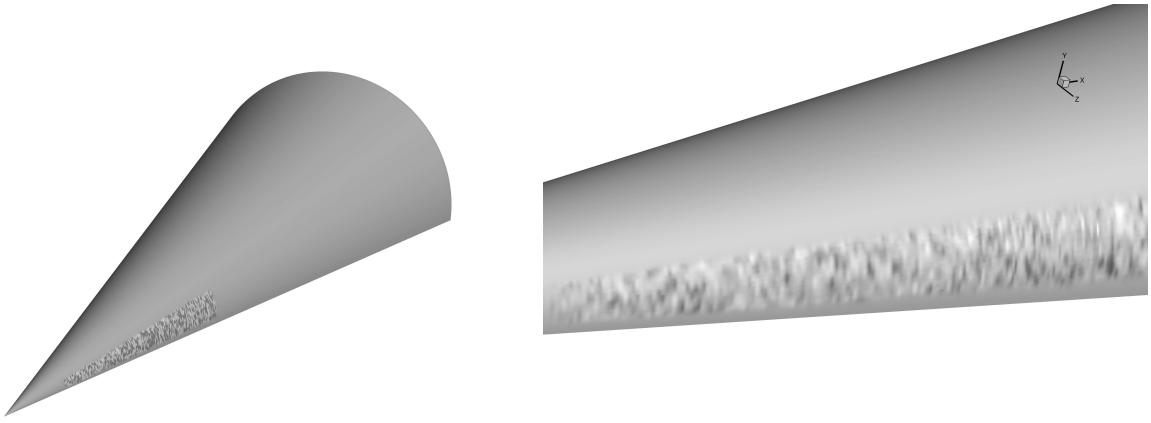

(a) Surface roughness strip location.

(b) Surface roughness zoom.

Figure 5.9: Surface roughness element locations.

5.4 Results

A steady mean flow solution was first generated and will be used to show basic flow features as well as to provide a basis for elucidating certain features of the crossflow instability. A useful visualization technique for overview of the fundamental flow features for a cone at angle of attack are density contours. Figure 5.10a shows such contours for the cone surface, at four axial locations

and along the symmetry planes. Examining this plot, it can be seen that the greater strength of the shock near the windward plane (0° ray) compared to the leeward plane (180° ray) results in the development of a circumferential pressure gradient and subsequently the crossflow velocity component within the boundary layer. This phenomena can be more easily recognized by looking at Figure 5.10b. In this figure, the red lines correspond to streamlines based on the velocity vector at the detected boundary layer edge and are therefore representative of the inviscid flow path of the fluid. While this flow is still subject to the transverse pressure gradient, at the boundary layer edge the fluid still has enough momentum to prevent the streamlines from the more substantial deviation observed in the fluid flow nearer to the wall. This particular aspect can be seen by examining the black lines in Figure 5.10b. These streamlines are generated using the velocity vector in the first cell away from the wall, which will be referred to as the shear velocity. By comparing to the inviscid streamlines in red, it can be seen that the lower-momentum fluid in the boundary layer is much more responsive to the transverse pressure gradient. It is this component of the velocity that is parallel to the wall and perpendicular to the inviscid (edge) velocity which is defined as the crossflow, and its magnitude reaches a maximum value within the boundary layer.

Returning again to Figure 5.10a, as expected the boundary layer becomes substantially thicker along the leeward symmetry plane. This is due to the accumulation of low momentum fluid which has been convected by the crossflow component on either side of the leeward ray resulting in the mushroom-shaped lifted boundary layer. The profiles along this plane are highly inflected and are thus subject to multiple instabilities. In contrast, the fluid near the windward symmetry plane is pushed away resulting in boundary layer thinning.

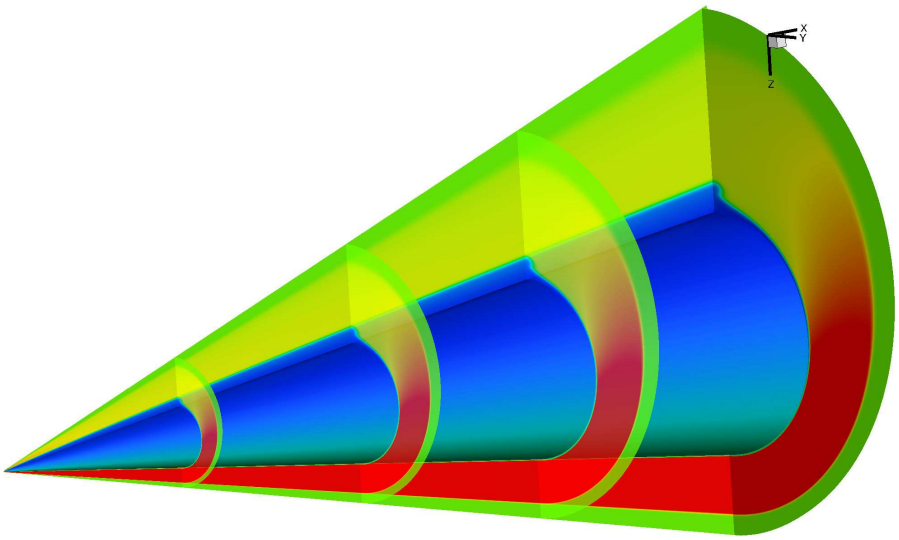

(a) Density contours

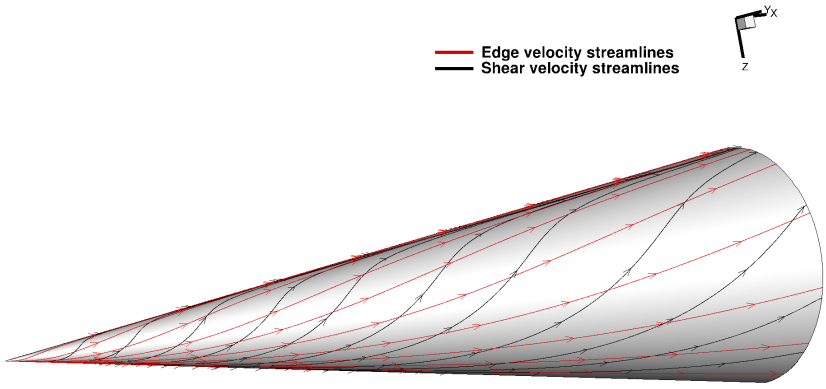

(b) Edge and shear velocity streamline

Figure 5.10: Laminar steady mean flow solution of cone at 6.0° angle of attack

The acceleration and deceleration of the crossflow velocity component can be seen in Figure 5.11 which shows contours of maximum crossflow velocity normalized by local edge velocity.

As fluid moves from the windward to the leeward plane, increasing crossflow velocity in Figure 5.11 is associated with increasing divergence between the inviscid and the shear streamlines in Figure 5.10. The peak crossflow velocity reaches a maximum value of approximately twelve percent of the edge velocity as the two sets of streamlines begin to converge again. The inflected boundary layer profiles due to the crossflow are unstable and can lead to the formation and amplification of crossflow vortices. However, the MSW fluxes used in the calculation of the steady mean flow are too dissipative to permit the generation of any such structures.

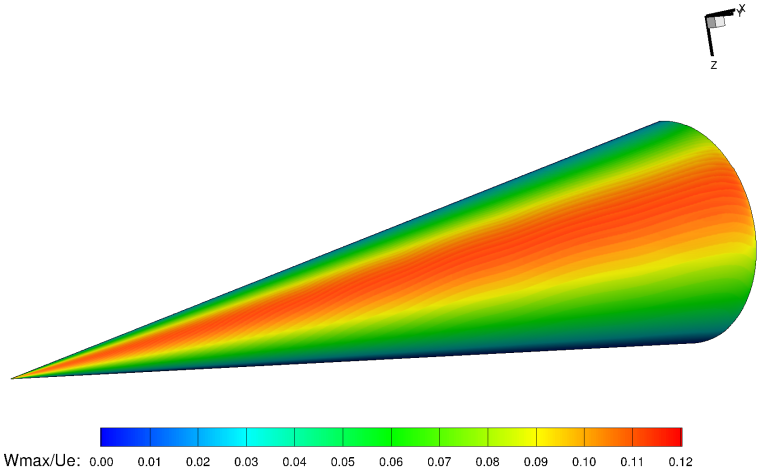

Figure 5.11: Maximum crossflow velocity contours normalized by local edge velocity

Qualitative comparisons between experimental and computational observations can provide useful insight where identifiable similarities exist and meaningful questions where differences arise. To aid in the analysis of the crossflow phenomena observed in the DNS, results from recent experimental work at Purdue[6, 5, 90, 7, 1, 93] will be used as a basis for qualitative comparison. The qualitative nature of these comparisons must be stressed due to readily evident differences between the computations presented here and the experimental results published to date, such as a measurable forward facing step[86], azimuthal variations in the nosetip-frustum junction[7], and slight differences in the freestream unit Reynolds numbers. Additionally, the machining and painting processes in the fabrication of the model can result in surface roughness characteristics that are significantly different than that used in this work. Also, the use of symmetry planes in the simulations by definition prescribes the fluid flow to be symmetric where symmetry may not

physically exist. This may be especially relevant along the leeward plane where the fluid from either side of the plane is flowing toward the plane and may in reality oscillate from one side to the other.

As previously discussed, two flow visualization methods were used during the experiments, oil flow and temperature sensitive paint. Figure 5.12a shows an image from a run early on in the cone at angle of attack experiments using oil flow visualization. In the picture light and dark streaks can be clearly seen on the surface indicating that stationary crossflow vortices were present. This would be a somewhat surprising observation, considering that the tunnel was being operated in a conventional mode. However, it has been proposed[6] that the vortices may be capable of maintaining their basic structure some distance into a turbulent boundary layer and that the flow of the oil is not greatly influenced by the smaller turbulent eddies. The next plot, Figure 5.12b, shows contours of what will be referred to as surface shear stress variation at a particular instance in time for the case with 20 μm roughness height. To emphasize the flow features from the direct numerical simulations, differencing with the baseline MSW-computed steady flow solution was used. In this case, the mean shear stress was subtracted from the DNS resulting in the plot shown. In a similar fashion, surface heat flux variation was calculated and will be used for subsequent comparisons. Comparing Figures 5.12a and 5.12b, it can be seen that the angles of the streaks in the computation appear to match the streaks visualized in the oil flow.

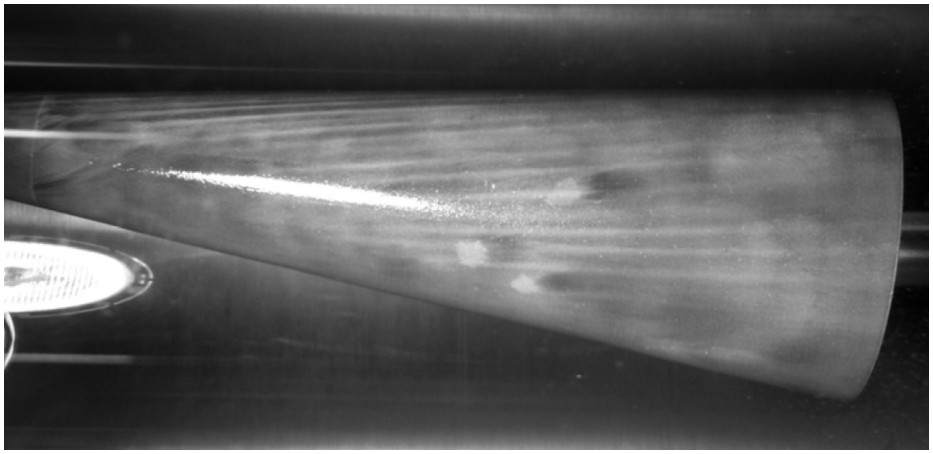

(a) Oil flow visualization[5]. Conventional operation.

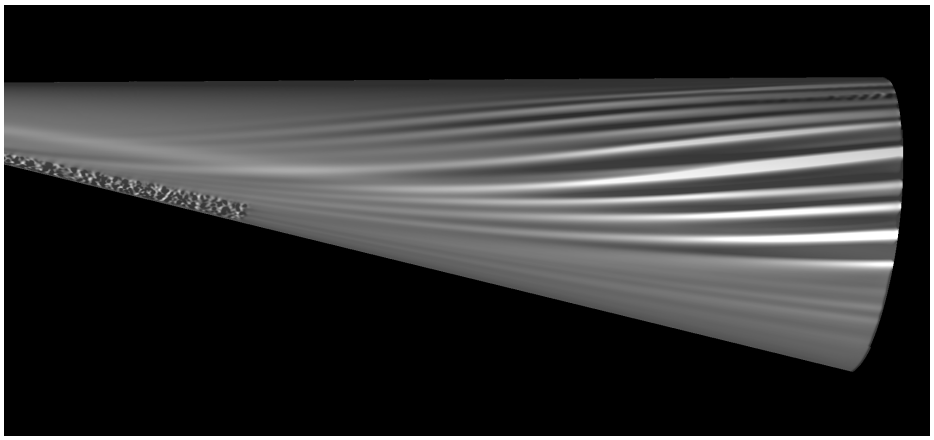

(b) Surface shear stress variation from DNS with surface roughness.

Figure 5.12: Comparison of crossflow vortical structures between oil flow observations and computations.

In Figures 5.13a and 5.13b a comparison of the streaks visualized using shear stress variation and surface heat flux variation is made for the DNS case with surface roughness height of 20 μm. Immediately, it can be seen that both methods detect the effect from the existence of crossflow disturbances almost identically, which is in contrast to some of the author's previous work[91]. Also, it can be observed near the aft portion of the cone near the leeward ray, that there appears to be some sort of secondary structures developing which will be discussed later. Additionally, the paths of these streaks differ considerably from the streamlines computed near the wall (black lines Figure 5.10). In contrast, they seem to roughly follow paths similar to the streamlines computed using the edge conditions (red lines Figure 5.10).

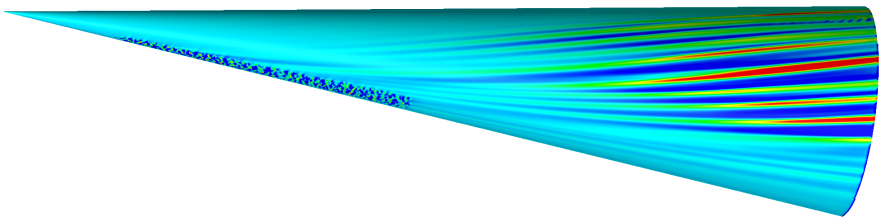

(a) Contours of surface shear stress variation.

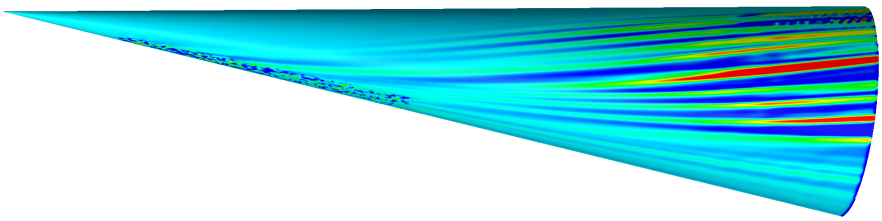

(b) Contours of surface heat flux variation.

Figure 5.13: Comparison of crossflow detection methods for the computations ($h = 20$ m). Both techniques capture the crossflow structures in a nearly identical fashion.

For the TSP visualization technique, a methodology was employed by which surface temperature or surface heat flux could be calculated. As such, certain sections of the cone were rolled flat for plotting purposes using a straightforward mathematical transformation procedure[6] and were used to present surface temperature and heat flux data. Of particular interest were the surface temperature plots which showed crossflow instability streaks. Unfortunately, a direct comparison of surface temperature would be useless since an isothermal wall temperature (300 K) boundary condition was used for the calculations of this work. However, using the previously described differencing technique between the DNS and baseline laminar solution, meaningful comparisons can still be made between the computations and experimental observations. In this case, surface heat flux and surface shear stress will be the primary visualization variables for the simulations.

The experimental surface temperature plot is shown in Figure 5.14a. Contours of the heat flux variation and shear stress variation from the DNS were plotted using the same mathematical transformation and a similar color map and are shown in Figures 5.14b and 5.14c. Examining these plots, one can observe decent qualitative agreement between all three plots. As indicated in each plot, an approximation of the angle of inclination is made for the observed crossflow disturbance as it passes through the 90° ray. In the experiment, the crossflow disturbances cross this yaw-side plane at a 13° angle of incidence. For the DNS results, streaks in both the surface heat flux variation and surface shear stress variation cross this plane at an angle of 15°. Again, for comparison, in the author's previous work there was an observable difference in angle of inclination between the heat flux variation and shear stress variation. It was later determined that there was a coding error, related to the boundary conditions, in the particular implementation of US3D that had been used which resulted in introducing artificial disturbances at each restart. Additionally, the gradual nature of the discrete roughness elements that had been used coupled with surface grid resolution that was not quite sufficient resulted in producing the results shown in the previous work.

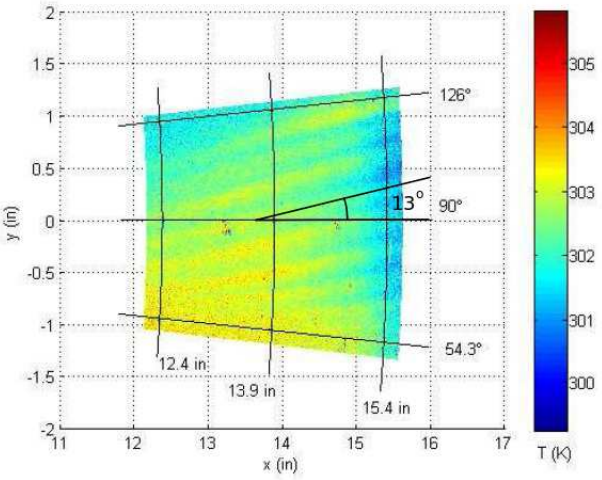

(a) Surface temperature data from TSP[5].

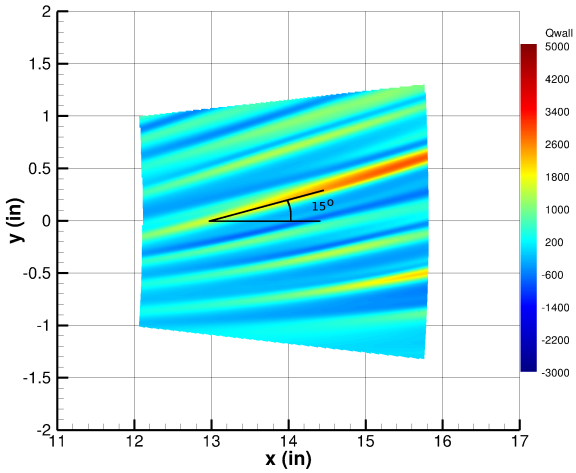

(b) Surface heat flux variation.

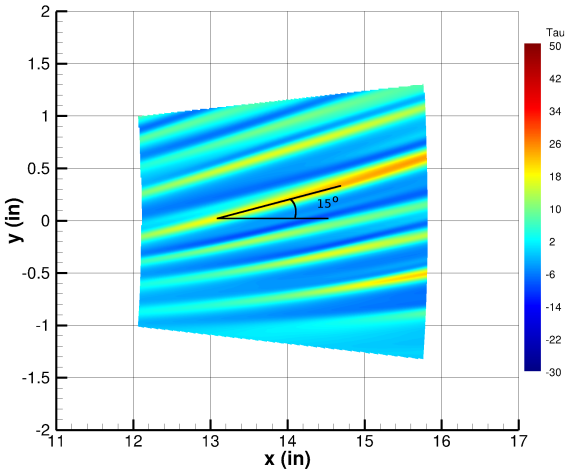

(c) Shear stress variation.

Figure 5.14: Comparison of crossflow vortical structures between TSP measurements and computations.

Quantifying the disturbance azimuthal wavenumbers from both the experiment and the simulations and making subsequent comparisons may also provide additional insight. Here, the azimuthal wavenumber is defined as the number of wavelengths of a particular disturbance at a particular axial location that can occupy one full circumference. The region in focus for determining the wavenumbers started a short distance upstream of and then through the range defined by the surface temperature plot window shown in Figure 5.14a, which was centered along the 90°

ray. In order to quantify the observed wavenumbers in the simulation with surface roughness, several axial slices of the flow were made between $x = 0.280$ m and $x = 0.390$ m. The heat flux was plotted as shown in Figure 5.15a, and the peaks of three disturbances were identified. The wavelength, in degrees, was determined by measuring the distance between the valleys on either side of each peak. Using these estimated wavelengths, each disturbance circumferential wavenumber was calculated. The three specified disturbances were tracked through the slices and the process for determining the wavenumbers was repeated for each slice. These results are presented in Figure 5.15b. What we see is that the wavenumbers range between 35 and 50, with most hovering around 40. This azimuthal wavenumber of 40 was observed experimentally as seen in Figure 5.14a, is in good agreement with previous stability calculations[88, 92] and fits reasonably well with previous direct numerical simulations[90]. It is interesting to note that the range of wavelengths associated with the roughness are noticeably smaller than the crossflow wavelengths measured in the results. It seems, therefore, that the system appears to have selected a preferred range of disturbance wavelengths.

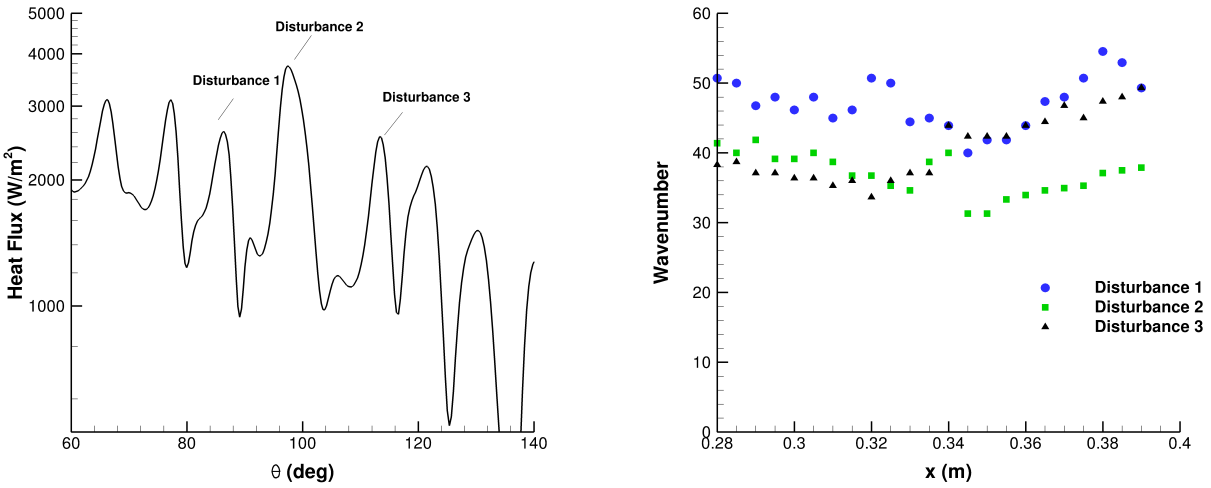

(a) Disturbance identification for the slice at axial location $x = 0.360$ m using surface heat flux. Cone with surfacewith roughness.

(b) Observed disturbance azimuthal wavenumbers for cone roughness.

Figure 5.15: Crossflow disturbance wavenumber observations.

In order to better visualize the crossflow disturbances, specifically if any vortical structures are present, the Q criterion can be used. The Q criterion, which is defined as $Q = \frac{1}{2}\left(|\Omega|^2 - |S|^2\right) > 0$

where S is the rate of strain tensor and Ω is the rate of rotation tensor, can represent coherent vortices as a spatial region. This is a convenient parameter to use as it can readily identify regions in the flow that are rotational, and in this case it can help identify any stationary co-rotating crossflow vortices. Figure 5.16 plots surface heat flux and the Q criterion for the 20 μm case. As one can observe, there are indeed crossflow vortices present which lie over the streaks in the surface heat flux. It can also be observed that toward the aft end of the cone near the leeward plane there appears to be a secondary instability acting upon the crossflow, possibly indicating transition is occurring.

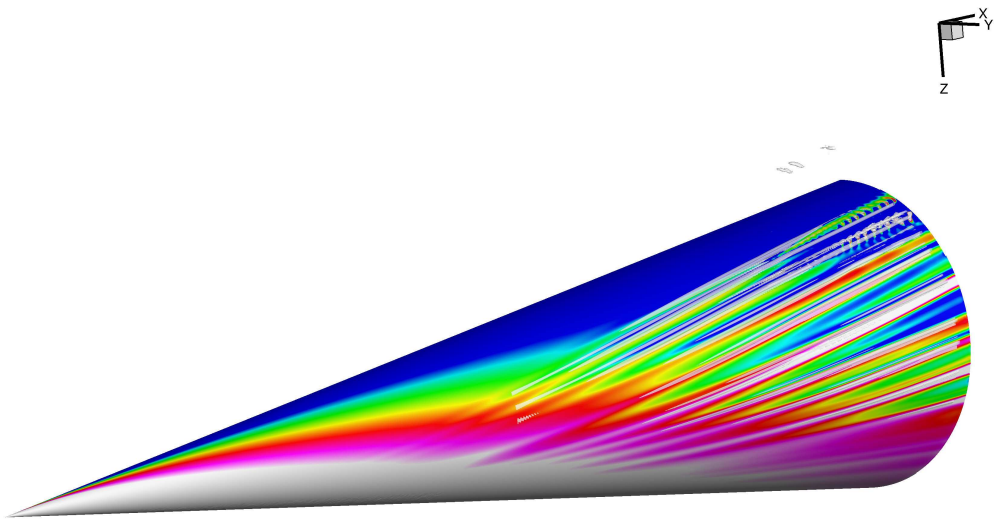

Figure 5.16: Surface contours of heat flux and isosurfaces of the Q criterion.

To get another perspective of the crossflow disturbances, slices of the flow showing contours of

temperature have been plotted in Figures 5.17, 5.18, 5.19, and 5.20 for axial locations $x = 0.25$ m, $x = 0.30$ m, $x = 0.35$ m, and $x = 0.40$ m, respectively. The flow is visualized by transforming the coordinate system from Cartesian coordinates into polar coordinates where Y represents normal distance from the surface of the cone. For comparison, plots from both roughness cases, 10 μm and 20 μm, are shown together. One can easily observe the lifted boundary layer near the leeward plane due to the accumulation of fluid. Even starting at the axial location $x = 0.25$ m, the disturbances are easily detectable and the difference between the two cases is readily evident. At $x = 0.30$ m and downstream, the disturbances become more developed and are easily identifiable as co-rotating vortices that one expects to see for the stationary crossflow disturbance.

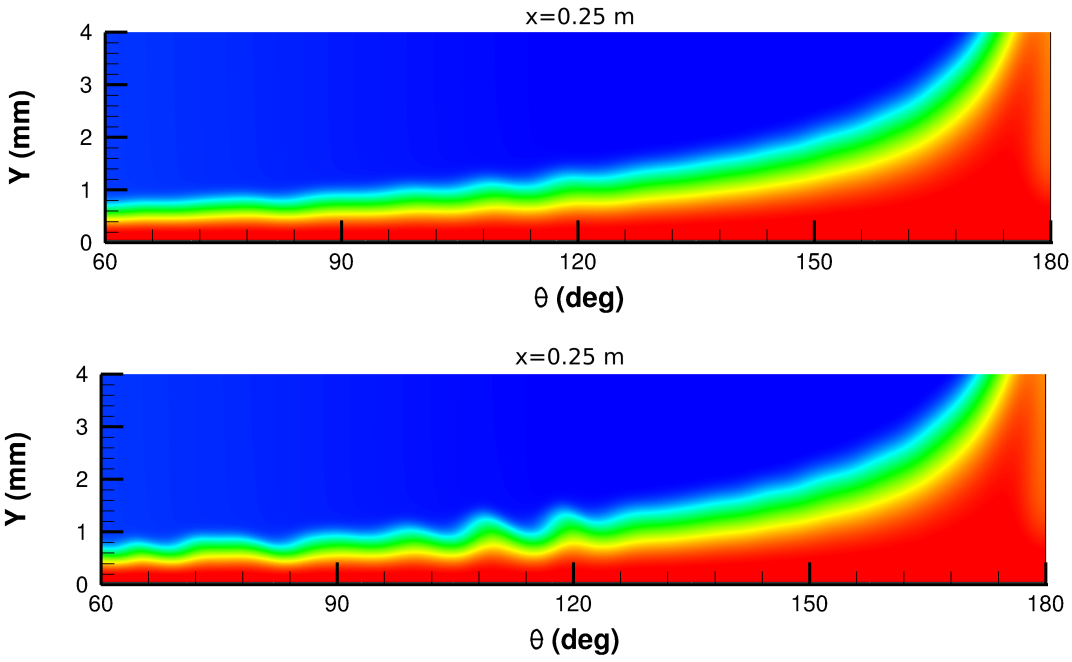

Figure 5.17: Temperature contour comparison at slice x=0.3 m. The 10 μm roughness height case top, 20 μm case bottom.

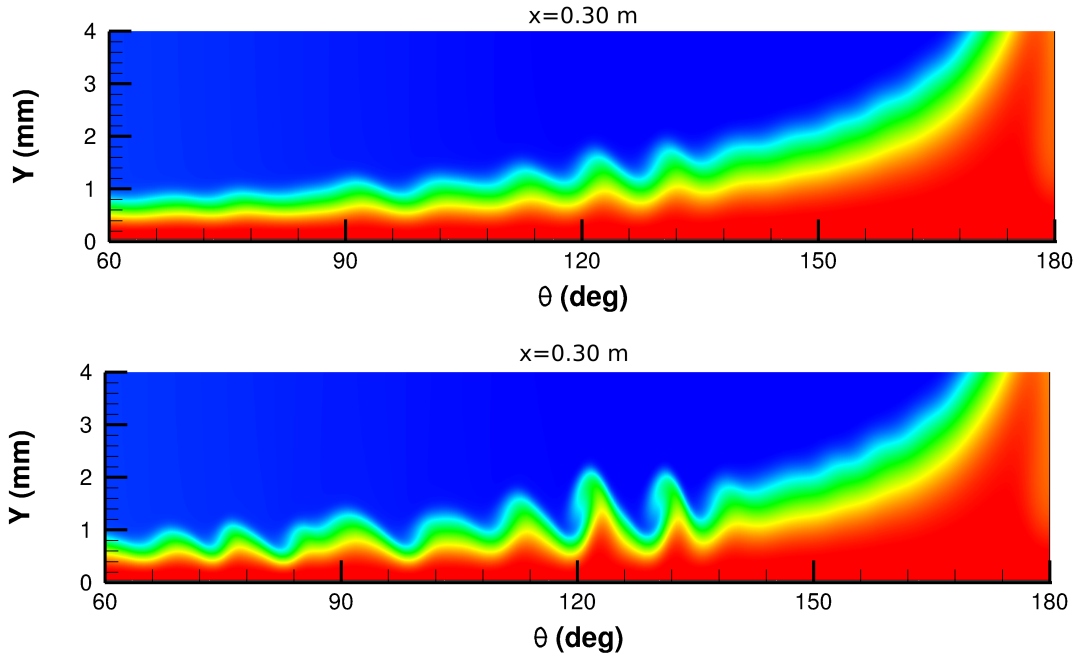

Figure 5.18: Temperature contour comparison at slice x=0.30 m. The 10 μm roughness height case top, 20 μm case bottom.

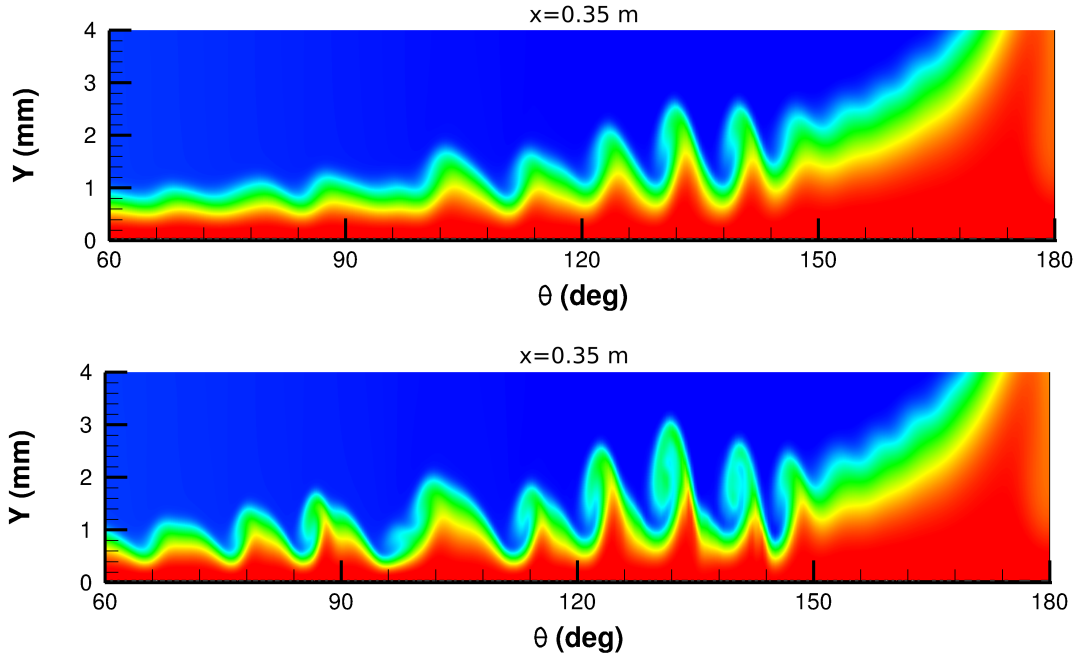

Figure 5.19: Temperature contour comparison at slice x=0.35 m. The 10 μm roughness height case top, 20 μm case bottom.

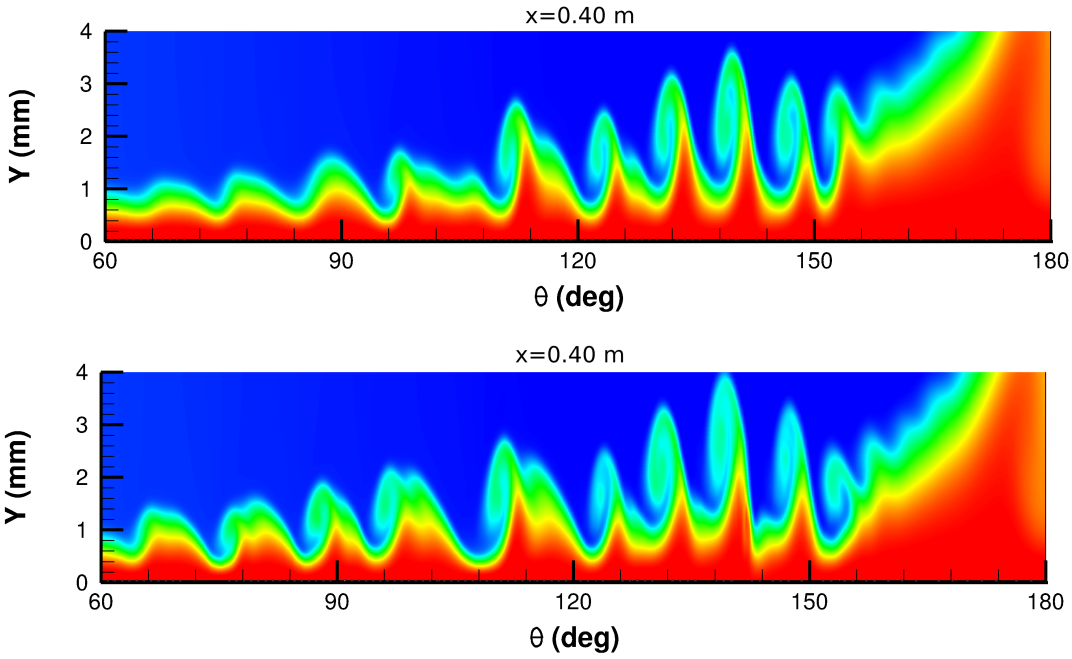

Figure 5.20: Temperature contour comparison at slice x=0.35 m. The 10 μm roughness height case top, 20 μm case bottom.

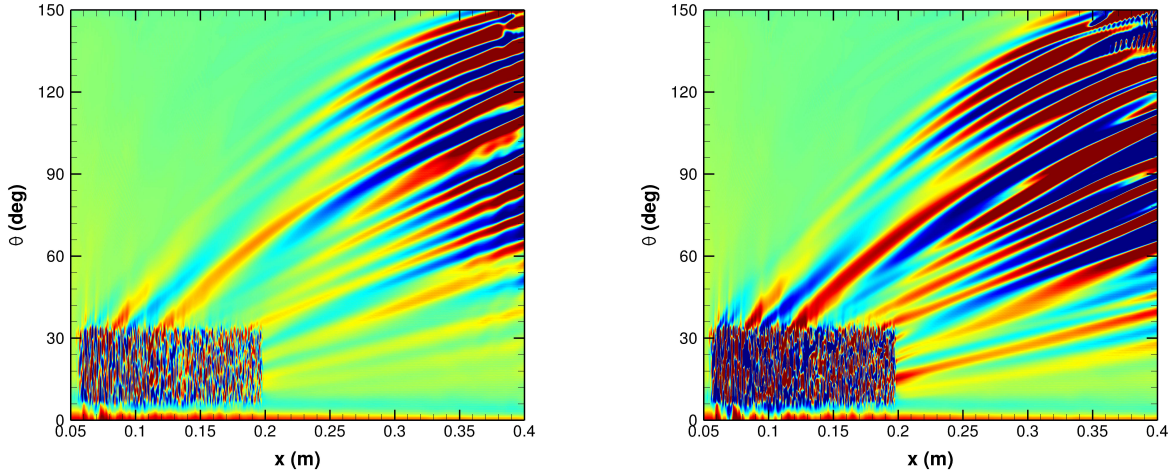

(a) Surface heat flux variation for the 10 μm roughness height case.

(b) Surface heat flux variation for the 20 μm roughness height case.

Figure 5.21: Comparison of the heat flux variation for the two roughness cases.

Lastly, contours of surface heat flux variation have been plotted on a two-dimensional coordinate system in Figures 5.21a and 5.21b. Here, θ represents the azimuthal angle such that 0° represents the windward symmetry plane and 180° represents the leeward symmetry plane. Note that in the figures, the patch of noise in the heat flux variation from 0.05 m to 0.2 m corresponds to the location of the roughness patch. Again, as seen in the temperature slices, there is a detectable difference between the roughness cases, where the streaks from the larger magnitude roughness are more intense. As previously noted, in the 20 μm roughness case there appears to be a secondary instability that is acting upon the crossflow vortices. During the simulation, this region remained quasi-steady in the sense that while the secondary instabilities are not stationary, they essentially continue developing at the same location. As it was not the intent of this work to study secondary instabilities, the grid is not adequately resolved to accurately capture them. Therefore, no definitive conclusions can be made.

Chapter 6

Conclusion and Discussion

The work presented herein focused on mechanisms involved in laminar-turbulent boundary layer transition. Specifically, two cases were considered. The first case focused on the characterization, amplification, and evolution of the streamwise disturbances observed in experiments conducted at the HIEST shock tunnel. The second case focused on the effect of surface roughness on the crossflow instability for a cone at angle of attack, where recent experiments at Purdue were used as a basis for the computations.

Turning first to the axisymmetric computations based on the transition experiments conducted at JAXA's HIEST facility. Using the linear PSE method as implemented in STABL, boundary layer stability analyses were conducted for four shots selected from the set of experiments. Calculations using the semi-empirical e^N method was compared to the experimentally measured transition locations. Previous work examining transition N factor values at other similar conventional wind tunnel facilities has found that a value of approximately $N = 5.5$ corresponds to transition. In contrast, the results here suggest that an N factor of 8.0 is the value which indicates the onset of transition for the HIEST facility. However, this result remains somewhat inconclusive, as only a limited number of cases were analyzed. In addition to providing transition data, boundary layer disturbance frequencies were also measured as a part of the HIEST experiments. These frequencies were compared to N factor versus frequency curves generated in the PSE-Chem analysis. The frequency range from the computational results compared reasonably well to those measured experimentally whenever the flow over a particular pressure transducer was laminar. However, as expected, when the flow over a pressure transducer was transitional or turbulent, the computational results show essentially no correlation to the measured frequencies

due to the broadening of the disturbance spectrum. Some additional theoretical operating conditions were examined for the HIEST facility in order to determine a reasonable operational range where chemistry has the greatest effect on transition. It was observed that there are two competing effects. Increasing freestream stagnation enthalpy destabilizes the boundary layer, while decreasing freestream unit Reynolds number results in the boundary layer becoming more stable. Further examination showed that there was a greater difference in boundary layer stability when comparing the inclusion versus exclusion of chemical kinetics modeling in the mean flow solutions over the same comparison in the PSE analyses. The inclusion of these effects in the mean flow generally increased the disturbance frequencies, the peak amplification rates, and the distance over which the disturbance frequencies were amplified. These observations were attributed, in part, to the decrease in boundary layer thickness, the increased proportion of the region of relative supersonic flow in the boundary layer, and to boundary layer characteristics that change more gradually over distance.

For the second portion, recent transition experiments conducted for a cone at angle of attack in hypersonic flow were investigated computationally. Although freestream disturbances are commonly employed for use in computational boundary layer transition studies, surface roughness was used for this work in order to investigate its effect on the stationary crossflow instability. Using a low-dissipation numerical scheme, two direct numerical simulations were computed and provided the data for analysis. These computations were performed for the cone at angle of attack and the results were compared with those of similar experiments conducted at Purdue. To model the surface roughness, a small strip of randomly distributed surface roughness was placed near the windward ray. Two roughness heights were considered, one with 10 μm RMS magnitudes and the other with 20 μm RMS magnitudes.

Both roughness heights provided sufficient destabilization to produce stationary crossflow vortices. Examining the computations and comparing to experimental results, several observations were made. It was shown that the crossflow structures visualized using both surface heat flux and surface shear stress matched well with the experimental observations. The disturbance azimuthal wavenumbers from the computation ranged from 35 to 50 with most hovering around 40, matching the wavenumbers from the experiments[5], recent stability calculations[88, 92], and similar DNS computations[89]. In both roughness height cases, the crossflow wavelengths were noticeably larger than the integral length scale from the roughness, preliminarly indicating that the system has a preference for certain wavelengths. Lastly, as expected, the larger magnitude

roughness destabilized the boundary layer to a greater extent with the development of crossflow vortices occurring further upstream than in the lower magnitude roughness case.

References

[1] C. Ward. Hypersonic Crossflow Instability and Transition on a Circular Cone at Angle of Attack. Master's thesis, Purdue University, December 2010.

[2] E. Reshotko. Transition Issues for Atmospheric Entry. *Journal of Spacecraft and Rockets*, 45(2):161–164, March-April 2008.

[3] M.V. Morkovin, E. Reshotko, and T. Herbert. Transition in Open Flow Systems: A Reassessment. *APS Bulletin*, 39(9):1–31, 1994.

[4] J.C. Adams and W.R. Martindale. Hypersonic Lifting Body Windward Surface Flow-Field Analysis for High Angles of Incidence. Technical Report TR-73-2, AEDC, June 1973.

[5] E.O. Swanson and S.P. Schneider. Boundary-Layer Transition on Cones at Angle of Attack in a Mach-6 Quiet Tunnel. Paper 2010-1062, AIAA, January 2010.

[6] E.O. Swanson. *Boundary-Layer Transition on Cones at Angle of Attack in a Mach-6 Quiet Tunnel*. PhD thesis, Purdue University, August 2008.

[7] A. Chou, B.M. Wheaton, C. Ward, P.L. Gilbert, L.E. Steen, and S.P. Schneider. Instability and Transition Research in a Mach-6 Quiet Tunnel. Paper 2011-0283, AIAA, January 2011.

[8] J.J. Bertin and R.M. Cummings. Fifty Years of Hypersonics: Where We've Been, Where We're Going. *Progress in Aerospace Sciences*, 39:511–536, August-October 2003.

[9] D.F. Fisher and N.S. Dougherty. In-Flight Transition Measurements on a 10 degree Cone at Mach NumbersFrom 0.5 to 2.0. Technical Paper TP-1971, NASA, January 1982.

[10] W.W. Haigh, B.H. Lake, and D.R. Ko. Analysis of Flight Data on Boundary Layer Transition at High Angles of Attack. Contractor Report CR-1913, NASA, January 1982.

[11] J. Laufer. Some Statistical Properties of the Pressure Field Radiated by a Turbulent Boundary Layer. *The Physics of Fluids*, 7:1191–1197, 1964.

[12] S.P. Schneider. Development of Hypersonice Quiet Tunnels. *Journal of Spacecraft and Rockets*, 45(4):641–664, 2008.

[13] A.J. Laderman. Review of Wind-Tunnel Freestream Pressure Fluctuations. *AIAA Journal*, 15(4):605–608, May 1977.

[14] T.J. Juliano and S.P. Schneider. Quiet-Flow Ludwieg Tube for Hypersonic Transition Research. *AIAA Journal*, 46(7):1757–1763, July 2008.

[15] M.V. Morkovin. Critical Evaluation of Transition from Laminar to Turbulent Shear Layers with Emphasis on Hypersonically Traveling Bodies. Technical Report TR-68-149, Air Force Flight Dynamics Laboratory, March 1969.

[16] H.B. Johnson and G.V. Candler. Hypersonic Boundary Layer Stability Analysis Using PSE-Chem. Paper 2005-5023, AIAA, June 2005.

[17] I. Nompelis, T.W. Drayna, and G.V. Candler. A Parallel Unstructured Implicit Solver for Hypersonic Reacting Flow Simulation. Paper 2005-4867, AIAA, June 2005.

[18] I. Nompelis. *Computational Study of Hypersonic Double-Cone Experiments for Code Validation*. PhD thesis, University of Minnesota, Minneapolis, Minnesota, May 2004.

[19] M.J. Wright, G.V. Candler, and M. Prampolini. Data-Parallel Lower-Upper Relaxation Method for the Navier-Stokes Equations. *AIAA Journal*, 34(7):1371–1377, July 1996.

[20] M.J. Wright, G.V. Candler, and D. Bose. A Data-Parallel Line-Relaxation Method for the Navier-Stokes Equations. Technical report, AIAA, 1997.

[21] R.W. MacCormack and G.V. Candler. The Solution of the Navier-Stokes Equations Using Gauss-Seidel Line Relaxation. *Computers and Fluids*, 17(1):135–150, 1989.

[22] P.K. Subbareddy and G.V. Candler. A fully discrete, kinetic energy consistent finite-volume scheme for compressible flows. *Journal of Computational Physics*, 228(5):1347–1364, 2009.

[23] J.L. Steger and R.F. Warming. Flux Vector Splitting of the Inviscid Gasdynamic Equations with Application to Finite-Difference Methods. *Journal of Computational Physics*, 40:263–293, 1981.

[24] F. Ducros, V. Ferrand, F. Nicoud, C. Weber, D. Darracq, C. Gacherieu, and T. Poinsot. Large-Eddy Simulation of the Shock/Turbulence Interaction. *Journal of Computational Physics*, 152(1):199–238, 1999.

[25] L.M. Mack. Boundary Layer Stability Theory. Report 900-277, Jet Propulsion Laboratory, June 1969.

[26] S.P. Schneider. Hypersonic laminar-turbulent transition on circular cones and scramjet forebodies. *Progress in Aerospace Sciences*, 40:1–50, January-February 2004.

[27] J.M. Kendall. Supersonic boundary layer stability experiments. Technical report, Proceedings from Boundary Layer Transition Study Group Meeting (ed. W. D. McCauley) Volume II, 1967.

[28] J.M. Kendall. Wind Tunnel Experiments Relating to Supersonic and Hypersonic Boundary-Layer Transition. *AIAA Journal*, 13(3):290–299, March 1975.

[29] A. Demetriades. Boundary-Layer Instability Observations at Mach Number 7. *Journal of Applied Mechanics*, 99(1):7–10, 1977.

[30] A. Demetriades. Laminar Boundary Layer Stability Measurements at Mach 7 Including Wall Temperature Effects. Technical Report AFOSR-TR-77-1311, Air Force Office of Scientific Research, November 1977.

[31] K.F. Stetson, E.R. Thompson, J.C. Donaldson, and L.G. Siler. Laminar Boundary Layer Stability Experiments on a Cone at Mach 8, Part 1: Sharp Cone. Paper 1983-1761, AIAA, July 1983.

[32] K.F. Stetson, E.R. Thompson, J.C. Donaldson, and L.G. Siler. Laminar Boundary Layer Stability Experiments on a Cone at Mach 8, Part 2: Blunt Cone. Paper 1984-0006, AIAA, January 1984.

[33] K.F. Stetson, E.R. Thompson, J.C. Donaldson, and L.G. Siler. Laminar Boundary Layer Stability Experiments on a Cone at Mach 8, Part 3: Sharp Cone at Angle of Attack. Paper 1985-0492, AIAA, January 1985.

[34] K.F. Stetson, E.R. Thompson, J.C. Donaldson, and L.G. Siler. Laminar Boundary Layer Stability Experiments on a Cone at Mach 8, Part 4: On Unit Reynolds Number and Environmental Effects. Paper 1986-1087, AIAA, May 1986.

[35] K.F. Stetson, E.R. Thompson, J.C. Donaldson, and L.G. Siler. Laminar Boundary Layer Stability Experiments on a Cone at Mach 8, Part 5: Tests with a Cooled Model. Paper 1989-1895, AIAA, June 1989.

[36] K.F. Stetson and R.L. Kimmel. On Hypersonic Boundary-Layer Stability. Paper 1992-0737, AIAA, January 1992.

[37] S.J. Rufer and S.P. Schneider. Hot-Wire Measurements of Instability Waves on Cones at Mach 6. Paper 2006-3054, AIAA, June 2006.

[38] K. Fujii. Experiment of the Two-Dimensional Roughness Effect on Hypersonic Boundary-Layer Transition. *Journal of Spacecraft and Rockets*, 43(4):731–738, July-August 2006.

[39] M. Estorf, R. Radespiel, S.P. Schneider, H.B. Johnson, and S. Hein. Surface-Pressure Measurements of Second-Mode Instability in Quiet Hypersonic Flow. Paper 2008-1153, AIAA, January 2008.

[40] H. Tanno, T. Komuro, K. Sato, K. Itoh, M. Takahashi, and K. Fujii. Measurement of hypersonic boundary layer transition on cone models in the free-piston shock tunnel HIEST. Paper 2009-0781, AIAA, January 2009.

[41] H. Knauss, T. Roediger, D.A. Bountin, B.V. Smorodsky, A.A. Maslov, and J. Srulijes. Novel Sensor for Fast Heat-Flux Measurements. *Journal of Spacecraft and Rockets*, 46(2):255–265, March-April 2009.

[42] T. Roediger, H. Knauss, M. Estorf, S.P. Schneider, and B.V. Smorodsky. Hypersonic Instability Waves Measured Using Fast-Response Heat-Flux Gauges. *Journal of Spacecraft and Rockets*, 46(2):266–273, March-April 2009.

[43] D.C. Berridge, K.M. Casper, S.J. Rufer, C.R. Alba, D.R. Lewis, S.J. Beresh, and S.P. Schneider. Measurements and Computations of Second-Mode Instability Waves in Three Hypersonic Wind Tunnels. Paper 2010-5002, AIAA, June 2010.

[44] L.M. Mack. Boundary Layer Linear Stability Theory. Report 709, AGARD, June 1984.

[45] M.R. Malik. Prediction and Control of Transition in Supersonic and Hypersonic Boundary Layers. *AIAA Journal*, 1989.

[46] M.R. Malik. Boundary Layer Transition Prediction Toolkit. Paper 1997-1904, AIAA, June 1997.

[47] H.L. Reed, W.S. Saric, and D. Arnal. Linear Stability Theory Applied to Boundary Layers. *Annu. Rev. Fluid. Mech*, 28:389–428, 1996.

[48] F.P. Bertolotti and T. Herbert. Analysis of the Linear Stability of Compressible Boundary Layers Using the PSE. *Theoret. Comput. Fluid Dynamics*, 3(1):117–124, 1991.

[49] C.L. Chang and M.R. Malik. Compressible Stability of Growing Boundary Layers Using Parabolized Stability Equations. Paper 1991-1636, AIAA, June 1991.

[50] H.B. Johnson, C.R. Alba, and G.V. Candler. Boundary-Layer Stability Analysis of the Hypersonic International Flight Research Transition Experiments. *Journal of Spacecraft and Rockets*, 45(2):228–236, March-April 2008.

[51] K. Itoh, S. Ueda, H. Tanno, T Komuro, and K. Sato. Hypersonic Aerothermodynamic and Scramjet Research Using High Enthalpy Shock Tunnel. *Shock Waves*, 12:93–98, 2002.

[52] H. Tanno, T. Komuro, K. Sato, K. Itoh, and M. Takahashi. Measurement of Hypersonic High-Enthalpy Boundary-Layer Transistion on a 7 degree cone model. Paper 2010-0310, AIAA, January 2010.

[53] H. Tanno, T. Komuro, K. Sato, K. Itoh, and M. Takahashi. Measurement of Surface Pressure Fluctuation in Hypersonic High-Enthalpy Boundary Layer on a 7 Degree Cone Model. Paper 2011-3889, AIAA, June 2011.

[54] D. Saunders, S. Yoon, and M. Wright. An Approach to Shock Envelope Grid Tailoring and Its Effect on Reentry Vehicle Solutions. Paper 2007-0207, AIAA, January 2007.

[55] F.G. Blottner, M. Johnson, and M. Ellis. Chemically Reacting Viscous Flow Program for Multi-Component Gas Mixtures. Technical Report SC-RR-70-754, 1971.

[56] H.B. Johnson and G.V. Candler. Analysis of Laminar-Turbulent Transition in Hypersonic Flight using PSE-Chem. Paper 2006-3057, AIAA, June 2006.

[57] H.B. Johnson, C.R. Alba, and G.V. Candler. Oblique Wave Disturbance Analysis of Supersonic Flow Past Axisymmetric and 2D Bodies at Angles of Attack. Paper 2008-4396, AIAA, June 2008.

[58] H.B. Johnson. *Thermochemical Interactions in Hypersonic Boundary Layer Stability*. PhD thesis, University of Minnesota, Minneapolis, Minnesota, 2000.

[59] N.A. Jaffe, T.T. Okamura, and A.M.O. Smith. Determination of Spatial Amplification Factors and Their Application to Predicting Transition. *AIAA Journal*, 8(2):301–308, February 1970.

[60] F.J. Chen, M.R. Malik, and I.E. Beckwith. Boundary-Layer Transition on a Cone and Flat Plate at Mach 3.5. *AIAA Journal*, 27(6):687–693, June 1989.

[61] M.R. Malik. Hypersonic Flight Transition Data Analysis Using Parabolized Stability Equations with Chemistry Effects. *Journal of Spacecraft and Rockets*, 40(3):332–344, May-June 2003.

[62] M.R. Malik, R.E. Spall, and C.L. Chang. Effect of Nose Bluntness on Boundary Layer Stability and Transition. Paper 1990-0112, AIAA, January 1990.

[63] J. Stilla. Engineering Transition Prediction for a Hypersonic Axisymmetric Boundary Layer. *Journal of Aircraft*, 31(6):1358–1364, November 1994.

[64] H.B. Johnson, T.G. Seipp, and G.V. Candler. Numerical Study of Hypersonic Reacting Boundary Layer Transition on Cones. *Physics of Fluids*, 10(10):2676–2685, October 1998.

[65] H. Johnson, C. Alba, G. Candler, M. MacLean, T. Wadhams, and M. Holden. Boundary Layer Stability Analysis to Support the HIFiRE Transition Experiment. Paper 2007-311, AIAA, January 2007.

[66] C.R. Alba, H.B. Johnson, M.D. Bartkowicz, G.V. Candler, and K.T. Berger. Boundary-Layer Stability Calculations for the HIFiRE-1 Transition Experiment. *Journal of Spacecraft and Rockets*, 45(6):1125–1133, November-December 2008.

[67] H.L. Reed. Role of Chemical Reactions in Hypersonic Flows. Technical Report RTO-EN-AVT-151-13, NATO, 2009.

[68] N. Gregory, J.T. Stuart, and W.S. Walker. On the Stability of Three-Dimensional Boundary Layers with Application to the Flow Due to a Rotating Disk. *Phil. Trans. R. Soc. Lond. A*, 248:155–199, 1955.

[69] R. Kobayashi, Y. Kohama, and M. Kurosawa. Boundary Layer Transition on a Rotating Cone in Axial Flow. *Journal of Fluid Mechanics*, 127:341–352, 1983.

[70] R. Kobayashi and H. Izumi. Boundary Layer Transition on a Rotating Cone in Still Fluid. *Journal of Fluid Mechanics*, 127:353–364, 1983.

[71] R.J. Lingwood. Absolute Instability of the Boundary Layer on a Rotating Disk. *Journal of Fluid Mechanics*, 299:17–33, 1995.

[72] W.E. Gray. The Effect of Wing Sweep on Laminar Flow. Paper 255, RAE TM Aero, 1952.

[73] W.E. Gray. The Nature of the Boundary Layer Flow at the Nose of a Swept Wing. Paper 256, RAE TM Aero, 1952.

[74] P.R. Owen and D.G. Randall. Boundary Layer Transition on a Sweptback Wing. Paper 277, RAE TM Aero, 1952.

[75] H.L. Reed and W.S. Saric. Stability of Three-Dimensional Boundary Layers. *Annu. Rev. Fluid. Mech*, 21:235–284, 1989.

[76] H. Bippes. Basic Experiments on Transition in Three-Dimensional Boundary Layers Dominated by Crossflow Instability. *Progress in Aerospace Sciences*, 35:363–412, 1999.

[77] W.S. Saric, H.L. Reed, and E.B. White. Stability and Transition of Three-Dimensional Boundary Layers. *Annu. Rev. Fluid. Mech*, 35:413–440, 2003.

[78] W.S. Saric and H.L. Reed. Crossflow Instabilities - Theory and Technology. Paper 2003-0771, AIAA, January 2003.

[79] J. Poggie and R.L. Kimmel. Traveling Instabilities in Elliptic Cone Boundary Layer Transition at Mach 8. Paper 1998-0435, AIAA, January 1998.

[80] R.L. Kimmel, J. Poggie, and S.N. Schwoerke. Laminar-Turbulent Transition in a Mach 8 Elliptic Cone Flow. *AIAA Journal*, 37(9):1080–1087, September 1999.

[81] M.D. Bartkowicz, P.K. Subbareddy, and G.V. Candler. Simulation of Boundary Layer Transition on Elliptic Cones in Hypersonic Flow. Paper 2010-1064, AIAA, January 2010.

[82] T.J. Juliano and S.P. Schneider. Instability and Transition on the HIFiRE-5 in a Mach-6 Quiet Tunnel. Paper 2010-5004, AIAA, June 2010.

[83] P.C. Stainback. Effect of Unit Reynolds Number, Nose Bluntness, Angle of Attack, and Roughness on Transition on a 5 deg Half-Angle Cone at Mach 8. Technical Note TN-D-4961, NASA, January 1969.

[84] V. DiCristina. Three-Dimensional Laminar Boundary-Layer Transition on a Sharp 8 degree Cone at Mach 10. *AIAA Journal*, 8(5):852–856, May 1970.

[85] K.F. Stetson. Hypersonic Boundary Layer Transition Experiments. Technical Report TR-80-3062, Air Force Wright Aeronautical Laboratories, October 1980.

[86] D.C. Berridge, A. Chou, C. Ward, L.E. Steen, P.L. Gilbert, T.J. Juliano, S.P. Schneider, and J.E. Gronvall. Hypersonic Boundary-Layer Transition Experiments in a Mach-6 Quiet Tunnel. Paper 2010-1061, AIAA, January 2010.

[87] A. Kroonenberg, R. Radespiel, G.V. Candler, and M. Estorf. Infrared Measurements of Boundary-Layer Transition on an Inclined Cone at Mach 6. Paper 2010-1063, AIAA, January 2010.

[88] F. Li, M. Choudhari, C.L. Chang, and J. White. Analysis of Instabilities in Non-Axisymmetric Hypersonic Boundary Layers Over Cones. Paper 2010-4643, AIAA, June 2010.

[89] P. Balakumar and L.R. Owens. Stability of Hypersonic Boundary Layers on a Cone at an Angle of Attack. Paper 2010-4718, AIAA, June 2010.

[90] C. Ward, B.M. Wheaton, A. Chou, P.L. Gilbert, L.E. Steen, and S.P. Schneider. Boundary-Layer Transition Measurements in a Mach-6 Quiet Tunnel. Paper 2010-4721, AIAA, June 2010.

[91] J.E. Gronvall, H.B. Johnson, and G.V. Candler. Hypersonic Three-Dimensional Boundary Layer Transition on a Cone at Angle of Attack. Paper 2011-3561, AIAA, June 2011.

[92] J.J. Kuehl, E. Perez, and H.L. Reed. JoKHeR: NPSE Simulations of Hypersonic Crossflow Instability. Paper 2012-0921, AIAA, January 2012.

[93] D.C. Berridge, C. Ward, R. Luersen, A. Chou, A.D. Abney, and S.P. Schneider. Boundary-Layer Instability Measurements in a Mach-6 Quiet Tunnel. Paper 2012-3147, AIAA, June 2012.

[94] H. Deyhle and H. Bippes. Disturbance Growth in an Unstable Three-Dimensional Boundary Layer and it Dependence on initial conditions. *Journal of Fluid Mechanics*, 316(9):73–113, 1996.

[95] H. Bippes. Transition Prediction in Three-Dimensional Boundary Layer Flows Unstable to Crossflow Instability. Paper 1997-1906, AIAA, June 1997.

[96] R.A. King. Three-dimensional boundary-layer transition on a cone at Mach 3.5. *Experiments in Fluids*, 13:305–314, 1992.

[97] K.F. Stetson. Mach 6 Experiments of Transition on a Cone at Angle of Attack. *Journal of Spacecraft and Rockets*, 19(5):397–403, 1982.

[98] R.H. Radeztsky, M.S. Reibert, and W.S. Saric. Effect of Isolated Micron-Sized Roughness on Transition in Swept-Wing Flows. *AIAA Journal*, 37(11):1370–1377, November 1999.

[99] L.E. Steen. Characterization and Development of Nozzles for a Hypersonice Quiet Wind Tunnel. Master's thesis, Purdue University, December 2010.

[100] C. Ward, B.M. Wheaton, A. Chou, D.C. Berridge, L.E. Letterman, R. Luersen, and S.P. Schneider. Hypersonic Boundary-Layer Transition Experiments in the Boeing/AFOSR Mach-6 Quiet Tunnel. Paper 2012-0282, AIAA, January 2012.

[101] E. Touber and N.D. Sandham. Large-Eddy Simulation of Low-Frequency Unsteadiness in a Turbulent Shock-Induced Separation Bubble. *Theor. Comput. Fluid Dyn.*, 23:79–107, 2009.

[102] E. Touber. *Unsteadiness in Shock-Wave/Boundary-Layer Interactions.* PhD thesis, University of Southampton, May 2010.

[103] Th. Herbert. Boundary-Layer Transition - Analysis and Prediction Revisited. Paper 1991-0737, AIAA, January 1991.

[104] M.R. Malik. Numerical Methods for Hypersonic Boundary Layer Stability. *Journal of Computational Physics*, 86:376–413, 1990.

[105] Th. Herbert. Parabolized Stability Equations. Report 793, AGARD, March-April 1993.

[106] C.L. Chang and M.R. Malik. Oblique-mode Breakdown and Secondary Instability in Supersonic Boundary Layers. *Journal of Fluid Mechanics*, 273:323–360, 1994.

Appendix A

Stability Analysis

A.1 Governing Equations

A.1.1 Disturbance Equations

The equations which govern the growth and evolution of disturbances are the compressible Navier-Stokes equations which have been previously discussed in chapter 2. However, in order to analyze boundary layer stability with less restrictive computational requirements than methods such as direct numerical simulations require, a different set of equations are used. These are the so-called disturbance equations which are themselves derived from the Navier-Stokes equations. A brief summary of the derivation of the disturbance equations and numerical approach is provided below. For a more detailed analysis see Johnson[58].

The process begins by decomposing the flow into two parts, a steady laminar base flow component and a disturbance fluctuation component, for example

$$\begin{aligned} u &= \overline{u} + u', \quad v = \overline{v} + v', \quad w = \overline{w} + w', \\ \rho &= \overline{\rho} + \rho', \quad T = \overline{T} + T', \quad T_v = \overline{T}_v + T'_v, \\ &\text{etc.} \end{aligned} \tag{A.1}$$

The above perturbations are substituted into the Navier-Stokes equations and the mean flow portion is subtracted and results in the following two-dimensional / axisymmetric form of the disturbance equations

$$\begin{aligned}\Gamma\frac{\partial\phi}{\partial t}+A\frac{\partial\phi}{\partial x}+B\frac{\partial\phi}{\partial y}+C\frac{\partial\phi}{\partial z}+D\phi \\ +V_{xx}\frac{\partial^2\phi}{\partial x^2}+V_{yy}\frac{\partial^2\phi}{\partial y^2}+V_{zz}\frac{\partial^2\phi}{\partial z^2} \\ +V_{xy}\frac{\partial^2\phi}{\partial xy}+V_{xz}\frac{\partial^2\phi}{\partial xz}+V_{yz}\frac{\partial^2\phi}{\partial yz}+F^n=0\end{aligned} \tag{A.2}$$

where ϕ is the vector of disturbance quantities defined as

$$\phi=\left(\rho_1',\rho_2',\ldots,\rho_{ns}',u',v',w',T',T_v'\right)^T$$

The coefficient matrices, Γ, A, B, C, D, V_{xx}, V_{yy}, V_{zz}, V_{xy}, V_{xz}, and V_{yz} are the Jacobians of the flux vectors and depend only on the mean flow variables and their derivatives. All the terms that vary nonlinearly with the elements of ϕ are grouped together in the vector F^n.

A.1.2 Parabolized Stability Equations

Before proceeding onto the derivation of the parabolized stability equations (PSE), it is computationally convenient to transform the Cartesian coordinate system into a body-fitted coordinate system. The following relations provide a means to transform into the computational coordinates

$$\begin{aligned}\xi_x&=\frac{y_\eta}{J} & \xi_y&=-\frac{x_\eta}{J}\\ \eta_x&=-\frac{y_\xi}{J} & \eta_y&=\frac{x_\xi}{J}\end{aligned}$$

where,

$$J=y_\eta x_\xi-x_\eta y_\xi$$

Though not shown here, the operators

$$\frac{\partial}{\partial x},\ \frac{\partial}{\partial y},\ \frac{\partial^2}{\partial x^2},\ \frac{\partial^2}{\partial y^2},\ \frac{\partial^2}{\partial x\partial y}$$

found in the stability equations are transformed into operators in the computational coordinates as well and can be found in Reference [58].

Following the method of Herbert[103], the linearized disturbance equations (A.2) are parabolized by assuming that the disturbance quantities are traveling waves of the following form

$$\phi = \chi(\xi, \eta)\, e^{i(kz - \omega t)} \tag{A.3}$$

where for the spatial stability problem, ω is the real frequency, k is the real spanwise wavenumber, and ξ and η are the body-tangential and body-normal computational coordinates. Taking the relevant derivatives of the assumed form for the disturbance quantities above yields the following

$$\begin{aligned} \frac{\partial \phi}{\partial t} &= -\, i\omega\phi \\ \frac{\partial \phi}{\partial z} &= \;\; ik\phi \\ \frac{\partial^2 \phi}{\partial z^2} &= -\, k^2\phi \end{aligned}$$

Substituting these derivatives into the linearized disturbance equations, applying the transformation to computational coordinates, collecting the terms containing ξ and η derivatives of ϕ gives

$$\widetilde{D}\phi + \widetilde{A}\frac{\partial \phi}{\partial \xi} + \widetilde{B}\frac{\partial \phi}{\partial \eta} + \widehat{V}_{\xi\xi}\frac{\partial^2 \phi}{\partial \xi^2} + \widehat{V}_{\eta\eta}\frac{\partial^2 \phi}{\partial \eta^2} + \widehat{V}_{\xi\eta}\frac{\partial^2 \phi}{\partial \xi \partial \eta} + F^n = 0 \tag{A.4}$$

Next, the mode shape $\chi(\xi, \eta)$ is decomposed into a fast-varying wave part and a slow-varying shape function

$$\chi(\xi, \eta) = \psi(\xi, \eta)\, A(\xi) \tag{A.5}$$

$$A(\xi) = e^{i\theta(\xi)} \tag{A.6}$$

where $d\theta/d\xi = \alpha(\xi)$ and α is the streamwise wavenumber. The function ψ is the shape function vector. Continuing the derivation requires computing the necessary derivatives of ϕ with respect to ξ and η, making appropriate substitutions, and applying some simplifying definitions, all of which produces the disturbance equations in computational coordinates

$$\widehat{D}\psi + \widehat{A}\frac{\partial \psi}{\partial \xi} + \widehat{B}\frac{\partial \psi}{\partial \eta} + \widehat{V}_{\xi\xi}\frac{\partial^2 \psi}{\partial \xi^2} + \widehat{V}_{\eta\eta}\frac{\partial^2 \psi}{\partial \eta^2} + \widehat{V}_{\xi\eta}\frac{\partial^2 \psi}{\partial \xi \partial \eta} + \widehat{F}^n = 0 \tag{A.7}$$

Finally, to obtain the linear PSE formulation a couple of additional simplifying assumptions are made. First, the terms $\widehat{V}_{\xi\xi}\frac{\partial^2\psi}{\partial\xi^2}$ and $\widehat{V}_{\xi\eta}\frac{\partial^2\psi}{\partial\xi\partial\eta}$ are assumed to be much smaller than all other terms and are thusly neglected. This assumption is considered reasonable due to the selection of wavenumber α in the marching procedure such that the derivative $\frac{\partial\psi}{\partial\xi}$ is small, making the streamwise second derivatives negligible. Second, since it has already been assumed that all the disturbances are very small, it can also be assumed that their products are even smaller, enough so to be neglected. Therefore, the nonlinear terms $\widehat{F}^n$ are dropped. This gives the linearized version of the parabolized stability equations

$$\widehat{D}\psi + \widehat{A}\frac{\partial\psi}{\partial\xi} + \widehat{B}\frac{\partial\psi}{\partial\eta} + \widehat{V}_{\eta\eta}\frac{\partial^2\psi}{\partial\eta^2} = 0 \tag{A.8}$$

A couple of comments can be made about the above approach (A.8). First, it describes the evolution of the shape function ψ and is considered "nearly" parabolic in that all the second derivatives in the streamwise direction are absent while the ellipticity associated with the wave part is retained and absorbed in the matrices $\widehat{D}$, $\widehat{A}$, and $\widehat{B}$. Second, due to its parabolic nature, this formulation constitutes an initial boundary value problem for the shape function and wavenumber α and as such can be solved using an efficient marching procedure. In order to proceed, however the wavenumber and eigenfunction must first be estimated and is typically obtained using linear stability approximations.

For the linear stability formulation, a so-called quasi-parallel flow assumption is made. The consequences of this assumption result in the shape function being a function of η only ($\psi = \psi(\eta)$) and $d\alpha/d\xi = 0$. Therefore, rewriting equations A.3 and A.5 gives

$$\phi = \chi(\eta)\, e^{i(kz-\omega t)}$$

$$\chi = \psi(\eta)\, e^{i\alpha}$$

Applying these changes to equation A.8 yields the linear stability equations, also referred to as linear stability theory (LST)

$$\widehat{D}\psi + \widehat{B}\frac{\partial\psi}{\partial\eta} + \widehat{V}_{\eta\eta}\frac{\partial^2\psi}{\partial\eta^2} = 0 \tag{A.9}$$

With this, all of the necessary governing equations have been formulated and as such a numerical procedure may be used to solve these systems computationally and will be summarized in the next section.

A.2 Numerical Approach

As previously mentioned, a method for estimating the wavenumber α and shape function are required before a PSE analysis can proceed. As such, applying techniques developed for linear stability theory and specifically following the methodology described by Malik[104], the required estimates are generated using a two-step process. The first step, referred to as the global method generates a spectrum of approximate eigenvalue guesses. The second step, referred to as the local method, then refines the estimates taken from the global method.

A.2.1 Global LST Procedure

To start this procedure it is assumed that the nonlinear term α^2 can be dropped in the global eigenvalue search. Then, after grouping together all terms which are linear in the wavenumber α, the generalized eigenvalue problem set up for spatial stability can be stated as

$$\underline{A}\Psi = \alpha \underline{B}\Psi \tag{A.10}$$

where,

$$\underline{A} = \widetilde{D} + \widetilde{B}\frac{\partial}{\partial \eta} + \widehat{V}_{\eta\eta}\frac{\partial^2}{\partial \eta^2}$$

$$\underline{B} = -i\widetilde{A} - i\widehat{V}_{\xi\eta}\frac{\partial}{\partial \eta}$$

The discretization of the above η derivatives is accomplished using second-order central differences approximations. Rearranging and combining the terms in the discretized system result in the following formulations

$$\underline{A}_j\psi_j = \underline{A}_j^1\psi_{j+1} + \underline{A}_j^2\psi_j + \underline{A}_j^3\psi_{j-1}$$

$$\underline{B}_j\psi_j = \underline{B}_j^1\psi_{j+1} + \underline{B}_j^2\psi_j + \underline{B}_j^3\psi_{j-1}$$

Again, the reader is referred to Johnson[58] for details about the coefficients $\underline{A}_j^1$, $\underline{B}_j^1$, $\underline{A}_j^2$, $\underline{B}_j^2$, etc.

The boundary conditions that are applied to this system consist of setting the velocity disturbances, temperature disturbances, and the gradient of the pressure disturbances to zero at the wall. At the outer boundary, all disturbances quantities are set to zero. With this, the resulting system of equations can be stated as

$$
\begin{bmatrix}
\underline{A}_n^2 & \underline{A}_n^3 & 0 & & & \cdots & & & 0 \\
\underline{A}_{n-1}^1 & \underline{A}_{n-1}^2 & \underline{A}_{n-1}^3 & 0 & & & & & \\
0 & \underline{A}_{n-2}^1 & \underline{A}_{n-2}^2 & \underline{A}_{n-2}^3 & 0 & & & & \\
 & & \ddots & \ddots & \ddots & & & & \vdots \\
 & & & \ddots & \ddots & \ddots & & & \\
\vdots & & & & \ddots & \ddots & \ddots & & \\
 & & & & 0 & \underline{A}_3^1 & \underline{A}_3^2 & \underline{A}_3^3 & 0 \\
 & & & & & 0 & \underline{A}_2^1 & \underline{A}_2^2 & \underline{A}_2^3 \\
0 & & & \cdots & & & 0 & \underline{A}_1^1 & \underline{A}_1^2
\end{bmatrix}
\begin{bmatrix}
\vec{\Psi}_n \\ \vec{\Psi}_{n-1} \\ \vec{\Psi}_{n-2} \\ \\ \\ \\ \vec{\Psi}_3 \\ \vec{\Psi}_2 \\ \vec{\Psi}_1
\end{bmatrix}
$$

$$
= \alpha
\begin{bmatrix}
\underline{B}_n^2 & \underline{B}_n^3 & 0 & & & \cdots & & & 0 \\
\underline{B}_{n-1}^1 & \underline{B}_{n-1}^2 & \underline{B}_{n-1}^3 & 0 & & & & & \\
0 & \underline{B}_{n-2}^1 & \underline{B}_{n-2}^2 & \underline{B}_{n-2}^3 & 0 & & & & \\
 & & \ddots & \ddots & \ddots & & & & \vdots \\
 & & & \ddots & \ddots & \ddots & & & \\
\vdots & & & & \ddots & \ddots & \ddots & & \\
 & & & & 0 & \underline{B}_3^1 & \underline{B}_3^2 & \underline{B}_3^3 & 0 \\
 & & & & & 0 & \underline{B}_2^1 & \underline{B}_2^2 & \underline{B}_2^3 \\
0 & & & \cdots & & & 0 & 0 & 0
\end{bmatrix}
\begin{bmatrix}
\vec{\Psi}_n \\ \vec{\Psi}_{n-1} \\ \vec{\Psi}_{n-2} \\ \\ \\ \\ \vec{\Psi}_3 \\ \vec{\Psi}_2 \\ \vec{\Psi}_1
\end{bmatrix}
$$

and is the generalized eigenvalue problem to be solved, which is done using the LZ algorithm.

A.2.2 Local LST Procedure

The local method provides refinement to the wavenumber guesses generated by the global method. Here again, the linearized stability equations are solved

$$\widehat{D}\psi + \widehat{B}\frac{\partial \psi}{\partial \eta} + \widehat{V}_{\eta\eta}\frac{\partial^2 \psi}{\partial \eta^2} = 0 \tag{A.11}$$

where now the nonlinear wavenumber terms α^2 are now included in contrast with the global method. The discretization of the η derivatives are now approximated with fourth-order central differences for the interior points and after rearranging terms gives the following form

$$\underline{A}_j^1\psi_{j+2} + \underline{A}_j^2\psi_{j+1} + \underline{A}_j^3\psi_j + \underline{A}_j^4\psi_{j-1} + \underline{A}_j^5\psi_{j-2} = 0 \tag{A.12}$$

For near boundary points, second-order central difference approximations are used giving

$$\underline{C}_j^1\psi_{j+1} + \underline{C}_j^2\psi_j + \underline{C}_j^3\psi_{j-1} = 0 \tag{A.13}$$

In order to prevent arriving at a trivial solution to equation A.11, which is homogeneous, a non-homogeneous boundary condition must be imposed at the wall. Therefore the equation for $\widehat{u} = 0$ at the wall used in the global procedure is instead replaced with the following normalization condition for the density fluctuation

$$\widehat{\rho} = \rho_{norm} \quad \text{where} \quad \rho_{norm} = \rho_\infty$$

Boundary conditions for the outer boundary are identical to those used in the global method. The resulting system is a block pentadiagonal matrix system

$$\underbrace{\begin{bmatrix}
\underline{A}_n^3 & \underline{A}_n^4 & 0 & 0 & & & \cdots & & 0 \\
\underline{C}_{n-1}^1 & \underline{C}_{n-1}^2 & \underline{C}_{n-1}^3 & 0 & 0 & & & & \\
\underline{A}_{n-2}^1 & \underline{A}_{n-2}^2 & \underline{A}_{n-2}^3 & \underline{A}_{n-2}^4 & \underline{A}_{n-2}^5 & 0 & & & \\
0 & \underline{A}_{n-2}^1 & \underline{A}_{n-2}^2 & \underline{A}_{n-2}^3 & \underline{A}_{n-2}^4 & \underline{A}_{n-2}^5 & & & \vdots \\
 & & \ddots & \ddots & \ddots & \ddots & \ddots & & \\
\vdots & & & \underline{A}_4^1 & \underline{A}_4^2 & \underline{A}_4^3 & \underline{A}_4^4 & \underline{A}_4^5 & 0 \\
 & & & 0 & \underline{A}_3^1 & \underline{A}_3^2 & \underline{A}_3^3 & \underline{A}_3^4 & \underline{A}_3^5 \\
 & & & & 0 & 0 & \underline{C}_2^1 & \underline{C}_2^2 & \underline{C}_2^3 \\
0 & & \cdots & & & 0 & 0 & \underline{A}_1^1 & \underline{A}_1^2
\end{bmatrix}}_{\underline{A}}
\underbrace{\begin{bmatrix} \vec{\Psi}_n \\ \vec{\Psi}_{n-1} \\ \vec{\Psi}_{n-2} \\ \vec{\Psi}_{n-3} \\ \\ \vdots \\ \\ \vec{\Psi}_4 \\ \vec{\Psi}_3 \\ \vec{\Psi}_2 \\ \vec{\Psi}_1 \end{bmatrix}}_{\Psi}
= \underbrace{\begin{bmatrix} 0 \\ 0 \\ 0 \\ 0 \\ \\ \vdots \\ \\ 0 \\ 0 \\ 0 \\ B_1 \end{bmatrix}}_{B}$$

or,

$$\underline{A}\Psi = B \tag{A.14}$$

This system contains terms in both α and α^2. Provided the initial estimation of α from the global procedure, the system shown in equation A.14 can be solved by iterating over α using the secant method until $\widehat{V}_{x,j=1} = 0$. This process gives both the complex wavenumber α and the disturbance eigenfunction ψ at this surface location and provides the starting estimates for the PSE marching procedure.

A.2.3 PSE Solution Procedure

Now that estimates for the disturbance eigenfunction and complex wavenumber have been found and refined, it is now possible to set up a numerical framework to solve the linear parabolized stability equations given by

$$\widehat{D}\psi + \widehat{A}\frac{\partial\psi}{\partial\xi} + \widehat{B}\frac{\partial\psi}{\partial\eta} + \widehat{V}_{\eta\eta}\frac{\partial^2\psi}{\partial\eta^2} = 0 \tag{A.15}$$

In order to develop a marching procedure, careful attention must be paid to the methodology as this problem is ill-posed due to the presence of α and $d\alpha/d\xi$ in the Jacobian matrices in addition to ψ and $d\psi/d\xi$. As such, the marching procedure must be capable of simultaneously updating both ψ and α at each step, therefore the method summarized here follows a similar approach proposed by Herbert[105].

In order to provide closure for this ill-posed system, a normalization technique is used. To illustrate, it is convenient to consider the assumed disturbance form

$$\phi = \psi\left(\xi, \eta\right) e^{i\theta(\xi)} e^{i(kz-\omega t)} \tag{A.16}$$

rewriting this in a logarithmic form gives

$$\ln \phi = \ln \psi\left(\xi, \eta\right) + i\theta\left(\xi\right) + i\left(kz - \omega t\right) \tag{A.17}$$

In order to obtain an expression for the complex wavenumber α, the partial derivative of equation A.17 with respect to ξ is taken while recalling the definition $\partial\theta/\partial\xi = \alpha$ gives the following result

$$-i\frac{\partial \ln \phi}{\partial \xi} = \alpha - i\frac{\left(\frac{\partial \psi}{\partial \xi}\right)}{\psi} \tag{A.18}$$

It can be observed that since ψ is a function of both ξ and η that α also has an η dependence, unless $\partial\psi/\partial\xi = 0$. It has been proposed, in order to remove the wavenumber's dependence on η, to use a particular normalization. This can be described as first multiplying both sides by the weight $|\psi|^2$, integrating over the domain Ω, dividing by the integral of $|\psi|^2$, and taking advantage of the property that $|\psi|^2 = \psi^\dagger\psi$

$$-i\frac{\int_\Omega |\psi|^2 \frac{\partial \ln \phi}{\partial \xi} dn}{\int_\Omega |\psi|^2 dn} = \alpha - i\frac{\int_\Omega \psi^\dagger \left(\frac{\partial \psi}{\partial \xi}\right) dn}{\int_\Omega |\psi|^2 dn} \tag{A.19}$$

where Ω represents the domain that extends in the body-normal direction from the surface to the outer boundary. Now, to remove the η dependence, at each marching step α and ψ are selected such that the relationship in equation A.19 is maintained while the following is also achieved

$$\int_{\Omega} \psi^{\dagger} \left(\frac{\partial \psi}{\partial \xi} \right) dn = 0$$

Applying this to an iterative approach yields

$$\alpha_{new} = \alpha_{old} - i \left(\frac{\int_{\Omega} \psi^{\dagger} \left(\frac{\partial \psi}{\partial \xi} \right) dn}{\int_{\Omega} |\psi|^2 \, dn} \right) \tag{A.20}$$

Chang and Malik[106] specifically proposed using a normalization based on the disturbance kinetic energy given by the following

$$\alpha_{new} = \alpha_{old} - i \left(\frac{I}{E} \right) \tag{A.21}$$

where,

$$I = \int_{\Omega} \overline{\rho} \left(\widehat{u}^{\dagger} \frac{\partial \widehat{u}}{\partial \xi} + \widehat{v}^{\dagger} \frac{\partial \widehat{v}}{\partial \xi} + \widehat{w}^{\dagger} \frac{\partial \widehat{w}}{\partial \xi} \right) dn$$

and

$$E = \int_{\Omega} \overline{\rho} \left(|\widehat{u}|^2 + |\widehat{v}|^2 + |\widehat{w}|^2 \right) dn$$

Taking equations A.15 and A.19 along with appropriate boundary conditions provides the well-posed system to be solved numerically. Constructing this system in a way that provides for straightforward implementation computationally will only be summarized here.

First, the derivatives with respect to ξ from equation A.15 are discretized, terms are rearranged using some useful simplifying definitions which gives

$$\widehat{D}_i^m \psi_i^m + \widehat{B}_i^m \frac{\partial \psi_i^m}{\partial \eta} + \widehat{V}_{\eta\eta,i}^m \frac{\partial^2 \psi_i^m}{\partial \eta^2} + \widehat{A}_i^m \psi_i^m = \widehat{A}_i^m \psi_{i-1}^m$$

where i represents the streamwise index location and m represents the iteration index for converging α. Next, the derivatives with respect to η are discretized using fourth-order central differencing for the interior points giving

$$\underline{A}_{i,j}^{1,m} \psi_{i,j+2}^m + \underline{A}_{i,j}^{2,m} \psi_{i,j+1}^m + \underline{A}_{i,j}^{3,m} \psi_{i,j}^m + \underline{A}_{i,j}^{4,m} \psi_{i,j-1}^m + \underline{A}_{i,j}^{5,m} \psi_{i,j-2}^m = \widehat{A}_{i,j}^m \psi_{i-1,j}^m \tag{A.22}$$

For the points near boundaries, second-order central differences are used giving

$$\underline{C}_{i,j}^{1,m}\psi_{i,j+1}^{m} + \underline{C}_{i,j}^{2,m}\psi_{i,j}^{m} + \underline{C}_{i,j}^{3,m}\psi_{i,j-1}^{m} = \widehat{A}_{i,j}^{m}\psi_{i-1,j}^{m} \tag{A.23}$$

Identical boundary conditions at the wall are used for the PSE formulation as was used in the LST formulation, excluding the normalization of ρ. For the outer boundary, the same boundary conditions are used as was used in both the global and local linear stability methods. The resulting system is a block pentadiagonal matrix problem, as was the case with the local LST method and is given by

$$\underbrace{\begin{bmatrix}
\underline{A}_{i,n}^{3,m} & \underline{A}_{i,n}^{4,m} & 0 & 0 & & & \cdots & & 0 \\
\underline{C}_{i,n-1}^{1,m} & \underline{C}_{i,n-1}^{2,m} & \underline{C}_{i,n-1}^{3,m} & 0 & 0 & & & & \\
\underline{A}_{i,n-2}^{1,m} & \underline{A}_{i,n-2}^{2,m} & \underline{A}_{i,n-2}^{3,m} & \underline{A}_{i,n-2}^{4,m} & \underline{A}_{i,n-2}^{5,m} & 0 & & & \\
0 & \underline{A}_{i,n-2}^{1,m} & \underline{A}_{i,n-2}^{2,m} & \underline{A}_{i,n-2}^{3,m} & \underline{A}_{i,n-2}^{4,m} & \underline{A}_{i,n-2}^{5,m} & & & \vdots \\
 & & \ddots & \ddots & \ddots & \ddots & \ddots & & \\
\vdots & & & \underline{A}_{i,4}^{1,m} & \underline{A}_{i,4}^{2,m} & \underline{A}_{i,4}^{3,m} & \underline{A}_{i,4}^{4,m} & \underline{A}_{i,4}^{5,m} & 0 \\
 & & & 0 & \underline{A}_{i,3}^{1,m} & \underline{A}_{i,3}^{2,m} & \underline{A}_{i,3}^{3,m} & \underline{A}_{i,3}^{4,m} & \underline{A}_{i,3}^{5,m} \\
 & & & & 0 & 0 & \underline{C}_{i,2}^{1,m} & \underline{C}_{i,2}^{2,m} & \underline{C}_{i,2}^{3,m} \\
0 & & \cdots & & & 0 & 0 & \underline{A}_{i,1}^{1,m} & \underline{A}_{i,1}^{2,m}
\end{bmatrix}}_{\underline{A}^{m}}$$

$$\underbrace{\begin{bmatrix} \psi^m_{i,n} \\ \psi^m_{i,n-1} \\ \psi^m_{i,n-2} \\ \psi^m_{i,n-3} \\ \\ \vdots \\ \\ \\ \psi^m_{i,4} \\ \psi^m_{i,3} \\ \psi^m_{i,2} \\ \psi^m_{i,1} \end{bmatrix}}_{\psi^m} \qquad \underbrace{\begin{bmatrix} \widehat{A}^m_{i,n}\psi^m_{i-1,n} \\ \widehat{A}^m_{i,n-1}\psi^m_{i-1,n-1} \\ \widehat{A}^m_{i,n-2}\psi^m_{i-1,n-2} \\ \widehat{A}^m_{i,n-3}\psi^m_{i-1,n-3} \\ \\ \vdots \\ \\ \\ \widehat{A}^m_{i,4}\psi^m_{i-1,4} \\ \widehat{A}^m_{i,3}\psi^m_{i-1,3} \\ \widehat{A}^m_{i,2}\psi^m_{i-1,2} \\ 0 \end{bmatrix}}_{B^m}$$

where

$$\underline{A}^m \psi^m_i = B^m \tag{A.24}$$

In summary, the numerical procedure involved in marching the solution in the PSE method is as follows

1. Start at iteration $m = 0$, let $\alpha_i = \alpha_{i-1}$ (or if at the starting location $\alpha_i = \alpha_{LST}$)

2. Update ψ^m_i by solving the system expressed in equation A.24

$$\underline{A}^m \psi^m_i = B^m$$

3. With the new ψ^m_i, update α^m using equation A.21

$$\alpha_{new} = \alpha_{old} - i\left(\frac{I}{E}\right)$$

4. Repeat steps 2 and 3 until the following criterion is met

$$\frac{\left|\alpha_i^{m+1}\right| - \left|\alpha_i^m\right|}{\left|\alpha_i^{m+1}\right|} < \epsilon$$

For a more in-depth development of this method see Reference [58].

A.2.4 Transition Prediction

With the ability to solve the parabolized stability equations, disturbances may now be tracked as they either grow or decay within the boundary layer. It is for this reason, along with the lower computational costs compared with direct numerical simulations, that this method has gained wide use in analyzing boundary layers.

In addition, this method can be coupled with a transition criterion, the so-called e^N method, by which the transition location can be predicted. It should, however, be noted that there are limitations to this criterion. For example, this method does not take into account the receptivity process by which disturbances of varying amplitudes are introduced into the boundary layer. It is therefore considered a semi-empirical method. In the e^N method the amplitude growth of a constant frequency is tracked and integrated as follows

$$e^N = \exp \int_{s_0}^{s} \frac{1}{A}\frac{dA}{dx} ds$$

which can also be expressed

$$N(\omega, s) = \ln\left(\frac{A}{A_o}\right) = \int_{s_0}^{s} \sigma ds$$

where s_0 is the first neutral point at the given frequency, $\frac{1}{A}\frac{dA}{ds}$ is the spatial growth rate, σ, and where

$$\sigma = -\alpha_i + \frac{1}{2E}\frac{dE}{ds}$$

$$E = \int_n \overline{\rho}\left(|\widehat{u}|^2 + |\widehat{v}|^2 + |\widehat{w}|^2\right) dn$$

This integration is carried out until the end of the body has been reached unless the disturbance frequency ω becomes stable before then.

Appendix B

Digital Filter Method

B.1 Surface Roughness Model

The approach used to generate the surface roughness was adapted from a digital filtering method used for prescribing perturbations as an inflow condition in shock-boundary layer interaction studies[101]. The primary benefit of this approach is the ability to specify a desired length scale for the roughness. This allows one to target and effectively perturb the most unstable cross-flow wavenumbers while providing a roughness pattern that reasonably reflects observed surface imperfections in real experimental models.

Starting from a one-dimensional description, a set of p random roughness heights (B.1a) with zero mean (B.1b) and unit variance (B.1c) is defined as follows

$$\{y_k\}_{1\leq k\leq p} \tag{B.1a}$$

$$\overline{y}_k \equiv \sum_{k=1}^{p} \frac{y_k}{p} = 0 \tag{B.1b}$$

$$y_k y_k \equiv \sum_{k=1}^{p} \frac{y_k^2}{p} = 1 \tag{B.1c}$$

Using a set of real-numbered filter coefficients, the filter values can be generated by defining the discrete filter operator (B.2b)

$$\{b_j\}_{-N\leq j\leq N} \tag{B.2a}$$

$$\hat{y}_k \equiv F_D\left(y_k\right) = \sum_{j=-N}^{N} b_j y_{k+j} \tag{B.2b}$$

Since the filter operator defined above is linear, making the averaging and filtering operations commutative, and since the set of random heights (B.1a) is composed of zero mean (B.1b) and unit variance (B.1c) it can be shown that

$$\overline{\hat{y}_k} = 0 \tag{B.3a}$$

$$\overline{\hat{y}_k \hat{y}_k} = \sum_{j=-N+q}^{N} b_j b_{j-q} \tag{B.3b}$$

The desired model for a two-point correlation function, in one dimension, is chosen to be

$$R\left(x_k + x\right) = \exp\left(-\frac{\pi x}{2I_x}\right) \tag{B.4}$$

where x_k is some reference point, x is the distance from the reference point, and I_x is the specified length scale. In the discrete domain, if we define the following

$$I_x = n\triangle x \;\text{ and }\; x = q\triangle x \tag{B.5}$$

then equation B.4 becomes

$$R\left(x_k + q\triangle x\right) \equiv \frac{\overline{\hat{y}_k \hat{y}_{k+q}}}{\overline{\hat{y}_k \hat{y}_k}} = \exp\left(-\frac{\pi q}{2n}\right) \tag{B.6}$$

Substituting equation B.3b into equation B.6 yields the following equation which can be used to solve for the filter coefficients

$$\frac{\sum_{j=-N+1}^{N} b_j b_{j-1}}{\sum_{j=-N}^{N} b_j^2} = \exp\left(-\frac{\pi q}{2n}\right) \tag{B.7}$$

The solution to this system may be approximated by

$$b_k \approx \frac{\widetilde{b}_k}{\left(\sum_{j=-N}^{N} \widetilde{b}_j^2\right)^{1/2}} \;\text{ where }\; \widetilde{b}_k = \exp\left(-\frac{\pi k}{n}\right) \tag{B.8}$$

For more details on the approach outlined here, see Touber and Sandham[101].

The process of generating surface roughness was accomplished by first selecting a desired length scale, I_r, to use in the two dimensional extension of the method described above. A maximum radius, defining the filtering neighborhood, was selected to be $r_{max} = 3I_r$. Next, the set of random roughness heights with a normal distribution about zero and unit variance was created on the surface. One straightforward method of creating these random numbers is to use a generic pseudo-random number generator to generate uniformly distributed random numbers and modify the range to fit in $(0, 1]$. Then taking two independent numbers, u and v, from that set one can utilize a form of the Box-Muller transform to obtain two independent numbers, z_1 and z_2, with a normal distribution and unit standard deviation as follows

$$z_1 = u\sqrt{\frac{-2\ln s}{s}} \quad where \quad s = u^2 + v^2 \quad and \quad 0 < s < 1 \tag{B.9a}$$

$$z_2 = v\sqrt{\frac{-2\ln s}{s}} \quad where \quad s = u^2 + v^2 \quad and \quad 0 < s < 1 \tag{B.9b}$$

Finally, using the predefined filtering neighborhood and specified length scale, the surface roughness heights were filtered.